

**Life extension and defect tolerance analysis of
HFMI treated welds in bridge application**

Yuki Banno

Doctoral Thesis

Gifu, Japan 2022

04/04/2022

Gifu University
Graduate School of Engineering
Mechanical and Civil Engineering Division

Supervised by Koji Kinoshita
(Gifu University, Gifu, Japan)
Co-supervised by Zuheir Barsoum
(KTH Royal Institute of Technology, Stockholm, Sweden)

Contents

List of figures	5
List of tables	7
Abbreviations	8
Acknowledgements	9
Abstract.....	10
 Chapter 1 Introduction	 12
1.1 Background.....	13
1.2 Objective.....	15
1.3 Disposition of this thesis	16
 Chapter 2 Review of literature including authors' previous study	 19
2.1 Introduction	20
2.2 Peening techniques	20
2.2.1 Hammer and needle peening	21
2.2.2 High frequency mechanical impact	25
2.3 HFMI simulation	31
2.3.1 Simulation approaches.....	31
2.3.2 Contact problem	34
2.3.3 Material hardening behavior.....	34
2.3.4 Optimum parameters and settings for HFMI simulation.....	38
2.3.4.1 Mesh size	38
2.3.4.2 Feed rate and the number of hits	39
2.3.4.3 Material hardening model.....	40
2.4 Effect of HFMI treatment on life extension of pre-fatigued welded joints	41
2.4.1 Hammer and needle peening	41
2.4.2 High frequency mechanical impact	43
2.5 Linear elastic fracture mechanics	44
2.5.1 Stress intensity factor.....	45
2.5.2 The principle of superposition	46
2.5.3 Stage of crack propagation	47
2.5.4 Fatigue life estimation of pre-fatigued welds treated by HFMI using LEFM..	48
2.6 Conclusions	49

Chapter 3 Validity of HFMI simulation for residual stress estimation using a flat and bead on steel plates models.....	51
3.1 Introduction	52
3.2 HFMI simulation to flat steel plate model.....	52
3.2.1 FE modeling of flat steel plate and HFMI tool.....	52
3.2.2 Material hardening model.....	55
3.2.3 Investigation on reduction of simulation time.....	56
3.2.4 Investigation of influence of under- and- over treatment on residual stress state	59
3.2.4.1 Influence of under-treatment on residual stress state	60
3.2.4.2 Influence of over-treatment on residual stress state	63
3.2.5 Influence of surface removal after HFMI simulation on residual stress state ..	65
3.3 HFMI simulation to bead on steel plate model.....	67
3.3.1 Peening treatment on bead on steel plate specimen	67
3.3.2 FE modeling of bead on steel plate specimen and peening tool.....	68
3.3.3 Comparison of experimental and simulation results	69
3.4 Conclusions	72
 Chapter 4 Defect tolerance analysis considering crack opening-closing behavior in HFMI treated welds.....	 73
4.1 Introduction	74
4.2 Review of experimental study on pre-fatigued rat-hole specimen treated by HFMI	74
4.3 Numerical investigation of defect tolerance considering crack opening-closing behavior on pre-fatigued welded joints treated by HFMI	75
4.3.1 Modeling of the specimen and fatigue crack.....	75
4.3.2 Material hardening model.....	78
4.3.3 Elastic thermal analysis for initial welding residual stress.....	79
4.3.4 Applied cyclic loading	82
4.4 Numerical investigation results	82
4.4.1 Induced compressive residual stress.....	82
4.4.2 Observation of change of slit geometry after HFMI simulation	87
4.4.3 Observation of opening-closing behavior of HFMI treated slit	90
4.5 Experimental investigation of crack opening-closing behavior on pre-fatigued welded joint treated by hammer peening.....	95
4.5.1 Experimental procedure.....	95
4.5.2 Non-destructive ultrasonic testing	95

4.5.3 Experimental investigation result.....	97
4.6 Conclusions	100
Chapter 5 Life extension analysis considering crack opening-closing behavior in HFMI treated welds.....	102
5.1 Introduction	103
5.2 Simulation model.....	103
5.2.1 The rat-hole model.....	103
5.2.2 Modeling of fatigue crack.....	105
5.2.3 Compressive residual stress.....	106
5.3 Linear elastic fracture mechanics	108
5.3.1 M-integral for stress intensity factor determination	108
5.3.2 Incorporation of compressive residual stresses	111
5.4 Investigation of influence of crack front template on SIF	111
5.5 Investigation of crack opening stress at crack tip.....	113
5.6 Crack propagation analysis using LEFM	118
5.6.1 Crack propagation analysis based on quasi-static growth model	118
5.6.2 Results of crack propagation analysis in HFMI treated welds	119
5.6.3 Fatigue life calculation	121
5.6.4 Results of fatigue life calculation	121
5.7 Conclusions	122
Chapter 6 Conclusions	124
6.1 Conclusions	124
6.2 Recommendation based on the current studies	126
References.....	128

List of figures

Fig. 1-1	Age profiles of welded steel bridges.....	13
Fig. 1-2	Disposition of this thesis.....	18
Fig. 2-1	Overview of different improvement techniques on the market [13].....	21
Fig. 2-2	Hammer peening.....	22
Fig. 2-3	Needle peening.....	23
Fig. 2-4	Fatigue test results using PPP treated out-of-plane gusset welded joints in the author's previous study	24
Fig. 2-5	Schematic diagram of HFMI using ultrasonic technologies.....	26
Fig. 2-6	Examples of four different HFMI devices [28]	26
Fig. 2-7	Examples of tip geometries and multiple indenter [29].....	26
Fig. 2-8	Schematic image of main benefits of HFMI [30]	27
Fig. 2-9	Fatigue design curves proposed by IIW recommendations	28
Fig. 2-10	“Staircase” improvement for HFMI treated weld [13]	28
Fig. 2-11	Orientation of HFMI tool with respect to the weld [13]	29
Fig. 2-12	Examples of visual inspection of HFMI treated welds [13]	30
Fig. 2-13	Definitions of indentation depth and width [13].....	30
Fig. 2-14	Two types of HFMI simulation approaches [50]	33
Fig. 2-15	Impact velocity recorded using a high-speed camera in [50]	33
Fig. 2-16	Impact force during HFMI treatment measured in [50]	33
Fig. 2-17	Yield surface of different hardening models under loading	36
Fig. 2-18	Complex material behavior expressed by the Chaboche model [69]	37
Fig. 2-19	Stress/strain response observed in the test result using small specimen and in the simulation using the single element [50].....	38
Fig. 2-20	Stress/strain response in HAZ, filler material, and base material [59]	38
Fig. 2-21	Residual stress distributions in depth on different mesh sizes [43]	39
Fig. 2-22	The effect of PPP treatment on pre-fatigued welded joints in the author's previous study.....	42
Fig. 2-23	Three different crack opening modes found in [84]	45
Fig. 2-24	Stresses near the tip of a crack in an elastic material [85]	46
Fig. 2-25	The principle of superposition	47
Fig. 2-26	Schematic of the three main stages of crack propagation found in [88].....	48
Fig. 3-1	The flat steel plate model used in FE HFMI simulation	54
Fig. 3-2	Isotropic hardening properties used in [40]	56
Fig. 3-3	Residual stress state obtained from the HFMI simulations using different	

	material densities	59
Fig. 3-4	History of energy balance during the HFMI simulation using the material density of 1.0 kg/mm ³	59
Fig. 3-5	Simulated transverse residual stress induced by the different feed rates	62
Fig. 3-6	Counter figures of transverse residual stress by the different feed rates	62
Fig. 3-7	Simulated transverse residual stress induced by the different number of hits	64
Fig. 3-8	Time history of HFMI simulation on the flat steel plate model	64
Fig. 3-9	Counter figures of transverse residual stress by the different number of hits	65
Fig. 3-10	Numerical electropolishing after HFMI simulation	66
Fig. 3-11	Bead on steel plate specimen	67
Fig. 3-12	The bead on steel plate model used in FE HFMI simulation	68
Fig. 3-13	Comparison of experimental and simulation results	71
Fig. 3-14	Time history during HFMI simulation on the bead on steel plate model ...	71
Fig. 4-1	Three different details of welded joints [80]	75
Fig. 4-2	The geometry of the rat-hole detailed specimen [Unit: mm]	75
Fig. 4-3	The rat-hole model used in FE HFMI simulation	77
Fig. 4-4	Elastic thermal analysis [Unit: mm]	81
Fig. 4-5	Initial welding residual stress distributions by elastic thermal analysis	81
Fig. 4-6	The area of interest for defect tolerance considering crack opening-closing behavior	82
Fig. 4-7	Induced compressive residual stress to the rat-hole specimen with and without slit	83
Fig. 4-8	Residual stress distribution during HFMI treatment simulation	85
Fig. 4-9	Observation of change of slit after HFMI simulation	88
Fig. 4-10	Observation of opening-closing behavior of HFMI treated slit	91
Fig. 4-11	Out-of-plane gusset welded joints specimen	95
Fig. 4-12	The ICR apparatus [21]	95
Fig. 4-13	The PAUT system	96
Fig. 4-14	Detection methods and locations of cracks	96
Fig. 4-15	Observation of the fractured surface [Unit: mm]	97
Fig. 4-16	The relationship between echo height ratio and nominal stress	99
Fig. 4-17	Identified crack opening-closing behavior on pre-fatigue welded joints treated by HFMI	101
Fig. 5-1	The rat-hole model used in CPA [Unit: mm]	104
Fig. 5-2	Element types used to the mesh around the crack front [105]	105
Fig. 5-3	Crack front template found in [106]	105

Fig. 5-4	Compressive residual stress distributions from different slit depths	107
Fig. 5-5	Schematic diagram when CFT is used to the local model with crack depth of 2.0 mm.....	107
Fig. 5-6	J-integral loop at the crack tip [105]	109
Fig. 5-7	J-integral loop at the crack front in 3D volume [105]	109
Fig. 5-8	Generated stress distribution through thickness	113
Fig. 5-9	Investigation results of the influence of crack front template on SIF.....	113
Fig. 5-10	Assumed crack shape in HFMI treated welds.....	115
Fig. 5-11	Investigation results of SIF at the crack tip.....	117
Fig. 5-12	Crack propagation based on crack growth increment [117]	119
Fig. 5-13	Curve fitting of crack front points found in [88]	119
Fig. 5-14	Observation of crack shape after crack propagation [Unit: mm].....	120
Fig. 5-15	Results of fatigue life calculation in depth direction (Maximum stress 150 MPa, Minimum stress 15 MPa).....	122
Fig. 6-1	Experimental test results of HFMI treated pre-fatigued rat-hole specimen [80]	127

List of tables

Table 2-1	Examples of treatment procedure parameters for UIT and HiFIT [13].....	29
Table 3-1	Mechanical properties and chemical composition found in [95]	56
Table 3-2	Investigation cases on reduction of simulation time	58
Table 3-3	The list of investigation cases of under- and over-treatment	60
Table 3-4	Mechanical properties and chemical composition of SM400	67
Table 5-1	List of the crack shape in HFMI treated welds determined from the crack opening-closing behavior of the HFMI treated slit studied in Chapter 4	114

Abbreviations

TIG	Tungsten Inert Gas
HFMI	High Frequency Mechanical Impact
IIW	International Institute of Welding
LEFM	Linear Elastic Fracture Mechanics
CPA	Crack Propagation Analysis
ICR	Impact Crack-Closure Retrofit
SIF	Stress Intensity Factor
HP _{ICR}	Hammer Peening with ICR apparatus
PPP	Portable Pneumatic needle-Peening
JSSC	Japan Society of Steel Construction
SEM	Scanning Electron Microscope
FE	Finite Element
3D	Three Dimensional
UIT	Ultrasonic Impact Treatment
UP	Ultrasonic Peening
HiFIT	High Frequency Impact Treatment
PIT	Pneumatic Impact Treatment
AW	As-Weld
HAZ	Heat Affected Zone
DC	Displacement-Controlled
FC	Force-Controlled
ALE	Arbitrary Lagrangian-Eulerian
KE	Kinetic Energy
IE	Internal Energy
AE	Artificial strain Energy
JIS	Japan Industrial Standard
PAUT	Phased Array Ultrasonic Testing
CFT	Crack Face Traction
i.e.	In extenso that is
e.g.	For example

Acknowledgments

This thesis was carried out at the Department of Civil Engineering at Gifu University in Japan and the Department of Aeronautical and Vehicle Engineering at KTH Royal Institute of Technology in Sweden. I would like to express my thanks to all the people who helped with my works since I could not accomplish this doctoral thesis without the help by myself.

First and foremost, I would like to express my gratitude for Associate professor Koji Kinoshita at Gifu University, my supervisor, for supervising me during this doctoral thesis with outstanding guidance and long-time great support. Furthermore, I am heartily thankful to him for allowing me to study abroad. Thanks to you, I have many precious experiences through the study abroad.

Furthermore, I would like to express my gratitude for Professor Zuheir Barsoum at KTH Royal Institute of Technology, my co-supervisor, for allowing me to discuss my idea and offering me chance to gain valuable knowledge in the field of finite element analysis. I also would like to thank him for providing a good work environment during my extended stay at KTH from September 1, 2019, to March 15, 2022. I am heartily thankful to him for his excellent guidance, valuable advice, support, and encouragement. I could not accomplish this doctoral thesis without those.

I would like to acknowledge Professor Uchida Yuichi, Professor Koichi Kobayashi, and Professor Minoru Kunieda at Gifu University for taking a lot of time to review this thesis and to have a pre-examination and a PhD defense. Their valuable comments and questions are quite precious for this doctoral thesis. I am very grateful for their guidance and contribution.

As for my extended stay at KTH, I thank all my colleagues who supported me in discussing this thesis, Dr. Mansoor, Dr. Rami, Mr. Jinchao, Mr. Martin, Ms. Sara, Mr. Gustav, Mr. Joel, and Mr. Johan. Besides, I thank all colleagues for accepting me into the group and inviting me to many activities.

I wish to give special big thanks to research members and graduated members in Gifu University, Mr. Akiyama, Dr. Hatasa, Assistant professor. Hasuike, Assistant professor. Yamamoto, Dr. Kozuka, Mr. Inoue, Mr. Suzuki, Mr. Iwata, Mr. Yano, Mr. Sakurai, Mr. Obara, Ms. Kato, Mr. Mezaki, and Mr. Sasaki for good colleagues. I would like to give special thanks to Project assistant professor. Ono, Mr. Sugawa, Mr. Ohira, and Mr. Takahashi, who are the members of the fatigue group and were studying together.

I would like to thank my father Masao, my mother Mayumi, older brother Masanori, and younger sister Arisa for their extended support.

Abstract

Many steel bridges around the world were constructed several decades ago, with a current need for continuous maintenance where the major challenge in old steel bridges is fatigue cracks. High Frequency Mechanical Impact (HFMI) has been gathering a lot of interest nowadays as one of the post-weld fatigue strength improvement techniques. HFMI treatment is conducted to the weld toe using a hardened pin or hammer with an operation frequency of more than 90 Hz. Owing to that, beneficial compressive residual stresses can be introduced locally in/around the weld toe, and therefore the fatigue strength of the welds can be improved remarkably. On the other hand, utilization of HFMI treatment for repairing and life extension of pre-fatigued welds of the fatigue-damaged steel bridges has been gained interest as a robust method nowadays. Although fatigue cracks are inevitably involved in the HFMI treated welds and become “defects” against the HFMI treated welds when HFMI treatment is performed to the pre-fatigued welds, defect tolerance is not clearly stipulated in the International Institute of Welding (IIW) recommendation for HFMI treatment. Therefore, the objective of this thesis is to propose defect tolerance of HFMI treated welds in bridge application for life extension based on numerical Finite Element (FE) simulations.

In chapter 1, the background and the problem statement were given. The objects of this thesis were also explained.

In chapter 2, the review of literature including author’s previous study was conducted, and the subjects that are addressed in the subsequent chapters of this thesis were determined based on the review.

In chapter 3, the validity of 3D FE HFMI simulations using an isotropic hardening model for residual stress estimation was verified for two models: flat and bead on steel plates. The HFMI simulations were carried out to the flat steel plate model, where feed rate and the number of hits of the HFMI indenter were varied in order to investigate the influence of different HFMI treatment processes, such as under- and over-treatment on the residual stress state. The results show that a high feed rate can influence the residual stress state near the treated surfaces, whereas the number of hits is independent of the amount of induced residual stress. Then, the HFMI simulations were carried out to the bead on steel plate model. The results show a reasonable estimation of the residual stresses near the treated surface compared with experimental measurement results, even when welding residual stress are not considered in the model.

In chapter 4, the effect of HFMI treatment on pre-fatigued welds and crack opening-closing behavior in HFMI treated welds were investigated based on the HFMI

simulation using a combined hardening model. A rat-hole weld, which is one of the fatigue-prone details in steel bridges, was used in the HFMI simulation. In order to simulate initial cracks, the detailed rat-hole models included a rectangle slit with different depths in their weld toes. Induced compressive residual stress, change of slit geometry, and opening-closing behavior of the HFMI treated slit were investigated numerically. The results show that the slit depth influences the amount of induced compressive residual stress at the slit tip and the amount of closed slit depth. The results also show that the slit closed by the HFMI treatment simulation opened from the inside prior to the treated surface. Additionally, the crack opening-closing behavior was investigated experimentally using pre-fatigued out-of-plane gusset welded joints treated by Impact Crack-Closure Retrofit (ICR) treatment, with the aid of an ultrasonic testing system. The results indicate that the behavior can be identified based on the change of echo height ratio from the crack, and similar crack opening-closing behavior was observed in the FE simulations. From both experimental and numerical investigations, the behavior in pre-fatigued welds treated by HFMI could be studied successfully.

In chapter 5, the defect tolerance of HFMI treated welds in bridge application for life extension was investigated in 3D Crack Propagation Analysis (CPA) based on Linear Elastic Fracture Mechanics (LEFM), using the rat-hole models with different fatigue crack depths in HFMI treated welds. At first, compressive residual stress introduced by HFMI treatment simulation was considered over those cracks faces in HFMI treated welds. Crack opening stress at the crack tip in HFMI treated weld was investigated considering the crack opening-closing behavior. The results indicate that cracks in HFMI treated welds would propagate after the HFMI treated surface crack is opened. Then, CPA based on LEFM was carried out under fatigue load. The results show that it is difficult to represent crack propagation behavior in a deeper region in the 3D CPA considering compressive residual stress state. Finally, the fatigue life was calculated based on the CPA results. The calculated results demonstrated that the life extension can be obtained effectively when HFMI treatment is performed to pre-fatigued welds including fatigue cracks that are shallower than 1.5 mm in depth.

In conclusion, in chapter 6, the author proposes fatigue cracks that are shallower than 1.5 mm in depth as a defect tolerance of HFMI treated rat-hole welds for fatigue life extension based on the numerical FE simulation results. Furthermore, the author recommends the defect tolerance of HFMI treatment based on the current numerical and experimental studies results.

Chapter 1

Introduction

1.1 Background

Many steel bridges around the world are used in terms of lower construction costs than other materials, faster construction, especially in urban areas, and feasible longer span beam length due to lightweight structure, etc. Welding is often used for the bridge members' joints in steel bridge applications. Advantages of using welding are that arbitrary shapes of the bridge members can be jointed easily, the total weight of the bridges can be reduced in comparison with ones using bolted or riveted joints, and also construction costs can be saved. Historically, the welded joints were incorporated in earnest into a bridge fabrication around 100 years ago [1]. Afterward, the welded joints were frequently adopted into the fabrication [2] with advancing welding technology. During the 1950s to 1970s, many welded bridges were built because of the high demand for development in road and railway networks around the world. For instance, in Japan, the welded bridges, with a span length exceeding 15 m, that were constructed during that period are around 40 % of the total number of the welded bridges [3] (see Fig. 1-1a). Hence, half of Japan's existing welded bridges is over 50 years old. Similarly, in European countries, the existing welded railway bridges are from 50 to 100 years old that are about 40 % and are over 100 years old that are more than 25 % [4] (see Fig. 1-1b). Such welded bridges have been subjected to higher traffic volumes and weights than those for which they are designed when its construction, and thus it is supposed that their fatigue lives have already been reached and/or exceeded due to fatigue damage accumulation. Hence, fatigue crack initiation is concerning in the older welded bridges. Therefore, a current need for continuous maintenance where the major challenge in older welded bridges is fatigue cracks.

Fatigue cracks often occur in the welded joints, which are sensitive to cracking because of stress concentration due to geometric complexity, unfavorable tensile residual

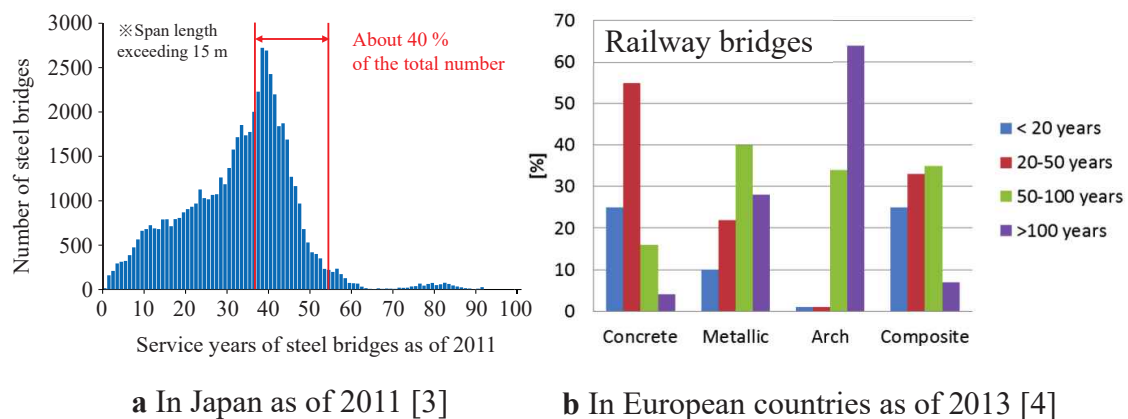


Fig. 1-1 Age profiles of welded steel bridges

stresses induced by welding, and weld defects such as undercuts, spatter, or inclusions. Once fatigue cracks occur in the welds, they continue to propagate steadily under repeated or fluctuating loading due to service loads, resulting in fracture of bridge members as time advances. Indeed, many inspectors and/or administrators have detected various size of fatigue cracks in the welds in existing steel bridges [5]. When fatigue cracks propagate to the bridge member and are so large that they are judged as causing danger to the bridge's performance, a retrofitting treatment is immediately performed to the damaged bridge member. For instance, crack tips in the damaged bridge member are drilling and bolting, i.e., stop hole with bolting method [5]. On the other hand, when fatigue cracks are so small as stay in the welds, they are usually judged as not causing immediate danger and left due to repair costs. In the current state that the number of fatigue-damaged steel bridges is rapidly increasing, it can be expected that hundreds and thousands of such small cracks have been left without any repair and/or retrofit treatment. When all of the cracks start to propagate rapidly and their influence is prominent, immediate repair/retrofit treatment would be necessary because the bridge's performance could be reduced dramatically. If treatment is delayed, a serious failure like collapse would occur. An immense amount of time, enormous costs, and many workforces would be necessary once serious failure occurred. Therefore, taking countermeasures is important against the fatigue-damaged welded steel bridges before their damages are prominent.

Classically, some techniques, such as grinding [6] and Tungsten Inert Gas (TIG)-remelting [7] have been proposed for repairing small cracks in the welds. Grinding is that the fatigue cracks in the welds are removed using either a disc or burr grinders. The cracking area of the welds needs to be grounded step by step, and magnetic particle inspection should be applied if the crack tip is completely removed or not. The gouge created by grinding should be targeted with a 2.5:1 slope, and finish grinding should be performed parallel to the applied cyclic stress. Scratches introduced by the grinding into the ground area will work as defects and crack initiation site, and hence, a careful finish treatment is necessary. TIG-remelting is that the fatigue cracks in the welds are remelted using welding, and it is possible to fuse the toe cracks that are from 3 to 4 mm in depth [7]. However, the effectiveness of TIG-remelting requires a high technical skill and adequate fusion depth at the cracked welds, both of which may be difficult to attain on-site. Accordingly, grinding and TIG-remelting largely depend on an operator's technical skill. Insufficient treatment would introduce unwanted damaged against the treated/repared welds. Consequently, secondary treatment may be necessary. Accordingly, grinding and TIG remating have advantage and disadvantage for repairing small cracks in the welds.

On the other hand, several studies on improvement of the fatigue strength of the welded joints have been performed using the post-weld improvement techniques. High Frequency Mechanical Impact (HFMI) has been emerged as a reliable, efficient, and user-friendly post-weld fatigue strength improvement technique of welded structures and has been gathering a lot of interest nowadays [8, 9]. HFMI treatment is a local cold working process to the weld toe using a hardened pin or hammer with an operation frequency of more than 90 Hz. High frequency operation makes impact energy increase, which is determined by a frequency and a driven mass of the hardened pin or hammer per HFMI impact. Due to that, HFMI treatment can be effectively performed to the welds, and unwanted tensile residual stresses in the welds can be removed and beneficial compressive residual stresses can be locally introduced in/around the region of impact. In addition, HFMI treatment improves the local weld geometry and surface quality involving work hardening. Numerous studies [10-12] have investigated the effect of HFMI treatment on the welds and demonstrated that HFMI treatment can improve their fatigue strengths remarkably especially for low fatigue strength details. The fatigue strength improvement effect is due to the combination of three effects: introducing high compressive residual stress in/around the region of impact, reducing high stress concentration of the weld toe, and causing work hardening [13]. In 2016, the International Institute of Welding (IIW) published a recommendation for HFMI treatment for improving the fatigue strength of the welded joints [13]. Hence, HFMI treatment is expecting to become one of desirable methods for fatigue life extension of pre-fatigued welds in the fatigue-damaged steel bridges. Although fatigue cracks are inevitably involved in the HFMI treated welds and become “defects” against the HFMI treated welds when HFMI treatment is performed to the pre-fatigued welds, defect tolerance is not clearly stipulated in the IIW recommendation for HFMI treatment [13]. These defects could influence the effect of life extension by HFMI treatment. Hence, it is necessary to investigate as the size of cracks that HFMI treatment can tolerate and the defect tolerance of HFMI treated welds in bridge application for life extension, to use HFMI techniques for the pre-fatigued welds of the fatigue-damaged steel bridges as a robust life extension method.

1.2 Objective

The objective of this thesis is to propose defect tolerance of HFMI treated welds in bridge application for life extension based on numerical Finite Element (FE) simulations.

1.3 Disposition of this thesis

In line with the objective, this thesis can be divided into six chapters, including this chapter. The disposition of this thesis is shown in Fig. 1-2.

Chapter 2 – Review of literature including author’s previous study

First, literature including author’s previous study was reviewed to determine the subjects that are addressed in subsequent chapters of this thesis. Background of the state-of-the-arts hammer and needle peening and HFMI techniques, and their experimental investigations were reviewed and discussed. Numerical investigations on HFMI simulation, such as FE modeling, optimum parameters, and settings for the HFMI simulation were also reviewed. Experimental investigations on life extension of pre-fatigued welds treated by hammer and needle peening and HFMI techniques were reviewed. Linear Elastic Fracture Mechanics (LEFM) was briefly introduced, and fatigue life estimation of pre-fatigued welds treated by HFMI using LEFM was reviewed and discussed.

Chapter 3 – Validity of HFMI simulation for residual stress estimation using a flat and bead on steel plates models

Prior to the investigations regarding defect tolerance of HFMI treated welds in bridge application for life extension, the validity of 3D FE HFMI simulations using an isotropic hardening model for residual stress estimation was verified for the two models: flat and bead on steel plates models. Firstly, the mass scaling method was applied to the simulation model in order to reduce the HFMI simulation time. The influence of the mass scaling on the HFMI simulation time, the residual stress state, and the energy balance during the HFMI simulation was examined. Secondly, the HFMI simulations were performed on the flat steel plate model, where feed rate and the number of hits of the HFMI indenter were varied in order to investigate the influence of different HFMI treatment processes, such as under- and over- treatment, on the residual stress state. In addition, the influence of electropolishing after the HFMI simulation on the residual stress state was examined. Finally, Portable Pneumatic needle-Peening (PPP) was experimentally performed to the bead on steel plate, and introduced residual stress was measured with the aid of X-ray diffraction method. Based on the experimental study, the HFMI simulations using the isotropic hardening model were carried out on the bead on steel plate model, and simulated residual stress was compared with the experimental measurement result in order to investigate the applicability of the isotropic hardening

model for residual stress estimation.

Chapter 4 – Defect tolerance analysis considering crack opening-closing behavior in HFMI treated welds

After the HFMI simulation was verified in the Chapter 3, the effect of HFMI treatment on pre-fatigued welds and crack opening-closing behavior in HFMI treated welds were investigated in 3D FE HFMI simulations using a combined hardening model. The rat-hole weld, which is one of the fatigue-prone details in bridges, was used in the HFMI simulation. In order to simulate initial cracks, the detailed rat-hole models included a rectangle slit with different depths in their welds toes. Initial welding residual stress was estimated using an elastic thermal analysis. Then, the HFMI simulation and subsequent initial axial cyclic loading was conducted. Induced compressive residual stress, change of slit geometry, and opening-closing behavior of the slit after HFMI simulation were investigated numerically.

Additionally, the crack opening-closing behavior was investigated experimentally using a pre-fatigued out-of-plane gusset welded joint treated by Impact Crack-Closure Retrofit (ICR) treatment. The crack opening-closing behavior under axial loading was investigated using a phased array ultrasonic testing system and identified based on the change of echo height ratio from the crack.

Chapter 5 – Life extension analysis considering crack opening-closing behavior in HFMI treated welds

The HFMI simulation and subsequent CPA based on LEFM were carried out to investigate defect tolerance of HFMI treated welds in bridge application on life extension. The rat-hole models with different defect depths in the HFMI treated welds were used in the CPA based on LEFM. At first, the compressive residual stress state introduced by HFMI treatment simulation was considered over crack faces in HFMI treated welds. Crack opening stress at the crack tip in HFMI treated weld was investigated considering the crack opening-closing behavior studied in Chapter 4. Then, CPA based on LEFM was carried out under fatigue load and crack propagation behavior was studied. Finally, the fatigue life was calculated based on the CPA results, and the defect tolerance of HFMI treated welds for life extension was investigated.

Chapter 6 – Conclusions

Conclusions obtained from the numerical FE simulations in this thesis were summarized. Based on the investigation of numerical FE simulations, the defect tolerance

of HFMI treated rat-hole welds in bridge application for fatigue life extension is proposed. In addition, the defect tolerance is recommended based on the numerical investigation results studied in this thesis and the previous experimental investigation result.

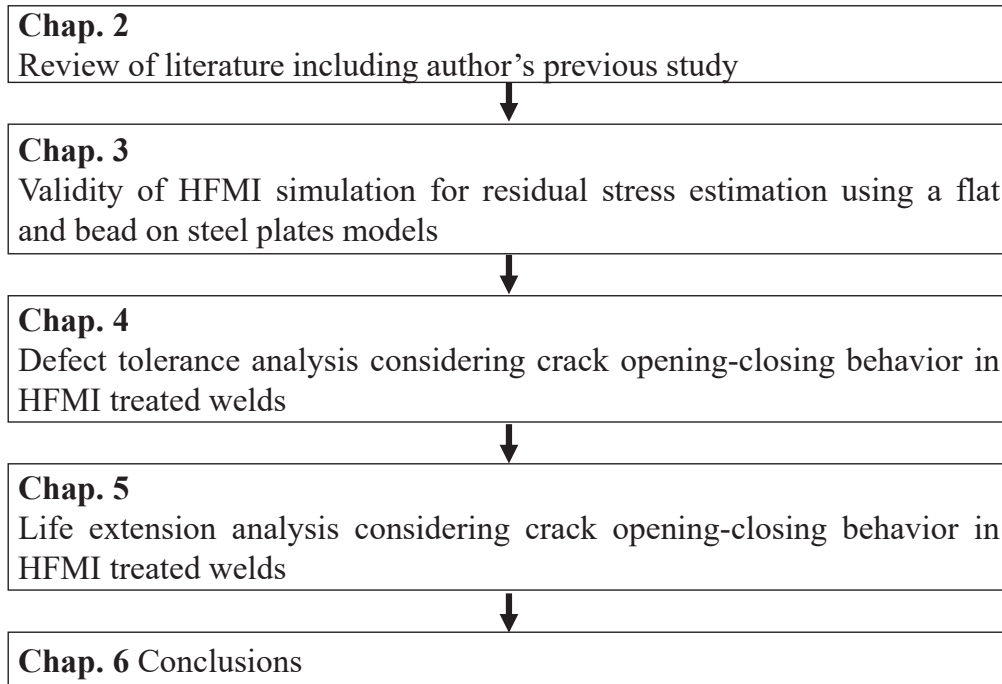


Fig. 1-2 Disposition of this thesis

Chapter 2

Review of literature including authors' previous study

2.1 Introduction

The objective of this chapter is to determine the subjects that are addressed in the subsequent chapters of this thesis through review of literature including author's previous study. Backgrounds of the state-of-the-arts peening techniques and High Frequency Mechanical Impact (HFMI) and Finite Element (FE) modeling of HFMI were briefly introduced. Then, the effect of HFMI techniques on life extension of pre-fatigued welds were reviewed and discussed. Finally, Linear Elastic Fracture Mechanics (LEFM) was briefly introduced, and fatigue life estimation of pre-fatigued welds treated by HFMI based on LEFM was reviewed and discussed.

2.2 Peening techniques

In steel bridge applications, welding has been used for their joints. As a result, high tensile residual stresses are produced in/around the welded joint. Therefore, the stress subjected to the weld becomes fully tensile stress even if the applied stress has partly compressive stress. The fatigue strength of the weld is decreased due to the presence of tensile residual stress and hence can be improved when it is removed. Furthermore, the benefit of fatigue strength improvement can be greater when compressive residual stresses are introduced in the weld.

Peening technique is a cold working process that plastically deforms a steel's surface locally by impacting it with a steel needle, hammer, or small ball/shot. During peening treatment, unwanted tensile residual stress is removed, and compressive residual stress in/around the region of impact is introduced. Hence, such peening treatment using the steel needle, hammer, or small ball/shot are well known as the residual stress modification technique. Currently, the recommendation published by International Institute of Welding (IIW) [13] classifies hammer and needle peening and shot peening as the residual stress modification technique, as shown in Fig. 2-1. Among them, hammer and needle peening can effectively eliminate tensile residual stress in the weld toe and introduce compressive residual stress in/around the region of impacts. Hammer and needle peening cause heavy material deformation and smooth the seam between the weld and the base plate, resulting in reducing the stress concentration factor of the welds, which is an additional beneficial effect. On the other hand, there is a latest development of those peening using ultrasonic technology, called HFMI. It can further improve the local weld geometry and the finish surface quality than hammer and needle peening. Therefore, HFMI has been much interest in improving the fatigue strength of the welds of the steel bridge applications.

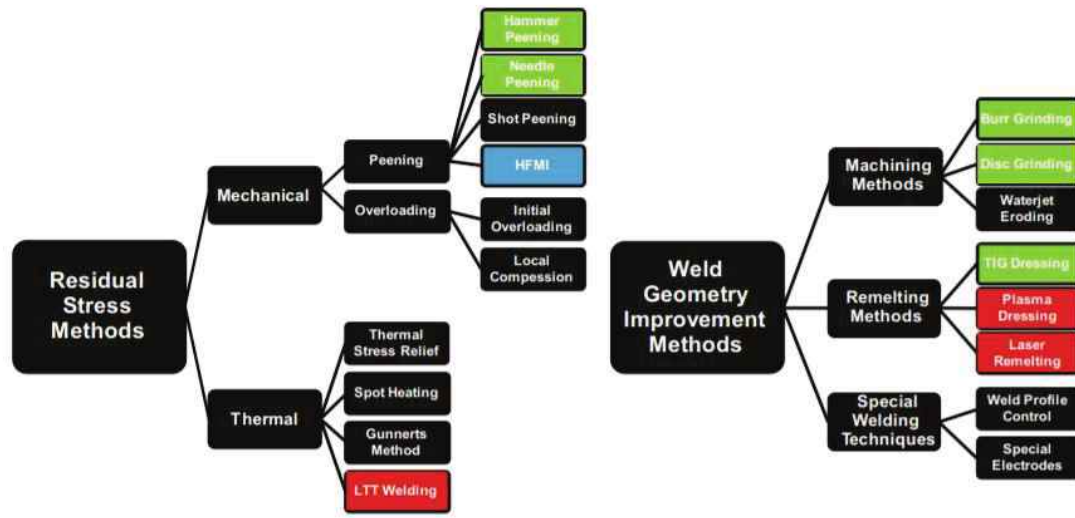


Figure 2-1 Overview of different improvement techniques on the market [13]

2.2.1 Hammer and needle peening

Hammer and needle peening are well-known as the residual stress modification techniques. In recent years, a hammer and needle peening have been developed originally in Japan and have been often used in-country. In this section, their backgrounds were briefly introduced. Note that, hereafter, previous type of hammer and needle peening techniques is called classical ones in order to distinguish with the developed ones.

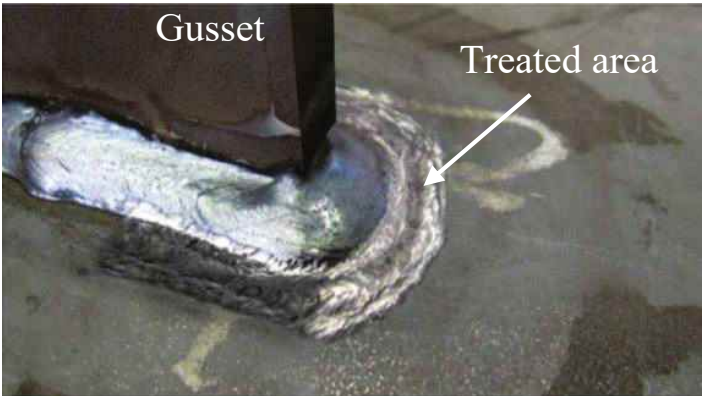
The classical hammer peening is shown in Fig. 2-2. The classical hammer peening aims to produce plastic deformation in the weld toe and introduce beneficial compressive residual stress in/around the region of impact. Power source is often compression air. Hammer peening treatment is performed to an object with operation frequency in the range of 25 to 100 Hz. For the treatment, hardened steel pins which have rounded hemispherical tips with diameters of between 6 and 18 mm [15] are used. The quality control is based on the number of passes and an indentation depth. Knight et al. [16] recommended four passes along the welds and indentation depth of about 0.6 mm in mild steel. Furthermore, in order to prevent the formation of a ditch or a crack-like defect in the treated welds due to improper contact between the hammer peening tool and the weld toe, a surface treatment, called cleaning using a grinder, is recommended [14, 17, 18].

Developed hammer peening is shown in Figs. 2-2b and 2-2c. This is called Hammer Peening with Impact Crack-Closure Retrofit apparatus (HP_{ICR}) [19, 20]. HP_{ICR} is performed to the welds using an apparatus which was originally developed by Yamada et al. [21] for ICR treatment. The original purpose of development of ICR treatment is to

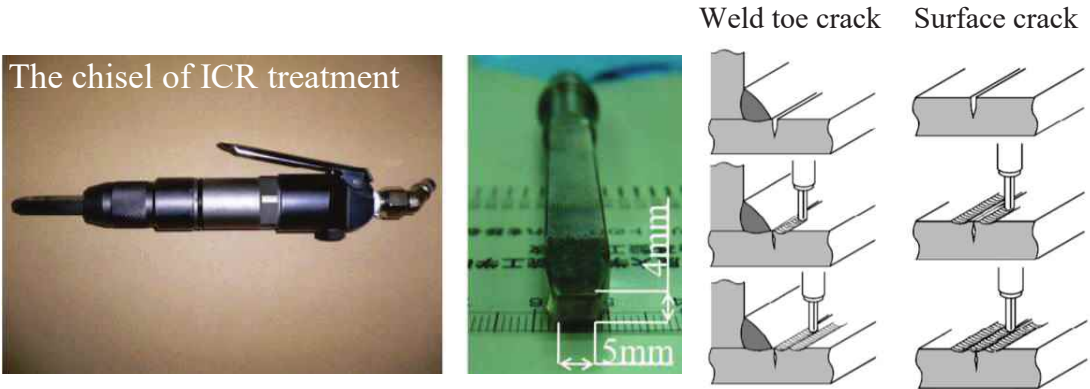
close fatigue cracks and to retrofit fatigue damage on a base plate and/or in welds. In this context, “close fatigue cracks” means causing plastic deformation near the crack in order to close crack opening by using impact air tool [21]. Hence, in order to close fatigue cracks opening effectively by the ICR treatment, ICR apparatus has rectangle chisel



a Classical hammer peening [14]



b Around the weld toe after HP_{ICR} treatment [20]



c ICR treatment [21]

Figure 2-2 Hammer peening

whose tip is ground to a flat surface of 4×5 mm with rounded corners. This is enable to cause large plastic deformation on the base plate near the cracked surface [22], see Fig. 2-2**b**. The power source is compression air. The ICR and HP_{ICR} treatment is performed to an object with operation frequency of around 90 Hz. The HP_{ICR} treatment does not make the ditch or the crack-like defect at the treated welds as is only performed on the base plate next to the welds. Hence, the cleaning using the grinder is not necessary before the treatment. The quality requirement of the HP_{ICR} treatment is judged based on two geometrical features: a section area of depression created by the HP_{ICR} and a distance between a weld seam and the HP_{ICR} created depression edge. Those geometric features strongly affect the amount of induced compressive residual stress [20, 21]. With satisfying those geometric features, the fatigue strength of the welded joint can be significantly improved, as seen in [23].

The classical needle peening is similar to the classical hammer peening except for using a different peening tool. A bundle of steel rods of around 2 mm with rounded corners shown in Fig. 2-3**a** is used. Due to that, the classical peening cannot treat the weld toe directly. Consequently, the fatigue strength improvement effect is generally slightly smaller than the classical hammer peening [24].

Developed needle peening is shown in Fig 2-3**b**. This is called Portable Pneumatic needle-Peening (PPP) [25], consisting of a peening tool and a control box. The peening tool has a 1.5 mm radius tool tip, and it is relatively sharper than the classical hammer and needle peening. Hence, the PPP can directly treat the welds and intensively cause plastic deformation there. The PPP treatment is performed to an object with operation frequency of around 90 Hz. The power source is compression air, and the control box is able to adjust the amount of compression air provided to the peening tool.



a Classical needle peening [14]

b Equipment of PPP [25]

Figure 2-3 Needle peening

Thereby, a stable treatment can be achieved. When it comes to quality control of the PPP treatment, the provider requires that the travel speed of PPP treatment is 0.3 m/min. On the other hand, the provider recommends that the travel speed is investigated considering weld geometry to be treated before PPP treatment is conducted.

Inoue et al. [25] carried out axial loading fatigue tests using out-of-plane gusset welded joints treated by PPP under two different travel speed levels: 0.2 m/min and 0.1 m/min. They demonstrated that the fatigue strength by PPP under 0.1 m/min shows higher than that under 0.2 m/min. Hence, travel speed significantly affects fatigue strength improvement. On the other hand, they did not investigate the influence of the number of passes on the fatigue strength improvement effect. It could be an important factor for quality control of PPP treatment since hammer peening treatment requires certain number of passes as its quality requirement, as shown in [16].

Regarding that, the authors investigated the influence of both travel speed and the number of passes on the fatigue strength. To investigate the influence, and PPP treatments were performed out-of-plane gusset welded joints under the travel speed with 0.1 m/min and 1 or 2 passes and it with 0.2 m/min and 2 passes. The results demonstrated that the PPP treatment under 0.2 m/min and 2 passes shows higher fatigue strength improvement effect than that other quality control cases, as shown in Fig. 2-4. Hence, it is necessary to perform PPP treatment under sufficient travel speed and the number of passes from fatigue strength improvement points of view. Moreover, the fatigue strengths by 0.2 m/min and 2 passes correspond with those by 0.1 m/min and 2 passes. From this, it can be here concluded that PPP treatment under travel speed under 0.2 m/min and 2

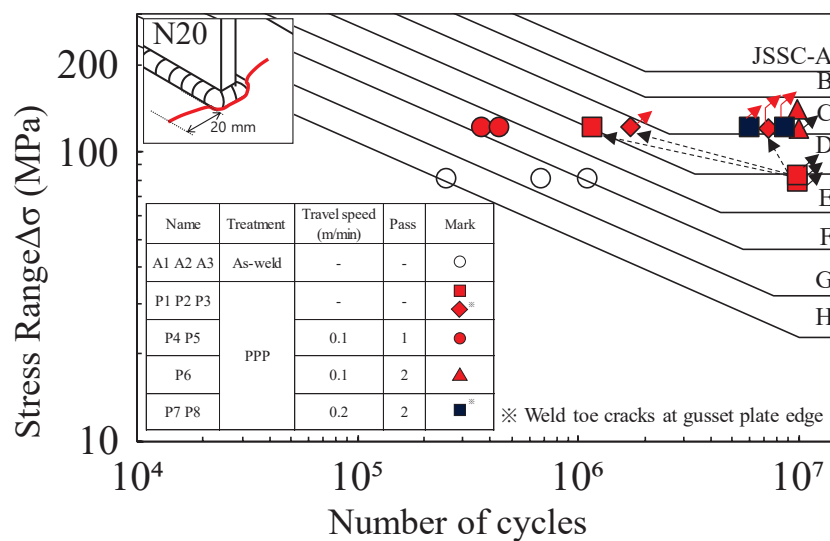


Figure 2-4 Fatigue test results by using PPP treated out-of-plane gusset welded joints in the author's previous study

passes is sufficient quality control for improving the fatigue strength of out-of-plane gusset welded joint.

2.2.2 High frequency mechanical impact

HFMI has been the latest development of the hammer and needle peening and has emerged as a reliable, effective, and user-friendly peening method. It is a generic term to describe related innovative peening technology that improves the fatigue strength of the welded structures by locally modifying the residual stress state, improving the local weld geometry and the surface quality.

Historically, innovation and development of the peening methods using ultrasonic technologies, such as piezoelectric and magnetostrictive oscillating systems (see Figs. 2-5a and 2-5b) is widely attributed to Statnikov, a researcher in Ukraine [27]. The peening methods implemented those ultrasonic technologies are well-known as Ultrasonic Impact Treatment (UIT) and Ultrasonic Peening (UP).

Since 2002, IIW Commission XIII on fatigue of welded components and structures has published many documents reporting on “High Frequency Mechanical Impact” technology development and experimental studies. In the published documents, several peening methods, including UIT and UP, have been emerged, e.g., High Frequency Impact Treatment (HiFIT), and Pneumatic Impact Treatment (PIT), see Fig. 2-6 [28]. In 2010, several related peening methods were categorized using the generic term “HFMI” by IIW Commission XIII. Finally, in 2016, the IIW published the IIW recommendation for HFMI treatment, presenting an overview of HFMI techniques existing today on the market and their proper procedures, quality assurance measures, and documentation [13].

HFMI devices employed alternate power sources, for example, ultrasonic piezoelectric elements, magnetostrictive elements, or compression air. However, in all cases, the working principle is identical: cylindrical indenters are accelerated to a component or structure with high frequency of more than 90 Hz [13]. The beneficial effect of high frequency is an increase of an impact energy per HFMI impact, which is determined by a velocity (e.g., frequency) and a driven mass. Hence, although HFMI devices are compact in comparison with the devices of the classical hammer and needle peening, see Figs. 2-2a, 2-3b and 2-6, HFMI can archive high intensity treatment. Indenter of HFMI equipment is made of a high strength steel, provided with different diameters in a range of 2 to 5 mm, tip geometries, and multiple indenters, see Fig. 2-7. This indenter is sharper than those of the classical hammer and needle peening and hence can efficiently cause plastic deformation in the region of impact. As a result, the space

between alternate impacts on a workpiece is very small, achieving a finer surface finish [13].

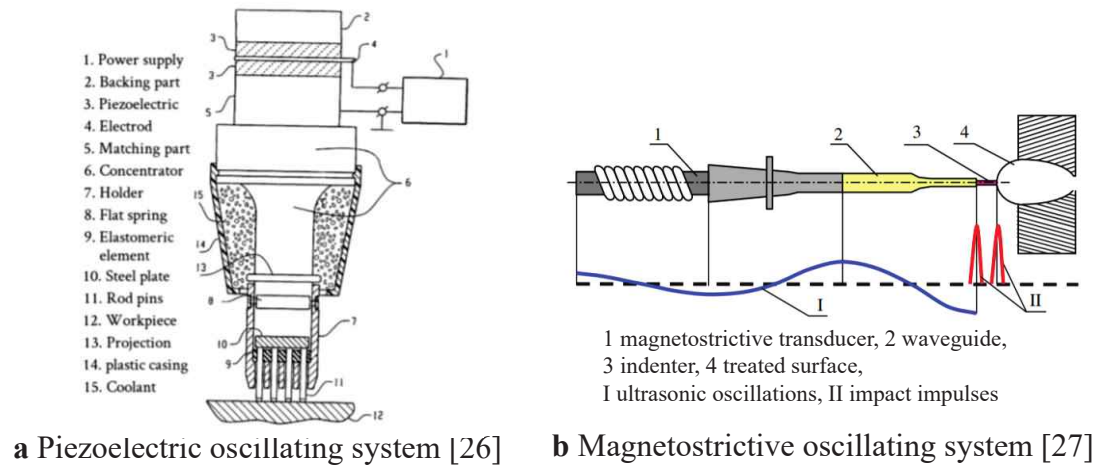


Figure 2-5 Schematic diagram of HFMI using ultrasonic technologies



Figure 2-6 Examples of four different HFMI devices [28]



Figure 2-7 Examples of tip geometries and multiple indenter [29]

HFMI treatment can give several beneficial effects to the welded joints. Many researchers have investigated those beneficial effects and explained them in terms of compressive residual stress, geometric modification, and material hardening. Figure 2-8 shows a schematic image of main benefits by HFMI treatment. HFMI treatment involves a cold working process and makes an indentation against weld seam. The indentation depth is generally in a range of 0.2 to 0.5 mm [30-33]. Due to HFMI impacts, large plastic deformation is caused in the region of impact, and compressive residual stresses are induced down to a depth of around 1.0 to 2.0 mm from the HFMI treated surface [34-36]. The amount of introduced compressive residual stress tends to depend on a base material yield strength. Hanji and Anami demonstrated that the amount of introduced compressive residual stress at 2 mm away from the depression edge by UIT was more than 60 % of the base material yield strength [37]. In addition to the introduction of compressive residual stress, material hardening occurs around the treated region. The Vickers hardness measurement showed that HFMI treatment increase a material hardness of the welds up to around 300 μm in depth, and it is harder maximum of 1.3 times in comparison with that of As-Welded (AW) state [38]. Lefebvre et al. [9] investigated which effects most contributed to the fatigue strength improvement of the welds and concluded that introduced compressive residual stress plays an important role and geometric modification is of secondary importance. In contrast, a change of microstructure due to material hardening does not seem to affect the fatigue strength improvement effect [9]. The importance of compressive residual stress can be seen from the fatigue design curves for HFMI treatment given by the IIW recommendation [13].

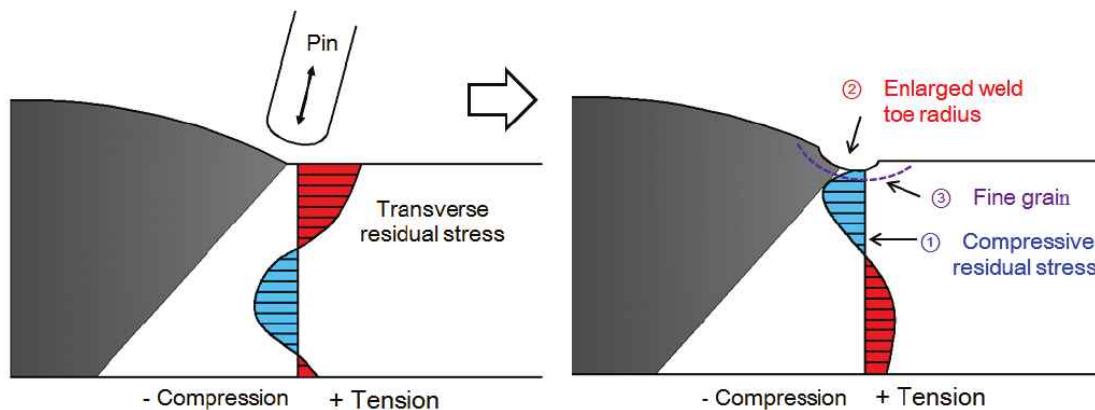


Figure 2-8 Schematic image of main benefits of HFMI [30]

The IIW recommendation [13, 14] provides the fatigue design curves for AW and HFMI treated states. Figure 2-9a shows the fatigue design curves for AW state. The fatigue design curves are represented by the number of cycles in the horizontal axis and nominal stress in the vertical axis. The fatigue strength of the AW state is classified or

categorized as FAT class which characterizes the fatigue strength at 2 million cycles and expresses in MPa. The slope coefficient is $m=3$ for the number of cycles inferior to the knee point where is at 10 million cycles. After the knee point, the slope is equal to $m=22$. Fatigue strength of HFMI treated state is determined depending on the effect of the base material yield strength and stress ratio, based on a FAT class of AW state, as shown in Fig 2-9b. Figure 2-10 shows “Staircase” improvement for the HFMI treated welds. Depending on the base material yield strength, FAT class is increased per one FAT for every 200 MPa. The IIW recommendation covers grade steels ranging from 235 to more than 950 in MPa. The benefit of HFMI treatment can be effective especially for low fatigue strength details that are classified into FAT50 to FAT90. On the other hand, stress ratio negatively affects FAT value. More specific detailed information regarding how to determine FAT class of HFMI treated state, see [13].

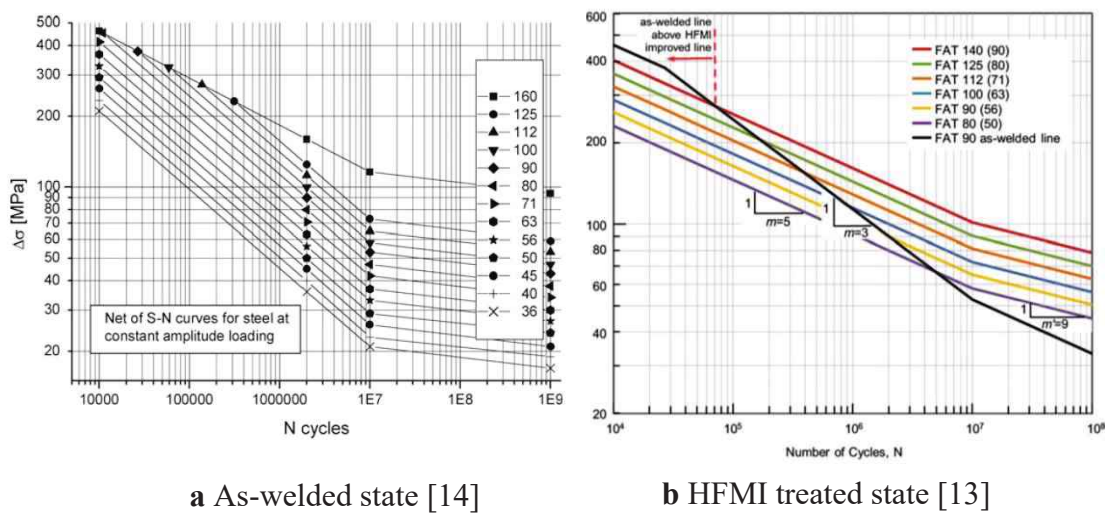


Figure 2-9 Fatigue design curves proposed by IIW recommendations

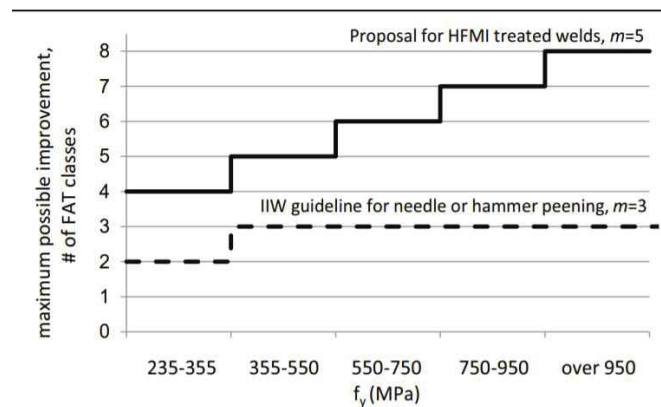


Figure 2-10 “Staircase” improvement for HFMI treated weld [13]

Proper HFMI treatment procedures and quantitative quality measurements are quite important to introduce compressive residual stress to the welds and improve the fatigue strength of the welds. IIW recommendation for HFMI treatment provides several specific HFMI treatment procedures, see Table 2-1 [13]. At first, HFMI treatment should be continuously carried out in moving direction with proper travel speed while HFMI tool is oscillated in forward and backward against the moving direction, as shown in Fig 2-11. For example, travel speeds of UIT and HiFIT are 3~5 mm/s and 5~25 mm/s, respectively. The orientation of the HFMI tool is kept about 30 to 80 digs with respect to the weld to be treated. A minimum of 5 passes is required for UIT. Time of HFMI treatment depends on the weld length to be treated. It would be a few minutes in the case a boxing weld toe is treated by HFMI.

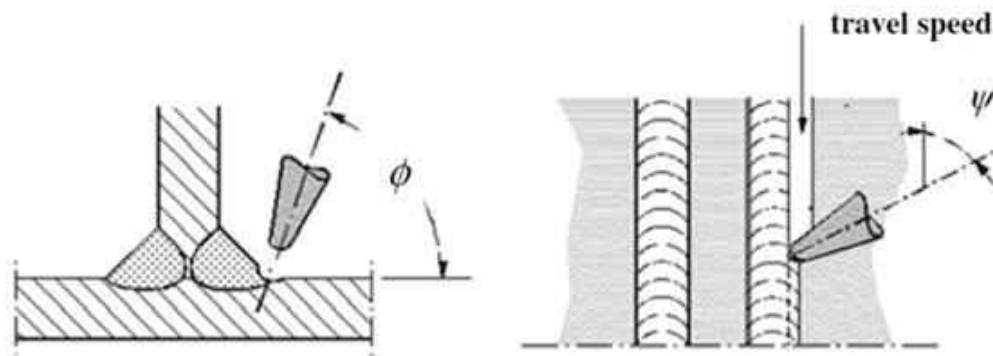


Figure 2-11 Orientation of HFMI tool with respect to the weld [13]

Table 2-1 Examples of treatment procedure parameters for UIT and HiFIT [13]

Parameter	HFMI tool	
	High frequency impact treatment (HiFIT) [22]	Ultrasonic impact treatment (UIT) [21, 23]
Power source	Pneumatic	Ultrasonic magnetostrictive
Number of indenters	1	1-4
Angle of the axis of the indenters with respect to the plate surface, ϕ (see Fig. 6)	60°-80°	30°-60° [21] 40°-80° [23]
Angle of the axis of the indenters with respect to the direction of travel, ψ (see Fig. 6)	70°-90°	90° (all pins should contact the weld toe)
Working speed	3-5 mm/s	5-10 mm/s [21] 5-25 mm/s [23]
Other		The self-weight of the tool is sufficient [21, 23] Minimum of 5 passes [23]

The groove geometries after HFMI treatment should be inspected visually first in accordance with the IIW recommendation [13]. Figure 2-12 shows an example of visual inspection of HFMI treated welds. Proper HFMI treatment makes a smooth finish and shiny groove without lines which is one of the characteristics of adequately treated welds. A crack-like defect in the groove shown in Fig. 2-12 should be avoided since fatigue cracks will initiate from the defect. This defect indicates that the weld seam line is not treated satisfactorily by HFMI treatment. In addition to the visual inspection, quantitative quality measurement should be conducted with respect to the indentation depth and width by HFMI treatment, as shown in Fig. 2-13. The indentation depth is defined as the distance from the base plate to the groove bottom, and the groove width is indicated as the HFMI treated width. Mostly, an optimum HFMI treatment creates the indentation depth from 0.2 to 0.6 mm and the width from 2.0 to 5.0 mm [13]. However, an excessive HFMI treatment of a weld toe should be avoided because it makes flaking type defects on the region of impact, and these could serve a crack initiation [39]. Thus, the remarkable fatigue strength improvement effect explained in previous paragraphs has relied on the proper HFMI treatment and quantitative quality measurement.

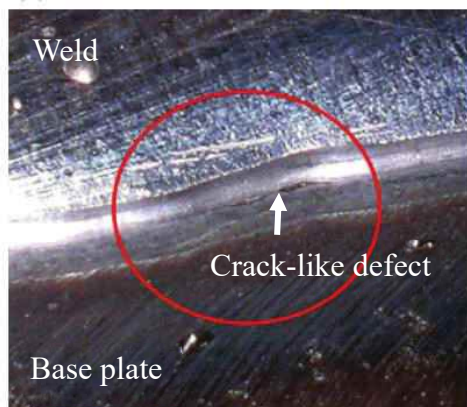


Figure 2-12 Examples of visual inspection of HFMI treated welds [13]

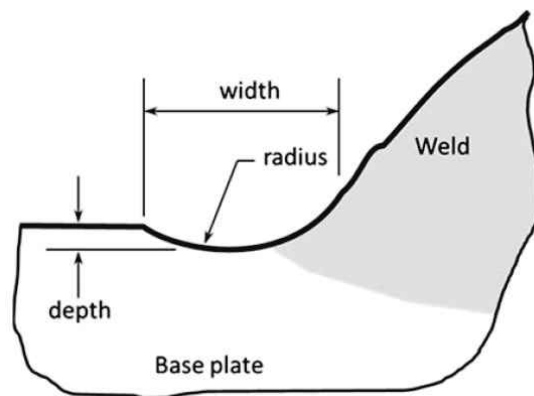


Figure 2-13 Definitions of indentation depth and width [13]

On the other hand, other HFMI process parameters [36], e.g., vibration amplitude and operation frequency, can influence treatment intensity, and thus treatment speed and equipment drivability. Hence, those can change peening quality, resulting in affecting introduced compressive residual stress. Therefore, it is important to understand those influences on induced residual stress state to optimize the time and cost-efficiency of HFMI treatment.

Khurshid et al. [40] investigated the influence of vibration amplitude of HFMI

equipment on introduced residual stress using the flat steel plate specimens made of S355 and S700MC grades steels. Those specimens were treated by HFMI. The vibration amplitude of HFMI indenter was varied in a range of 20 to 60 μm , and introduced compressive residual stress was measured with the aid of the X-ray diffraction method. As a result, the influence of vibration amplitude of HFMI indenter was observed from the measurement result of the specimen made of S700MC grade steel, and the maximum compressive residual stress peak was shifted in deeper region with increasing vibration amplitude. On the other hand, the influence was not observed in the specimen made of S355 grade steel. The most likely reasons could be that the specimen was treated only single pass and electropolishing was performed to measure introduced compressive residual stress in depth direction.

2.3 HFMI simulation

With a steady development of a computational performance, 3D simulation that needs much simulation cost and time than 2D simulation can be easily carried out using a personal computer. In order to help understanding a mechanism of induced compressive residual stress by HFMI treatment and the effect of HFMI treatment, numerical FE HFMI simulation has been attempted so far, and simulation approach for the HFMI simulation has been developed over the past decades. In this section, the necessary knowledge of HFMI simulation was briefly introduced. HFMI simulation conducted in literature was reviewed and discussed.

HFMI simulation has been commonly performed in several commercial software, such as Abaqus, Ansys, and Dytran, using explicit solver. Among them, HFMI simulation in Abaqus explicit solver was mainly described since HFMI simulations were carried out using Abaqus in subsequent chapters of this thesis.

2.3.1 Simulation approaches

Figure 2-14 shows the schematic diagram of HFMI simulation. In HFMI simulation, a small part of a HFMI indenter was modeled as either elastic- [41-43] or rigid- body [30, 44-49]. The latter was often used for the sake of reducing simulation time. Hence, the HFMI indenter was modeling as a rigid body, see subsequent **Chapters 3** and **4**.

HFMI treatment is a process that a workpiece is impacted using an accelerated HFMI indenter with high frequency. Hence, HFMI treatment process will be instantaneously performed to the workpiece. On the other hand, HFMI simulation simplify this HFMI treatment process numerically. Two types of HFMI simulations have

been often used in literature: Displacement-Controlled (DC) and Force-Controlled (FC) simulations. These simulations are performed using “displacement” or “force” and hence require different input parameters. Hereafter, what input parameters DC and FC simulations are necessary and how to take these input parameters were described. The advantage and disadvantages of DC and FC simulations were also described.

DC simulation

DC simulation is that an enforced displacement is input to a HFMI indenter model [40, 41, 44-47, 50-57], see Fig. 2-14a. The magnitude of the enforced displacement is often determined such that the amount of indentation depth of a model to be treated corresponds with an experimentally measured value of an indentation depth after HFMI treatment. Therefore, DC simulation requires information of the indentation depth. It is generally measured at the quantitative quality measurement after HFMI treatment. Since indentation depth is only often used, DC simulation is quite simply and straight forward simulation approach. Although operation frequency is not considerate into DC simulation in many studies, some latest studies incorporates operation frequency into DC simulation using enforced oscillating [48, 49] or step time [58].

FC simulation

FC simulation is that an impact force and velocity of HFMI indenter are input to a HFMI indenter model, see Fig. 2-14b. In addition, a mass is given to the model, and an elastic spring is added to the model's top to control its motion [41-43, 46, 50, 59-61]. Therefore, FC simulation requires information of the impact force and the velocity. The magnitude of the impact force and the velocity is measured during HFMI treatment. Hereafter, an example how to take the impact force and velocity was introduced. Föhrenbach et al. [50] measured the impact force using strain gauges that are mounted on the HFMI indenter and the impact velocity using a high-speed camera whose frame rate is 3000 fps, respectively, as shown in Figs. 2-15 and 2-16. In the case of the study by Föhrenbach et al. [50], PIT weld line 10 was used. They measured that the maximum impact force is 4000 N and the maximum impact velocity is around 5 m/s. Meanwhile, since it takes a lot of work effort to obtain input parameters for FC simulation, in some literature, velocity from 1 to 5 m/s is only input for FC simulation [62-66].

In conclusion, FC simulation uses the impact force and velocity and hence would be more realistic approach than DC simulation in terms of physical phenomena. Nevertheless, a better estimation agreement against experimentally measurement value

was observed in DC simulation rather than FC simulation [42, 50]. Furthermore, simulation time of DC simulation is about three or four times shorter than the FC simulation [50]. One of the most likely reasons why FS simulation needs much simulation time is because the amount of indentation depth per impact is determined by a mass of HFMI indenter model and input impact velocity [43], and therefore several HFMI impacts need to reach a certain indentation depth. Meanwhile, DC simulation requires less input parameter than FC simulation. Hence, DC simulation was employed in this thesis. Note that operation frequency was not considered in this thesis.

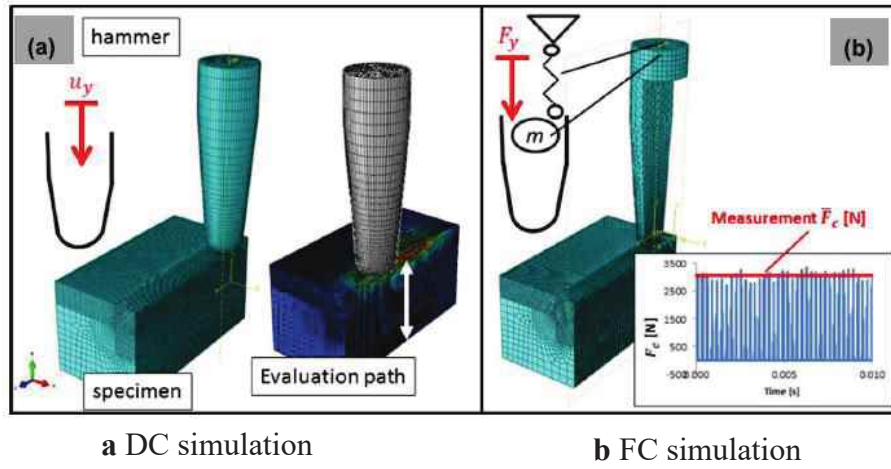


Figure 2-14 Two types of HFMI simulation approaches [50]

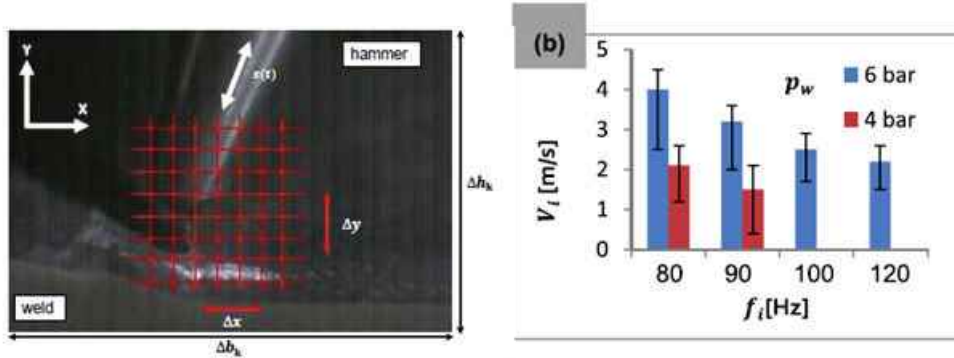


Figure 2-15 Impact velocity recorded using a high-speed camera [50]

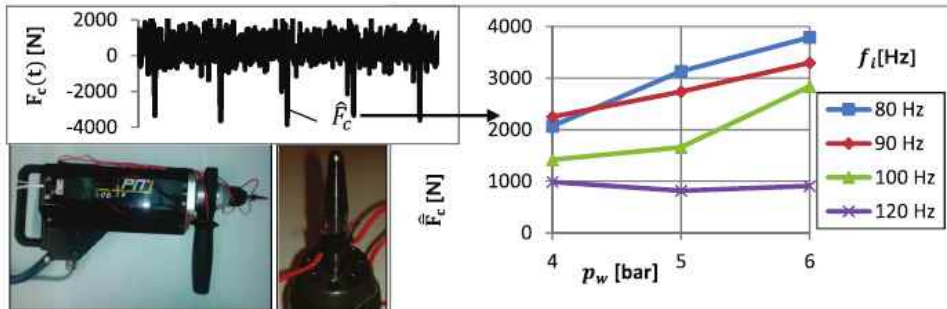


Figure 2-16 Impact force during HFMI treatment measured in [50]

2.3.2 Contact problem

HFMI indenter model will collide and contact a workpiece model during HFMI simulation. Hence, a contact problem is necessary to solve the HFMI simulation. In this section, how to manage the contact problem during the HFMI simulation in Abaqus was described.

Contact formulation

With HFMI simulation, the HFMI indenter and the workpiece models collide and are contacted. A penalty contact algorithm is assigned to the workpiece and the HFMI indenter models to prevent their nodes penetration when their contact. The penalty contact algorithm introduces an additional stiffness into the workpiece model. This additional stiffness is automatically determined and controlled by Abaqus. To work the penalty contact algorithm, master and slave surfaces should be assigned to two model's surfaces that contact themselves during simulation. With the DC HFMI simulation carried out by Khurshid et al. [40], the master and slave surfaces were assigned to the HFMI indenter model and the workpiece model to be treated, respectively. Hence, in the same manner as the study by Khurshid et al. [40], the master and slave surfaces were assigned to the simulation models used in this thesis, see **Chapters 3 and 4**.

Friction behavior

When the HFMI indenter and the workpiece models collide, the coulomb's friction model [67] implemented in Abaqus, described by Eq. (2-1), is used for the friction behavior between those models, where μ is the friction coefficient.

$$F_f = \mu \cdot F_n \quad (\text{Eq. 2-1})$$

In the previous studies of HFMI simulation, the friction coefficient of $\mu = 0.15$ [40-42, 44-47, 50, 55], 0.25 [63-65], 0.3 [48, 49], or 0.5 [65] is assumed. The study on shot peening by Manoucherifar et al. [68] showed that the influence of the friction coefficient between 0.1 to 0.8 is insignificant on the induced compressive residual stress distribution. Hence, in this thesis, the friction coefficient of 0.15 is used.

2.3.3 Material hardening behavior

When a material is loaded beyond an elastic limit, a plastic deformation is left. To describe the plastic deformation, a yield criterion is necessary. Von Mises criteria

described in Eq. (2-2) is normally used for ductile metallic materials. According to the von Mises criteria, plastic deformation onsets that equivalent Mises stress exceeds a material yield strength.

$$F = f(\sigma - \dot{\alpha}) - \sigma_y = 0 \quad (\text{Eq.2-2})$$

where σ_y is the yield stress, and $f(\sigma - \dot{\alpha})$ is the equivalent Mises stress with respect to the back stress $\dot{\alpha}$.

Hardening model describes a plastic material behavior that involves evolution of the yield strength. Figure 2-17 shows the yield surface of different hardening models under loading. The non-linear isotropic hardening model, hereafter called isotropic hardening model, will exhibit a gradual increase in the yield strength as plastic strain increases. The isotropic hardening model is denoted in Eq. (2-3).

$$\sigma_y = \sigma_{y,0} + Q_{\infty}(1 - e^{-b\bar{\epsilon}^p}) \quad (\text{Eq.2-3})$$

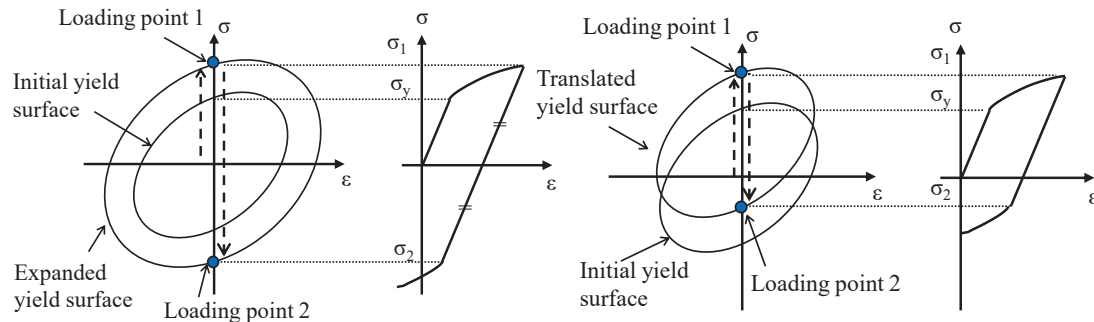
where $\sigma_{y,0}$ is the yield stress at zero plastic strain, Q_{∞} is the maximum increase in the size of the yield surface due to hardening at saturation, b is related to the speed for the saturation. $\bar{\epsilon}^p$ is the equivalent plastic strain and the term is able to consider strain rate dependency. The non-linear kinematic hardening model, hereafter called kinematic hardening model, will exhibit the transition of the yield surface in stress space through the back stress α as described in Eq. (2-4).

$$\dot{\alpha} = \frac{C_k}{\sigma_y}(\sigma - \alpha)\bar{\epsilon}^{pl} - \gamma\alpha\bar{\epsilon}^{pl} \quad (\text{Eq. 2-4})$$

where C_k is the initial kinematic hardening component and γ determines the rate at which the kinematic hardening component decreases with increasing plastic deformation. This kinematic hardening model can be used considering the isotropic hardening model, resulting in combined hardening model known as the Chaboche model [69]. The Chaboche model implemented in Abaqus [70] can represent complex material behaviors below.

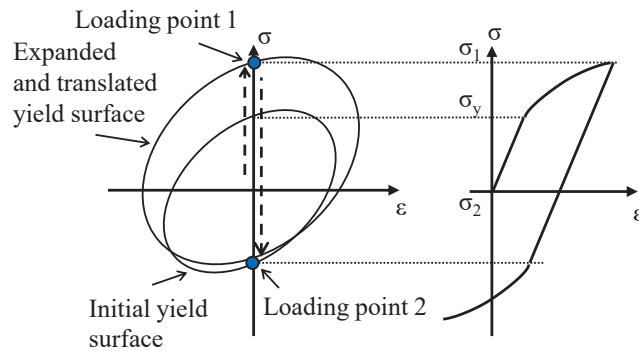
- Bauschinger effect, which reduces yield stress on reversal load after plastic deformation by kinematic hardening model (see Figs. 2-17b and 2-17c)
- Cyclic hardening with plastic shakedown, which increases or reduces yield stress due to plastic strain accumulation by isotropic hardening model. (see Figs. 2-17a and 2-18a)

- Ratchetting or creep, which cause a progressive increase of strain until stabilization value as the number of cycles increases. (see Fig. 2-18b)
- Relaxation of mean stress, which is phenomena that the mean stress tends to zero as the number of cycles increases when an unsymmetric stress is loaded. (see Fig. 2-18c)



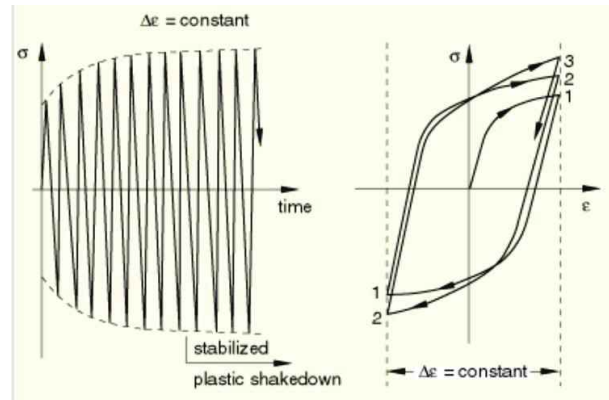
a Isotropic hardening

b Kinematic hardening

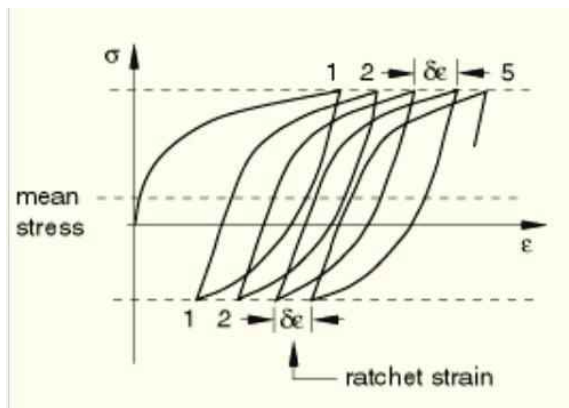


c Combined isotropic-kinematic hardening model

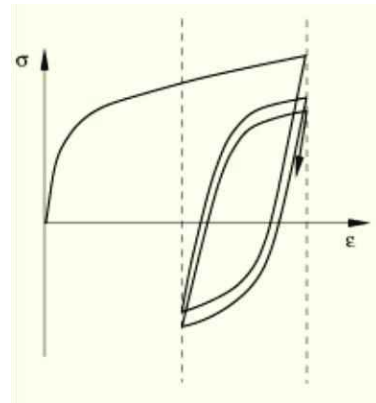
Figure 2-17 Yield surface of different hardening models under loading



a Cyclic hardening with plastic shakedown



b Ratchetting or creep



c Relaxation of mean stress

Figure 2-18 Complex material behavior expressed by the Chaboche model [69]

In order to take stress-strain response of an isotropic hardening model, tensile test using a small specimen is commonly performed under different strain rates. Meanwhile, kinematic hardening component and back stress are taken from tension-compression test [e.g., 50]. This tension-compression test is conducted step by step under strain-controlled conditions. Hereafter, an example found in [50] was introduced. The tension-compression test was conducted with a strain amplitude of 3, 5, and 7 % under strain amplitude $R=-1$, then the kinematic hardening component and back stress were taken. After that, a single element model implemented taken kinematic hardening component and back stress was used for calibration, and the calibration result was compared with the experimental test result, as shown left figure in Fig. 2-19. Figure 2-19 also shows material behavior taking into account of isotropic hardening models under different strain rates [50].

When HFMI treats the welds, HFMI treatment will be performed around the

weld seam where is the mechanical weld heterogeneity and Heat Affected Zone (HAZ). The welds and HAZ show different material properties, and hence material hardening behavior of HAZ is different compared to the one of base material, as shown in Fig. 2-20 [59]. On the other hand, the mechanical weld heterogeneity and HAZ in terms of final residual stress state is of a secondary importance since the previous studies [45, 46] have shown the influence of a welding residual stress on the final residual stress state after the HFMI simulation is less than 15 %. Hence, the mechanical weld heterogeneity and HAZ were not considered in the HFMI simulations performed in this thesis.

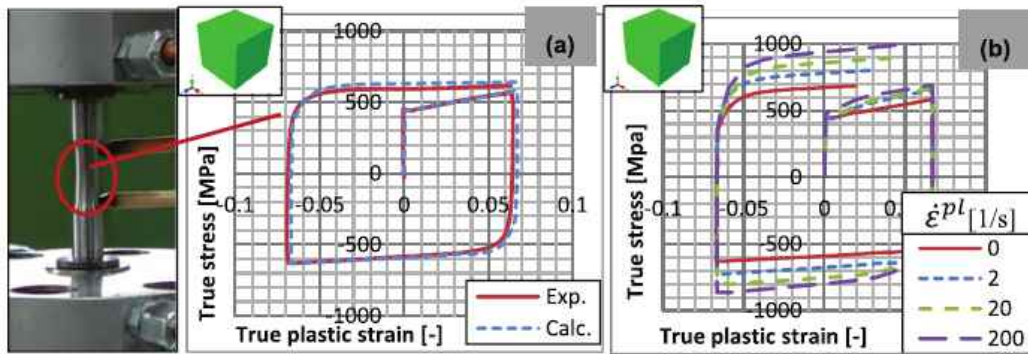


Figure 2-19 Stress/strain response observed in the test result using small specimen and in the simulation using the single element [50]

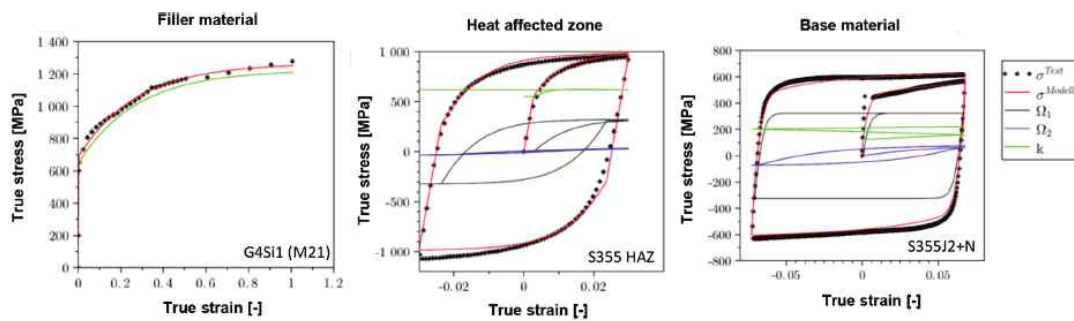


Figure 2-20 Stress/strain response in HAZ, filler material, and base material [59]

2.3.4 Optimum parameters and settings for HFMI simulation

2.3.4.1 Mesh size

Hardenacke et al. [43] investigated the influence of a mesh size on a residual stress state using a flat steel plate model. Figure 2-21 shows the residual stress distributions introduced into the models using different mesh sizes. The results show that the mesh size does not significantly influence the residual stress distributions, especially

for the depths above 1.0 mm. The location of the maximum compressive residual stress is also independent on the mesh size, although the absolute value of introduced compressive residual stress is small when the coarse mesh was used. A major influence of using different mesh size can be seen at the treated surface. Compressive residual stresses of about -100 MPa are generated when the mesh sizes of more than 0.2 mm are used, whereas compressive residual stresses of about -150 MPa are generated when the mesh sizes of less than 0.125 mm are used. The magnitude of induced compressive residual stresses by the mesh sizes of 0.125 and 0.10 mm seems to be almost the same. Hence, it is found that the mesh size of 0.125 mm can capture compressive residual stress at the treated surface enough. Meanwhile, Lennart et al. [56] recommended that the minimum mesh size is less than 1/10 times the HFMI indenter's radius. In this case, the minimum mesh size depends on the indenter's radius. When it is more than 1.5 mm, the recommended minimum mesh size becomes more than 0.15 mm. In this thesis, the HFMI indenter's radii were 3.0 and 1.5 mm, respectively. Thus, the minimum element size of 0.125 mm is used in this thesis.

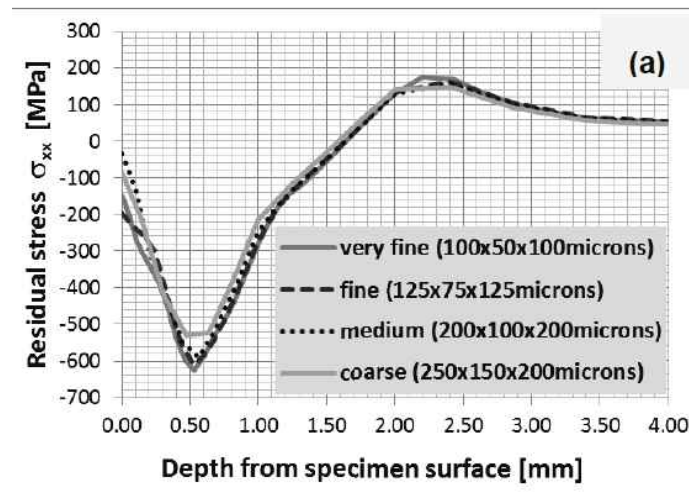


Figure 2-21 Residual stress distributions in depth on different mesh sizes [43]

2.3.4.2 Feed rate and the number of hits

When HFMI simulation is performed to a workpiece model, HFMI treatment conditions, such as the travel speed and the number of hits, are needed. For example, real HFMI treatment conditions are assumed simply in line with the IIW recommendation [13]: operation frequency of 90 Hz and the travel speed of 2 mm/s. Under this treatment condition, HFMI treatment will be performed 2 mm length within 2 sec, and hence 45 HFMI hits would approximately be done each 1 mm length. Considering HFMI simulation, enormous simulation time would be required when 45 HFMI hits are

simulated per 1 mm length. Hence, HFMI simulation employing even this simply assumed real HFMI treatment conditions would be hard to be reproduced. Therefore, HFMI simulation is often performed using simplified HFMI treatment conditions for the sake of reducing simulation time. In HFMI simulation, the travel speed is replaced as the feed rate that is either 0.2 or 0.4 mm/hits. Föhrenbach et al. [50] and Ernould et al. [42] used the feed rate of 0.2 mm/hit in FC simulation. Simunek et al. [71] used the feed rate of 0.4 mm/hit in DC simulation and found that the DC simulation under 0.4 mm/hit shows a good compromise between simulation time and achieved the geometric feature. They also demonstrated that good estimation accuracy compared with the experimental results. Hardenacke et al. [43] compared the influence of the feed rate of 0.2 and 0.4 mm/hits on the residual stress state in depth direction and concluded that the influence has no significance. Thus, the feed rate of 0.4 mm/hit seems to be a good compromise between numerical calculation efforts and solution accuracy. Accordingly, the feed rate of 0.4 mm/hit was used in DC simulation in this thesis. On the other hand, the investigation regarding the number of hits is quite a few.

2.3.4.3 Material hardening model

Choice of material hardening model is an essential matter in HFMI simulation. Different material hardening models influence produced residual stress state by the HFMI simulation. Hence, suitable material hardening model should be used in line with the aim of HFMI simulation. Several researchers investigated the influence of the material hardening model on the residual stress state using flat steel plate model [40, 41, 56, 63-65] or welded joint model [44-49, 55, 60], assuming S355 or similar grades steels. In those investigations, isotropic hardening model [40, 41, 56], or combined isotropic-kinematic hardening model based on the Chaboche model [40, 41, 44-46, 48, 49 54-56] or the Jonson-cook [47, 63-65] model were used.

Föhrenbach [51] carried out experimental and numerical investigations using a flat steel plate in order to describe the condition in the surface layer and revealed that the choice of the material hardening model considerably influenced the simulated residual stress. They recommended that the DC simulation with the combined isotropic-kinematic with strain rate dependent hardening model can estimate well experimental measured value.

Khurshid et al. [40] carried out DC simulation on a flat steel plate model to investigate the influence of using different material hardening models on the residual stress state. Different material hardening models were isotropic, isotropic with strain rate dependence, combined and combined with strain rate dependent model. They compared

the simulation results with the experimentally measured values taken from S355, S700MC, and S960 grades steels of flat steel plates. From the results, they indicated that residual stress state near the treated surface can be estimated qualitatively well using isotropic or isotropic hardening model with strain rate dependency models. They also indicated that the accuracy of residual stress estimation in depth was higher when the combined hardening or the combined hardening with strain rate dependency models were used to the HFMI simulation.

Several researchers have investigated the optimal parameters and settings for the HFMI simulations and have revealed the influence of the choice of the material hardening model on the residual stress state. As a result, HFMI simulation is being utilized as a reliable tool for residual stress estimation. Under this circumstance, a numerical investigation on HFMI treatment processes, such as vibration amplitude and operation frequency, would help better understand of those influences on the residual stress state since microscopic and/or detailed phenomena hardly observed experimentally could be investigated. However, there is a lack of numerical studies on the HFMI treatment processes.

2.4 Effect of HFMI treatment on life extension of pre-fatigued welded joints

Many steel bridges in Europe and Japan were constructed several decades ago [72, 73], with a current need for continuous maintenance where the major challenge in old steel bridges is fatigue cracks. Utilization of HFMI treatment for repairing and life extension of pre-fatigue welded joints has been gained in interest as a robust method [74]. In this section, investigations regarding HFMI treatment on pre-fatigued welds were reviewed. Meanwhile, ICR and PPP treatment for repairing and life extension of pre-fatigued welds has been gained in interest in Japan. Those investigations were also reviewed.

2.4.1 Hammer and needle peening

ICR treatment was developed to close surface crack opening in pre-fatigued welds and effectively extend the fatigue life of the welds, as explained in **Section 2.2.1**. When the surface crack is closed and does not open due to an applied load, the surface crack can be considered as an internal crack. Its crack length becomes half compared with the surface crack. As a result, stress intensity factor at the crack tip can be reduced and fatigue life can be extended [21]. Yamada et al. [21] carried out plate bending fatigue test using a plate bending loading system in order to investigate the effect of the ICR treatment

on life extension of pre-fatigued welds and demonstrated that the ICR treatment could extend fatigue life remarkably even when the welds are already cracked and the cracks propagated to the base plate.

To enhance fatigue strength of the weld toe, peening treatment is often performed. Peened welds would have higher fatigue strength than one of weld root. Consequently, fatigue cracks could initiate from the weld root and appear on the weld bead. Therefore, it is necessary to investigate whether ICR treatment could extent fatigue life of such fatigued welds. Akiyama and Kinoshita [75] investigated the effect of ICR treatment on life extension of the welds including cracks on their weld bead. They demonstrated that the fatigue life of the welds including cracks on their weld bead could be extended as similar fatigue strength of AW state using the ICR treatment. They also demonstrated that the effect of ICR treatment could be higher when the shape of the weld bead becomes flattened due to repetition ICR treatment.

On the other hand, the effect of life extension of pre-fatigued welds have also been investigated using PPP treatment nowadays. Fueki et al. [76] investigated the effect of PPP treatment on the life extension to the welds with an artificial semi-circular slit depths of 1.0 and 1.5 mm. They demonstrated that the artificial semi-circular slit depth less than 1.0 mm could be rendered harmless by the PPP treatment. The author investigated the effect of PPP treatment to pre-fatigued out-of-plane gusset welds that have relatively larger cracks than ones by Fueki et al. [76]. The author demonstrated that the fatigue life of the pre-fatigued welds could be extended to a similar fatigue life of AW state by repetition of the PPP treatment. When PPP treatment is adequately performed under quality control, fatigue life of pre-fatigue welds can be extended more than the

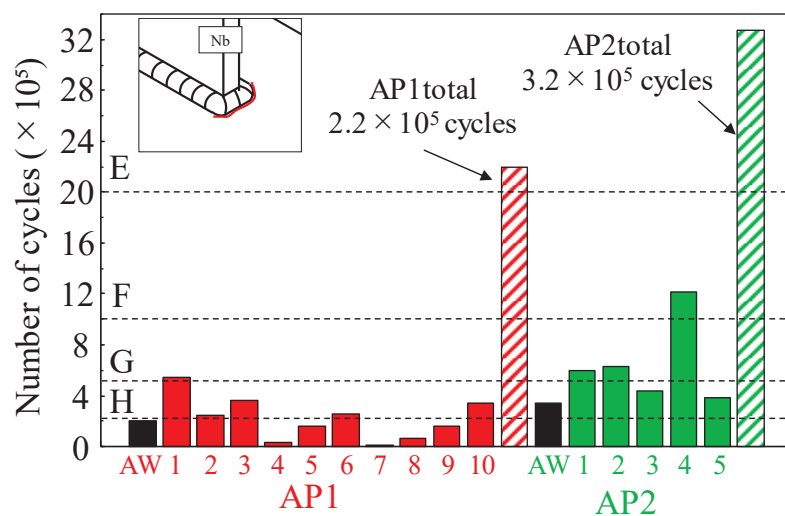


Figure 2-22 The effect of PPP treatment on pre-fatigued welded joints in the author's previous study

fatigue strength of AW state, as shown in Fig. 2-22.

From those investigations, it is found that ICR and PPP treatment can be used in the purpose of life extension even when the welds are already cracked.

2.4.2 High frequency mechanical impact

Several researchers have investigated the utilization of HFMI techniques for pre-fatigued welds and demonstrated those effect on life extension. Kudryavtsev et al. [77] investigated the effect of UP for the purpose of rehabilitation and repair of pre-fatigued welds of fatigue-damaged steel structures and demonstrated that UP can extend the fatigue life of the pre-fatigued welds as the same fatigue life as UP treated welds without fatigue. Also, they compared the effect of different restraining and repairing techniques for fatigue cracks, such as drilling with and without bolting, overloading, local explosive treatment, local heat treatment and welding with and without UP treatment. They revealed that the effect of welding with UP on fatigue life extension was highest, yet even when UP was only performed, the effect was significant compared to other restraining and repairing techniques.

Leitner et al. [78] used HFMI treatment for rehabilitation of pre-fatigued longitudinal welds with a crack depth of 0.5 mm and demonstrated that the effect of HFMI treatment depends on applied nominal stress range and it is remarkable especially for a run-out level of longitudinal welds.

Lefebvre et al. [9] evaluated the effect of HFMI treatment on retrofitting of pre-fatigued butt welds with crack depths in a range of 0.5 to 3.0 mm and indicated that the effect of HFMI treatment depends on the crack depth and could be used for retrofitting of the pre-fatigued welds with equal or inferior to the millimeter crack depth.

Meanwhile, Branco et al. [79] introduced the concept of the gain factor in order to quantify the effect of life extension by hammer peening on pre-fatigued welds. The gain factor, $g = N_r/N_e$, is defined as the ratio of the fatigue life of the repaired weld, N_r , to the fatigue life of the newly treated weld, N_e . This evaluation using the gain factor clearly demonstrated that the effect depends on the crack depth [79]. The validity of this evaluation was verified in the study by Leitner et al. [78]. Hedegård et al. [80] used the gain factor to quantify the effect of HFMI treatment to pre-fatigued rat-hole detailed specimen and demonstrated that the effect is superior when the crack depth is shallower than 1.5 mm. Recently, Karawi et al. [81] collected more than 250 test data from literature to analyze the effect of HFMI treatment on different pre-fatigued welded details, such as butt welds, longitudinal- and transverse- weld attachments, and cover plate welded details, based on the gain factor. The study by Karawi et al. [81] demonstrated that HFMI

treatment could successfully be used for extending the fatigue life even when those welded details contain fatigue cracks that are less than 2.25 mm in depth.

From those investigations, HFMI treatment could effectively extend the fatigue life of pre-fatigued welds of fatigue-damaged welded structures. However, it can be expected that the closed fatigue crack is opened depending on the magnitude of applied stress and result in continuing crack propagation due to service loads. Accordingly, understanding the crack opening-closing behavior, of HFMI treated pre-fatigued welds, due to service loads is necessary, which will increase in the reliability of HFMI treatment as a robust life extension technique.

2.5 Linear elastic fracture mechanics

Fatigue life of an object or a material will be evaluated using several methods, such as S-N curves and fatigue crack propagation. The evaluation based on the S-N curve has the inherent disadvantage which cannot evaluate how cracks propagate and final crack state when the object and/or the material failure. An alternate method based on fracture mechanics concepts have been developed. Linear Elastic Fracture Mechanics (LEFM), as the basic theory of fracture mechanics, is a state-of-the-art and a beneficial approach to evaluate how cracks propagate and final crack state. Usually, the material, such as steel, is considerate brittle when it breaks at low elongations, not exceeding a few percentage points. For such material, LEFM is widely used for the fatigue life evaluation with respect to its simplicity because it works well since small deformations around the crack tip led to fracture. LEFM assumes that the materials are an isotropic and linear elastic, and hence a stress and a strain singularity at the crack tip is yield, which cannot exist for actual materials. Hence, an assumption must take place in order to limit the stress and the strain at finite values for LEFM to be valid. This assumption is that the plastic and the damage area at the crack tip must remain small enough with respect to the size of the specimen or of the structure. This is so-called the small scale yielding condition. This small scale yielding condition states that the ligament size of the specimen or the structure must be large compared to the plastic zone size. The requirement of the small scale yielding condition for LEFM to be valid is specified by, e.g., ASTM [82], as Eqs. (2-5) and (2-6) below.

$$l_{min} \geq 2.5 \left(\frac{K_{IC}}{\sigma_Y} \right)^2 \quad (\text{Eq. 2-5})$$

$$l_{min} = \min(\alpha, B, W - \alpha) \quad (\text{Eq. 2-6})$$

where, K_{IC} is a fracture toughness that denotes stress intensity factor (SIF) for crack Mode-I, which was developed by Irwin [83], a is a crack length, B and W are a thickness and a width of a structure.

2.6.1 Stress intensity factor

The SIF, which is denoted “ K ” as shown in Eq. 2-5, is a useful method in LEFM. It predicts the stress intensity near the crack tip of a crack caused by a remote load or a residual stress. This concept of SIF was developed by Irwin [83]. Before the description of SIF around the crack tip, it is important to distinguish primary crack opening mode of stressing. Due to different loading conditions, the crack front is opened with three opening modes and their combinations. Three primary crack opening modes are shown in Fig. 2-23. Mode-I (K_I) is the most widely encountered in practice, which is due to tensile stresses. It corresponds to normal separation of the crack front, where the in-plane stresses and strains are symmetric with respect to the X axis. Mode-II (K_{II}) is the sliding or in-plane shearing mode, where the stresses are anti-symmetrical with respect to the X axis. Mode-III (K_{III}) is the tearing or anti-plane shearing mode, where the out-of-plane stresses and strains are anti-symmetrical with respect to the X axis. Those three primary crack opening modes are expressed as K_I , K_{II} , and K_{III} , respectively.

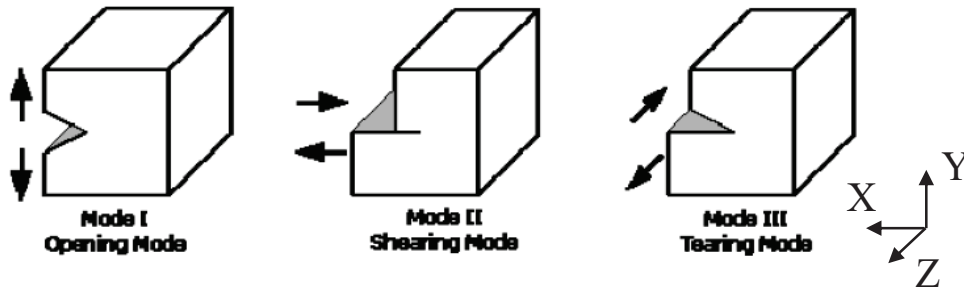


Figure 2-23 Three different crack opening modes found in [84]

Figure 2-24 shows schematically image of an element near the crack tip of a crack in an elastic material with in-plane stresses on this element. Ideal planar crack problems are considered, in which the stresses and strains near the crack tip can be expressed in terms of the in-plane coordinates the X and Y axis only. For the sake of simplicity, each stress component under Mode-I, K_I , is only introduced. The entire stress distribution around the crack tip can be computed using K_I and the coordinate around the crack tip, as denoted Eqs. (2-7), (2-8), (2-9), and (2-10).

$$\sigma_{xx} = \frac{K_I}{\sqrt{2\pi r}} \cos\left(\frac{\theta}{2}\right) \left[1 - \sin\left(\frac{\theta}{2}\right) \sin\left(\frac{3\theta}{2}\right)\right] \quad (\text{Eq.2-7})$$

$$\sigma_{yy} = \frac{K_I}{\sqrt{2\pi r}} \cos\left(\frac{\theta}{2}\right) \left[1 + \sin\left(\frac{\theta}{2}\right) \sin\left(\frac{3\theta}{2}\right)\right] \quad (\text{Eq.2-8})$$

$$\tau_{xy} = \frac{K_I}{\sqrt{2\pi r}} \cos\left(\frac{\theta}{2}\right) \sin\left(\frac{\theta}{2}\right) \cos\left(\frac{3\theta}{2}\right) \quad (\text{Eq.2-9})$$

$$\sigma_{zz} = \begin{cases} 0 & \text{Plane stress} \\ \nu(\sigma_{xx} + \sigma_{yy}) & \text{Plane strain} \end{cases} \quad (\text{Eq.2-10})$$

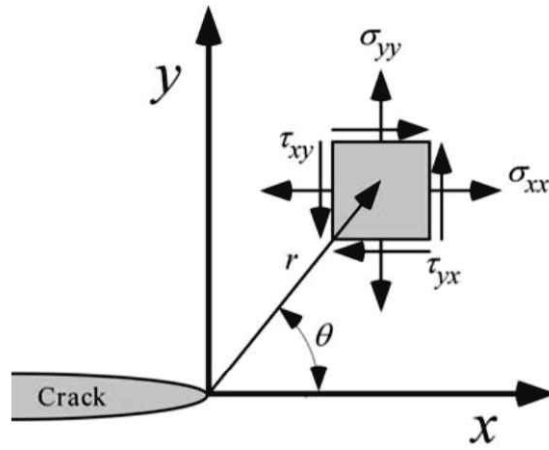


Figure 2-24 Stresses near the tip of a crack in an elastic material [85]

2.5.2 The principle of superposition

LEFM is the linearity prevails and hence superposition is possible. This superposition is another useful method in LEFM. This is well known as the principle of superposition [e.g.,86]. The principle of superposition is able to add and decompose the SIF solutions into simple loads and geometry configurations in such a way that those sum becomes more complex loads and geometry conditions. Figure 2-25 shows an example of using the principle of superposition, where a crack in an element stresses uniformly from both remote sides. This crack is also locally stressed in the opposite direction as the uniform stresses. The uniform stresses exactly balance the local stresses. In this case, using the principle of superposition, the state of structural element B can be decomposed into the ones of structural elements C and D, see Fig. 2-25. The expression can be written using, e.g., Mode-I, as following Eq. (2-11).

$$K_I^A = K_I^B = K_I^C + K_I^D \quad (\text{Eq.2-11})$$

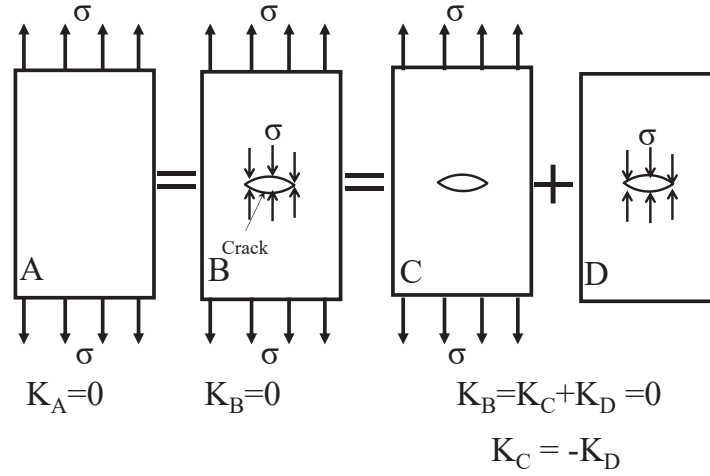


Figure 2-25 The principle of superposition

2.5.3 Stage of crack propagation

It is generally accepted that crack propagation under cyclic loading is divided into three main stages: crack initiation, crack propagation, and final failure. Figure 2-26 shows the three stages of crack propagation. The first stage presents a threshold, ΔK_{th} . Below the threshold value, there is no crack propagation. The second stage shows a relatively steady state, where a crack propagation rate increases steadily with increasing the number of cyclic loadings. This steady crack propagation is always described by the Paris and Erdogan law [87]. There is a relationship between SIF at the crack tip that is characterized by the applied stress and the crack propagation length per load cycle, which is experimentally proven, as written in Eq. 2-12.

$$\frac{da}{dN} = C(\Delta K)^m \quad (\text{Eq.2-12})$$

$$\Delta K = K_{max} - K_{min} \quad (\text{Eq.2-13})$$

where, a is the crack propagation length, and da/dN is the crack propagation rate per the number of cycles N . C and m are the material coefficients. ΔK is a stress intensity factor range as shown in Eq. 2-13. The final stage represents an unstable situation, where the unstable fracture occurs when the crack propagation rate reaches the fracture toughness, K_C . In this final stage, a structure fails rapidly within a small number of cycles.

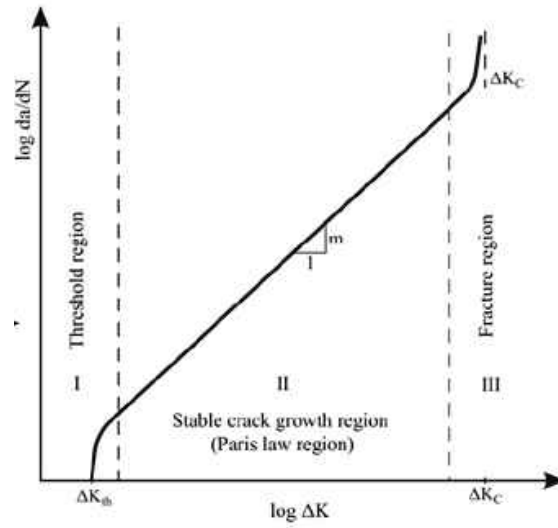


Figure 2-26 Schematic of the three main stages of crack propagation found in [88]

2.5.4 Fatigue life estimation of pre-fatigued welds treated by HFMI using LEFM

Because weld defects due to spatter or undercut [84] are introduced in the weld toes in the steel structures. Fatigue cracks may initiate from those defects in the weld toes, and they propagate under cyclic loading. The fatigue life of the welded joints is often divided in a crack initiation stage and a crack propagation stage.

$$N_t = N_i + N_p \quad (\text{Eq.2-14})$$

Where N_t , N_i and N_p are the total fatigue life, crack initiation and crack propagation life, respectively. Although LEFM is not able to be used for crack initiation stage, it works well for the fatigue life estimation of the welds of the steel structure because those have defects in their welds. Those defects can be assumed as short cracks. Several studies [84, 88-92] have applied LEFM for the fatigue life estimation of the welded joints with defects or small cracks in their weld toe and have demonstrated that their fatigue lives can quantitatively be estimated even in comparison with the experimental test results.

On the other hand, fatigue life estimation of pre-fatigued welds treated by HFMI has been gathering a lot of interest nowadays. Yekta et al. [39] carried out 2D CPA based on LEFM in order to investigate the fatigue life of HFMI treated welds with HFMI induced defects. They demonstrated that the effect of fatigue strength improvement by HFMI decreases with increasing the defect depth in HFMI treated welds and can completely be vanished if the defect is sufficiently large. Karawi et al. [93] evaluated the effect of cracks in HFMI treated welds using 2D CPA based on LEFM and demonstrated

the effect quantitatively well. In those investigations, simplified analytical compressive residual stress distributions estimated from experimentally measured values are incorporated into those 2D CPA [39, 93]. Hence, although the investigations were conducted on 2D CPA based on LEFM, the fatigue life of pre-fatigued welds treated by HFMI could be estimated well considering compressive residual stress distribution introduced into the HFMI treated welds. On the other hand, the presence of cracks in pre-fatigued welds could affect compressive residual stress state by HFMI [93, 94]. Furthermore, the shape of the cracks in HFMI treated welds would be varied depending on the magnitude of applied stress and affect whether the cracks in HFMI treated welds propagate. Accordingly, investigation of defect tolerance of HFMI treated welds in bridge application on life extension is necessary to use HFMI techniques for repair and life extension of pre-fatigued welds of fatigue-damaged steel structures.

2.6 Conclusions

The objective of this chapter is to determine the subjects that are addressed in subsequent chapters of this thesis through review of literature including authors' previous study. Conclusions obtained from the review and the subjects of the subsequent chapters can be summarized as follows.

1. Quality controls, such as travel speed and the number of treatment passes, and finish quality measurement are essential to hammer and needle peening and HFMI treatment to ensure compressive residual stresses and to improve the fatigue strength of the welded joints. However, induced residual stress can be influenced by HFMI treatment processes, e.g., vibration amplitude and operation frequency. Therefore, it is important to understand those influences on induced residual stress to optimize the time and cost-efficiency of HFMI treatment.
2. Two types of HFMI simulation, DC and FC simulation, have been often performed. DC simulation that uses enforced displacement to carry out HFMI simulation would be more reasonable than FC simulation in terms of less time-consuming and accurate simulation results. Although optimum parameter and settings for HFMI simulation has been investigated in literature, there is a lack of numerical studies on the HFMI treatment processes.
3. Hammer and needle peening and HFMI effectively extend the fatigue life of the fatigue-damaged welded structure. However, it can be expected that the closed fatigue crack is opened depending on the magnitude of applied stress and result in continuing crack propagation due to service loads. Accordingly, understanding the

crack opening-closing behavior of HFMI treated pre-fatigued welds, due to service loads, is necessary which will increase in the reliability of HFMI treatment as a robust life extension technique.

4. Fatigue life of HFMI treated pre-fatigued welds could be estimated well based on LEFM. However, presence of cracks in pre-fatigued welds could affect compressive residual stress introduced by HFMI. Furthermore, the shape of the cracks in HFMI treated welds would be varied depending on the magnitude of applied stress and affect whether the cracks in HFMI treated welds propagate. Accordingly, investigation of defect tolerance of HFMI treated welds in bridge application on life extension is necessary to use HFMI techniques for repair and life extension of pre-fatigued welds of fatigue-damaged steel bridges.

Chapter 3

Validity of HFMI simulation for residual stress estimation using a flat and bead on steel plates models

3.1 Introduction

The objective of this chapter is to verify the validity of HFMI simulation for residual stress estimation using a flat and bead on steel plates models. This verification was conducted by Displacement-Controlled (DC) HFMI simulation using an isotropic hardening model.

First, the mass scaling method was applied to the HFMI simulation in order to reduce its simulation time, and the influence of the mass scaling method was examined in terms of simulation time, introduced residual stress state, and energy balance during the HFMI simulation. Then, the HFMI simulations using the isotropic hardening model were carried out to the flat steel plate model, where feed rate and the number of hits of the HFMI indenter were varied in order to investigate the influence of difference HFMI treatment processes, such as under- and over-treatment, on residual stress state. In addition, after the HFMI simulation, the influence of electropolishing on residual stress state was examined.

Then, the HFMI simulation using the isotropic hardening model was carried out on the bead on steel plate model in order to investigate its applicability for residual stress estimation. Estimated compressive residual stresses by the HFMI simulations were compared with the experimental measured values.

All HFMI simulations were conducted using commercial software Abaqus 6.21 [70], with dynamic explicit solver.

3.2 HFMI simulation to flat steel plate model

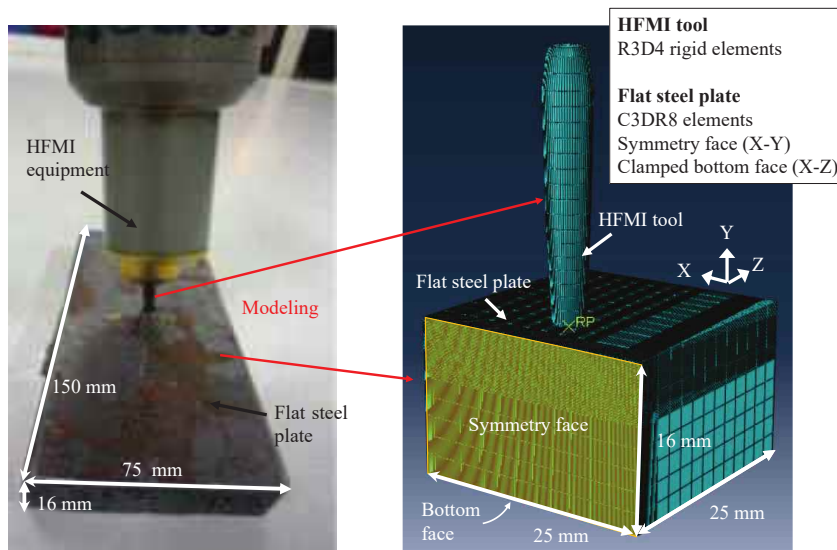
3.2.1 FE modeling of flat steel plate and HFMI tool

In order to investigate the influence of HFMI treatment processes, such as under- and over- treatment on residual stress state, HFMI simulation model was performed. For the HFMI simulation model, a flat steel plate specimen made of S355 grade steel and HFMI tool studied and modeled by Khurshid et al. [40] were used. Figure 3-1 shows the flat steel plate model used in the HFMI simulation. A small section of the flat steel plate specimen shown in Fig.3-1a was modeled to reduce simulation time. The dimension of the flat steel plate model was $25 \times 25 \times 16$ (width \times depth \times height) in mm. Boundary conditions were given to the symmetry face (the X-Y plane, $u_z=0$) and the bottom face (the X-Z plane, $u_x=u_y=u_z=0$). The mesh of the model consisted of 8-node continuum elements with reduced integration (C3D8R). When a reduced integration element is used, zero-strain deformation like “hourglassing” could occur because the reduced integration element has only one integration point. Therefore, an hourglass-control was introduced

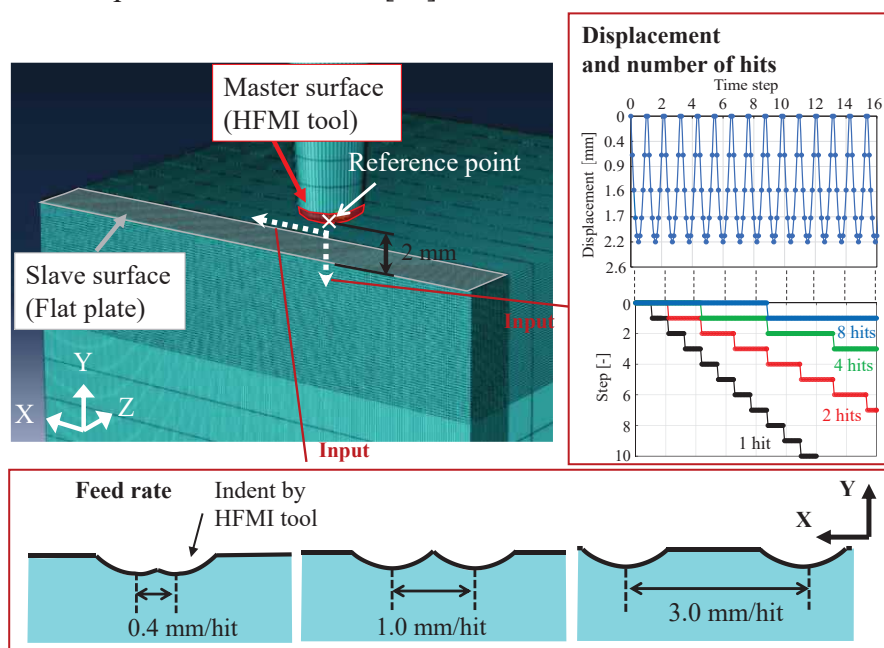
into the flat steel plate model in order to avoid such zero-strain deformation. The minimum mesh size of 0.125 mm recommended by Föhrenbach et al. [50] was assigned to the region where HFMI indenter model is hit, while the rest of the flat steel plate model was gradually larger mesh size.

Figure 3-1b shows the HFMI tool model. The dimension of the HFMI tool model was the size of 3×25 (tip radius \times length) in mm. A rigid body was assigned to the HFMI tool model, aimed to reduce simulation time, and mass was not given to the model. The HFMI tool model was meshed by 4-node tetrahedral elements (R3D4). A contact pair was defined between the HFMI tool model (master surface) and the flat steel plate model (slave surface), as shown in Fig. 3-1c, using the penalty contact algorithm with a friction coefficient of $\mu=0.15$. In order to maintain a high-quality mesh throughout HFMI simulation, Arbitrary Lagrangian-Eulerian (ALE) adaptive meshing was assigned on the slave surface.

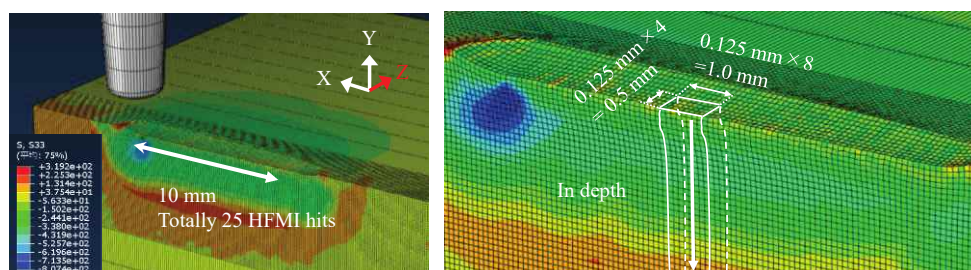
DC HFMI simulation was carried out. In this DC HFMI simulation, an enforced displacement was applied to the HFMI tool model, and hence, physical phenomenon, such as acceleration, velocity, and frequency, were not considered. The HFMI tool was set 2.0 mm above the flat steel plate model, see Fig. 3-1c. To perform the DC HFMI simulation on the flat steel plate model, the HFMI tool model was moved toward the X-direction and the Y-direction based on the reference point put on the bottom of the HFMI tool model, as shown in Fig. 3-1c. The HFMI treatment simulation was carried out 10 mm along the X-direction by a feed rate of 0.4 mm/hit, i.e., totally 25 HFMI hits, see Fig. 3-1d. This feed rate is the calibrated treatment condition that shows a good compromise between simulation time and achieved geometric feature [44]. Total enforced displacement of 2.2 mm ($2.0 + 0.2$ mm) toward the Y-direction was given. Enforced displacement of 0.2 mm was determined considering springback effect after HFMI treatment simulation. When the enforced displacement of 0.2 mm is given, an indentation depth will be about 0.14 mm, which corresponds with the experimentally measured mean value in the study by Khurshid et al. [40].



a Flat steel plate and HFMI tool [40] **b** The flat steel plate model



c Detailed setting of HFMI simulation



d Flat steel plate model after HFMI simulation

Figure 3-1 The flat steel plate model used in FE HFMI simulation

3.2.2 Material hardening model

Material hardening model influences residual stress estimation. There are several hardening models implemented in Abaqus. So far, many researchers have carried out HFMI simulations using isotropic, kinematic, and combined isotropic and kinematic hardening models. The study by Khurshid et al. [40] demonstrated that HFMI simulation using an isotropic hardening model could give reasonable estimation results up to 0.8 mm in depth. The model's surface will receive severe work hardening during HFMI treatment simulation. Hence, residual stress on the model's surface would be significantly influenced when HFMI treatment process is varied. Thus, the isotropic hardening model was employed in this investigation.

Table 3-1 shows mechanical properties and chemical compositions of S355 grade steel found in [95]. Figure 3-2 shows the isotropic hardening properties used in the study [40]. In practice, a workpiece's surface made of steel will receive a higher strain amplitude during HFMI treatment, involving plastic deformation under a higher strain rate and causing strain hardening. Strain hardening involves different isotropic hardening properties, depending on the strain rate, as shown in Fig. 3-2. On the other hand, Lennart et al. [56] showed from the results of the HFMI simulation on the flat steel plate model consisting of S355 grade steel that the HFMI simulation leads to a reasonable agreement with the experimental results even when strain rate dependency due to higher strain rate is not considered. Thus, the isotropic hardening property under a strain rate of 0.0001 was employed. An elastic modulus $E=2.1 \times 10^6$ MPa and Poisson's ratio $\nu=0.3$ were used.

Table 3-1 Mechanical properties and chemical composition found in [95]

Type of steel	Yield strength (Min.)	Tensile strength	Elongation	Chemical composition [%]				
				C (Max.)	Si (Max.)	Mn (Max.)	P (Max.)	S (Max.)
	[MPa]		[%]	×100			×1000	
S355	355	470-630	21	18	50	160	20	10

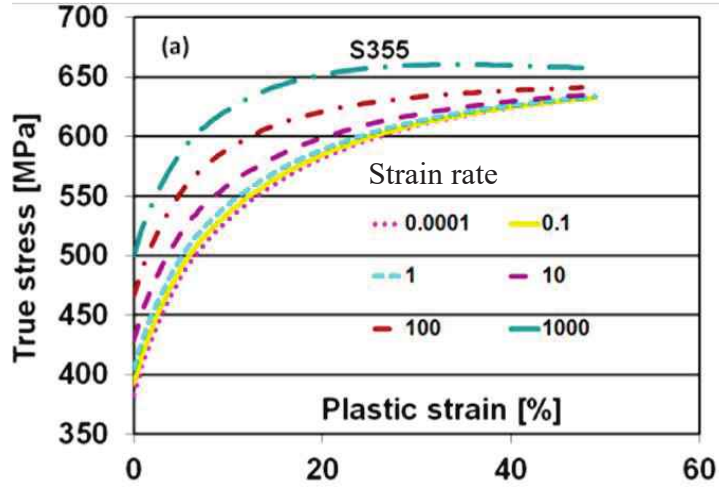


Figure 3-2 Isotropic hardening properties used in [40]

3.2.3 Investigation on reduction of simulation time

When a simulation is solved with Abaqus explicit solver [70], an explicit central-difference time integration rule is used to integrate the resulting equations of motion explicitly. This explicit central-difference time integration rule is conditionally stable and does not need the use of iterative calculation. The rule requires that for each time increment, Δt , the current solution be expressed as:

$$\dot{u}_{(i+\frac{1}{2})}^N = \dot{u}_{(i-\frac{1}{2})}^N + \frac{\Delta t_{(i+1)} + \Delta t_{(i)}}{2} \ddot{u}_{(i)}^N \quad (\text{Eq.3-1})$$

$$u_{(i+1)}^N = u_{(i)}^N + \Delta t_{(i+1)} \cdot \dot{u}_{(i+\frac{1}{2})}^N \quad (\text{Eq.3-2})$$

where, u^N is degree of freedom (a displacement or rotation component), the subscript i indicates the increment number in an explicit dynamic step and Δt is time increment. The current solution to the current time increment depends only on the solution of previous time increment, and hence, the costly iterations to decide to the unknown

solution at the current time increment can be avoided. The drawback with explicit methods is the stability, which is controlled by the smallest transit time of a dilatational wave across every element in mesh. The stability is controlled by the courant condition shown in Eq. (3-3).

$$\Delta t_{ST} = L_{min} \cdot \sqrt{\frac{\rho}{E}} \quad (\text{Eq.3-3})$$

$$\Delta t \leq \Delta t_{ST} \quad (\text{Eq.3-4})$$

where, Δt_{ST} is stable time increment, L_{min} is minimum element length, ρ is a material density, and E is young's modulus. In order to maintain simulation stability, each time increment is automatically controlled so that the time increment is not beyond the stable time increment, see Eq.3-4. When finer mesh is used in simulation model, the stable time increment becomes small magnitude, and hence time increments to solve the simulation increase. Consequently, the simulation time increases. Therefore, the model's material density is often up-scaled to increase the magnitude of stable time increment and solve the simulation fast. This concept is known as the mass scaling method, and it is widely utilized to shorten the simulation time [61, 96, 97]

The drawback of using the mass scaling method is that inertia force occurs due to up-scaling mass. Consequently, kinetic energy could be increased. Therefore, it is important to examine whether the simulation using the mass scaling method shows proper result. Schubnell et al. [61] utilized the mass scaling method to FC HFMI simulation. However, detailed information, such as up-scaling rate, simulation time and the influence on the residual stress state was not described. Thus, those influences against DC HFMI simulation were investigated. This investigation was carried out using the flat steel plate model shown in Fig. 3-1b. This model was treated by the DC HFMI simulation under the conditions of the feed rate of 0.4 mm/hit, one hit and given enforced displacement of 2.2 mm.

Table 3-2 shows investigation cases on reduction of simulation time. Material density of the flat steel plate model was changed from around 10^2 to 10^5 times on the basis of the steel's material density. In the table, up-scaling rate of the material density, simulation time, and the number of used CPUs are also shown. It is found that the HFMI simulation time is steadily reduced as the material density is increased. In the case of HFMI simulation using the material density of 1.0 kg/mm^3 , the reduction rate of the simulation time reaches 99 %. Even below the material density of 0.1 kg/mm^3 is used, the

reduction rate reaches 95 %. Thus, adopting the mass scaling method to the HFMI simulations can result in reducing simulation time more than 90 % in comparison with the HFMI simulation time without the mass scaling method.

Table 3-2 Investigation cases on reduction of simulation time

Material density [Kg/mm ³]	Up-scaling rate of material density [-]	Simulation time [%]	Number of used CPUs
7.58×10^{-6}	1	100	8
1.0×10^{-3}	137	26	8
1.0×10^{-2}	1274	16	8
1.0×10^{-1}	12,739	5	8
1	127,389	1	8

Figure 3-3 shows residual stress state obtained from the DC HFMI simulations using different material densities. Each stress value was averaged over multiple integration points (see Fig. 3-1d), as recommended in [50]. The domain of the multiple integration points was the same as the collimator spot size used in [40]. From the results, it is found from the transverse residual stresses, that the trends and magnitudes in the treated surface and also in depth direction are in well agreement with themselves, see Fig. 3-3a. On the other hand, in the longitudinal residual stresses, it can be observed that simulated residual stresses are in larger differences near the treated surface. The simulated values are -443 MPa by HFMI simulation using the 1.0 kg/mm^3 , while -620 MPa by the one using the steel's material density, see Fig. 3-3b. When a HFMI treated boxing weld is considered, residual stresses perpendicular to the indentation by HFMI, i.e., transverse residual stress, is more important than longitudinal one because fatigue cracks will initiate parallel to the weld. Hence, the crack initiation could be suppressed by the transverse residual stress. Thus, using the mass scaling method must be carefully considered when longitudinal residual stress is important.

To examine whether the simulation can be well controlled, two criterions in relation to energy balance were checked during the HFMI simulation. One of the criteria is that the Kinetic Energy (KE) should not be greater than 10 % of the Internal Energy (IE) throughout a simulation [96]. This criterion means that no inertia force due to the mass scaling method should occur. The other criterion is that a ratio of the Artificial strain Energy (AE) to IE should be less than 5 % [97]. Figure 3-4 shows the history of energy balance during the HFMI simulation implementing the material density of 1.0 kg/mm^3 . In the figure, the two criteria are shown by the ratio of each energy. The ratio of KE to IE

is less than 1 % and the ratio of AE to IE is around 5 %. Those ratios satisfy the criteria sufficiently. Thus, the HFMI simulation can be well controlled even though the mass scaling method is adopted.

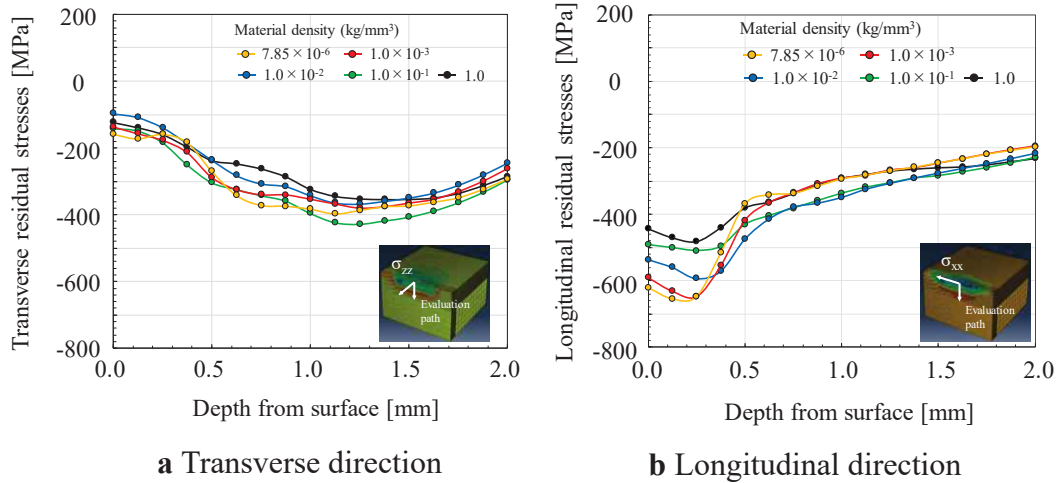


Figure 3-3 Residual stress state obtained from the HFMI simulations using different material densities

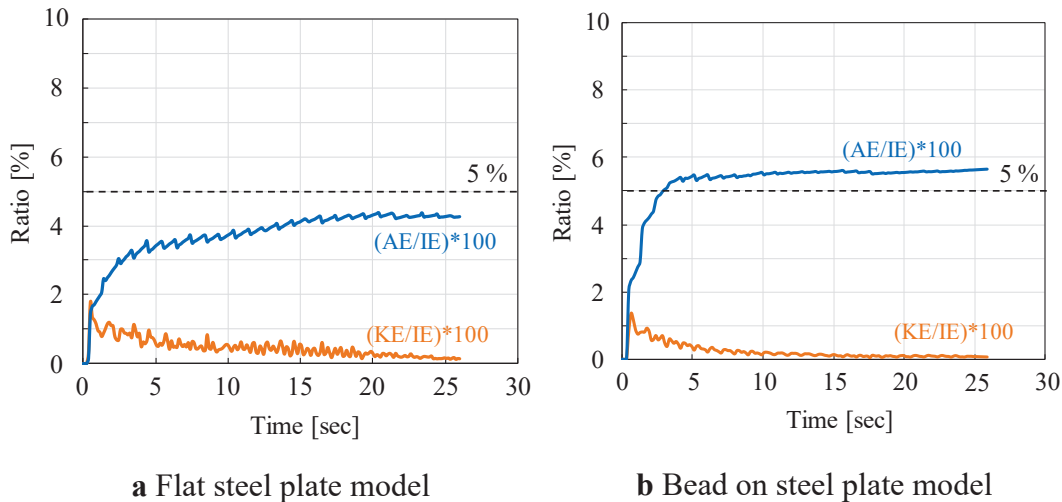


Figure 3-4 History of energy balance during the HFMI simulation using the material density of 1.0 kg/mm³

3.2.4 Investigation of influence of under- and over- treatment on residual stress state

In order to investigate the influence of different HFMI treatment process, such as under- and over- treatment, on residual stress state near the treated surface, the DC HFMI simulation was carried out. Table 3-3 and Figure 3-1c show the investigation cases of under- and over-treatment and settings of the HFMI treatment simulation, respectively.

The feed rate of 0.4 mm/hit and one hit was defined as the “moderate treatment.” Additionally, two types of treatments were simulated. One was over-treatment which changed the number of hits assuming a change of operation frequency. In this investigation, three different number of hits was chosen: two, four, and eight hits. The other was under-treatment which changed the feed rate assuming lower equipment drivability due to large vibration amplitude. Referring to an example of an unacceptable HFMI treatment reported in [14], two feed rates were chosen: 1.0 and 3.0 mm/hits, see Fig.3-1c.

Table 3-3 The list of investigation cases of under- and over-treatment

Treatment	Moderate-	Under-			Over-	
Number of hit [hits]	1	1	1	2	4	8
Feed rate [mm/hit]	0.4	1.0	3.0	0.4	0.4	0.4

3.2.4.1 Influence of under-treatment on residual stress state

Figure 3-5 shows simulated transverse residual stress introduced by HFMI simulation with under-treatments: 1.0 mm/hit and 3.0 mm/hit. The simulation result of the moderate treatment (0.4 mm/hit) and the experimental results with different vibration amplitude measured in the study by Khurshid et al. [40] are also depicted. Figure 3-6 shows the counter figures of the transverse residual stresses by the different feed rates. In these figures, indentation depths averaged from residual stress measurement area are also shown.

For the feed rate of 0.4 mm/hit, the simulated transverse residual stresses show reasonable results in comparison with the experimental results, especially near the treated surface. In depth around 0.1 mm, the simulated transverse residual stress is -140 MPa, which is in very well agreement with the experimental results. A similar observation is reported in the study by Föhrenbach et al. [50], where the HFMI simulations using an isotropic hardening model are performed to the flat steel plate model made of S355 grade steel. However, they showed high degree of simulation accuracy against experimental results not only at the treated surface but also in depth direction. That could be due to the residual stress measurement method, i.e., neutron diffraction and X-ray diffraction methods, because the latter needs surface polishing to measure compressive residual stress in depth. Thus, the influence of the surface removal after the HFMI simulation on

the induced residual stress state is examined later in **section 3.2.5**.

For the feed rate of 1.0 mm/hit, the trend of the simulated transverse residual stress state in depth direction is similar to the trend of the moderate treatment. A difference of the simulated residual stress can be seen slightly at the treated surface. The treatment of 1.0 mm/hit estimates -79 MPa, while the moderate treatment estimates -124 MPa. The amount of introduced compressive residual stress by the feed rate of 1.0 mm/hit is smaller than that by the moderate treatment. In the contour figure of the feed rate of 1.0 mm/hit, individual indentation seams due to HFMI simulation under the 1.0 mm/hit are left on the treated surface. Tensile residual stresses can be seen slightly around the seams. Consequently, the magnitude of compressive residual stress is reduced on the treated surface compared with the moderate treatment. (see Figs. 3-6a and 3-6b). Similar observation can be seen in the experimental results [39], where induced compressive residual stress near the treated surface tends to be small when treatment speed is high and individual strikes are visible. Thus, HFMI treatment where individual indentations are visible on the HFMI treated surface would result in introduction of tensile residual stress around the individual indentation seams.

For the feed rate of 3.0 mm/hit, the trend of the simulated transverse residual stresses is entirely different from the trend of the moderate treatment. Particularly, large differences of the simulated residual stress are observed at the treated surface and at depth of around 1.0 mm. In the contour figure of the feed rate of 3.0 mm/hit as shown in Fig. 3-6c, tensile residual stresses on the treated surface and large compressive residual stress beneath the indentation center can be seen visually. Those stresses do not seem to be homogenized such as the moderate treatment, see Fig. 3-6a. This is due to that the adjacent hit is more than a threshold value of a distance, i.e., 2.0 mm, and hence the adjacent hit does not influence residual stress distribution produced by single HFMI hit [64]. As a result, induced residual stresses were not homogenized, and the tensile residual stress produced by the single HFMI hit was not converted to compressive residual stress. Since the feed rate is large, untreated base plate remains. Therefore, the transverse residual stresses are taken from the untreated base plate between individual indentations (see Fig. 3-6c). From the results, tensile residual stresses are seen on the untreated base plate and compressive residual stresses are produced in a depth of around 1.0 mm. Hence, similar trend is also observed in the results of transverse residual stress state extracted from untreated base plate between individual indentations (see Fig. 3-5). Thus, when individual indentations are completely visible on the treated surface, the introduction of compressive residual stress in transverse direction on the surface cannot be expected even if HFMI treatment is performed.

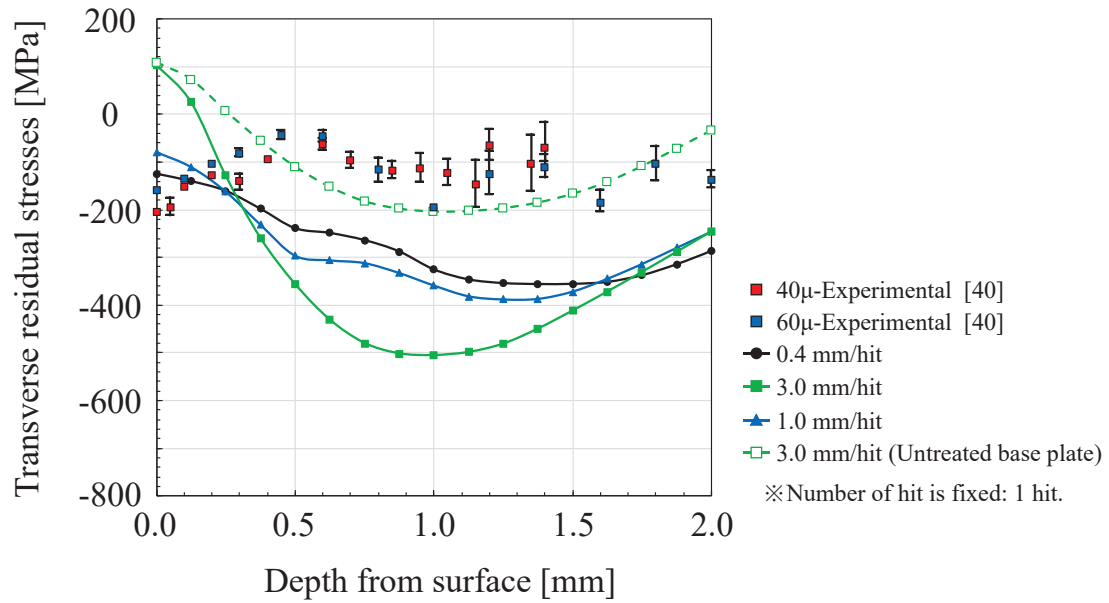
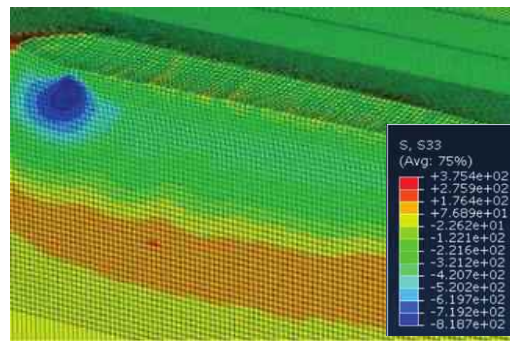
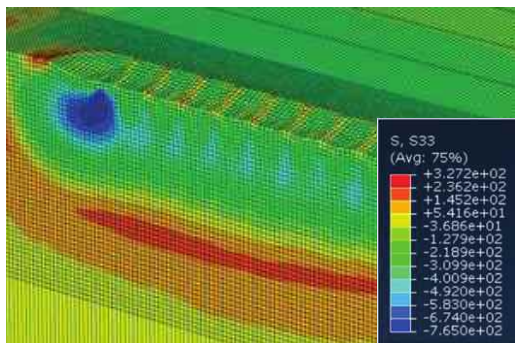


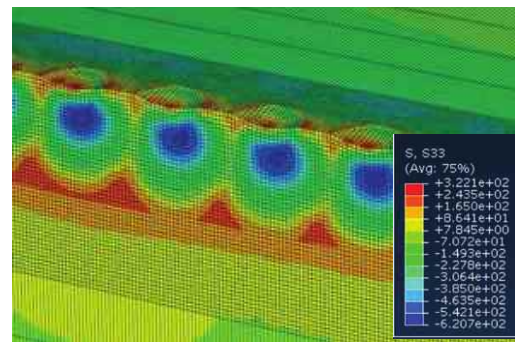
Figure 3-5 Simulated transverse residual stress induced by different feed rates



a Feed rate of 0.4 mm/hit
(Averaged indentation depth: 0.135 mm)



b Feed rate of 1.0 mm/hit
(Averaged indentation depth: 0.133 mm)



c Feed rate of 3.0 mm/hit
(Averaged indentation depth: 0.135 mm)

Figure 3-6 Counter figures of transverse residual stress by the different feed rates

3.2.4.2 Influence of over-treatment on residual stress state

Figure 3-7 shows simulated residual stress state by the HFMI simulation with over-treatments: two, four, and eight hits. Figure 3-8 shows time history during HFMI simulation on the flat steel plate model. The HFMI tool model hits first on the flat steel plate model (see step time 0 s and 0.45 s in Fig. 3-8). During the first HFMI hit, the mesh of the flat steel plate model was deformed. After HFMI simulation, less mesh distortion was observed (see step time 0.9 s in Fig. 3-8) since ALE adaptive mesh that maintains a high-quality mesh was assigned to the area where the HFMI tool hits (see Fig. 3-1c). After the first HFMI hit was finished, the second HFMI hit was conducted on the deformed model as the same manner of the first hit. This procedure was repeated until the second, the fourth, and the eighth hits were finished. Severe mesh deformation was not observed even when the fourth and eighth HFMI hits were finished (see step times 3.6 and 7.2s in Fig. 3-8). Figure 3-9 shows the contour figures in transverse residual stress state by the different number of hits.

For the two hits, the trends of simulated residual stress and magnitudes of induced residual stress in transverse directions are in good agreement with those of moderate treatment. No significant difference between the two hits and the moderate treatment can be observed, especially for less than 0.9 mm depth. Compared to the results of the four hits and the eight hits, the trends and the magnitudes of transverse residual stress show almost the same, although the number of hits is increased. One possible reason is that the investigated material has a relatively low yield strength (see Table 3-2, and Fig. 3-2), and hence it could be considered that the primary hit saturated the induced compressive residual stress near the treated surface. Similar observation can be seen in the study by [61]. They carried out HFMI treatment on a flat steel plate made of S355J2, S690QL, and S960QL grades steels and observed that an amount of introduced compressive residual stress was not increased when S355J2 grade steel was used even when the number of treatments runs increased. As for the indentation depths, it is found that averaged permanent indentation depth is slightly increased in comparison with the moderate treatment, but there is no large variation of the indentation depth from the simulation with the number of two hits (see Fig. 3-9)

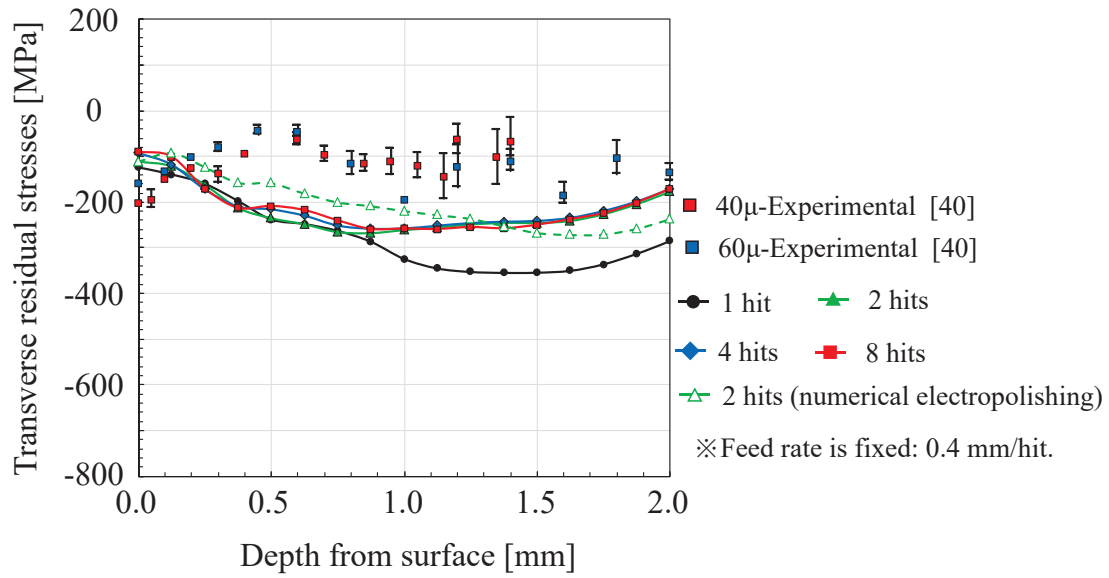


Figure 3-7 Simulated transverse residual stress induced by the different number of hits

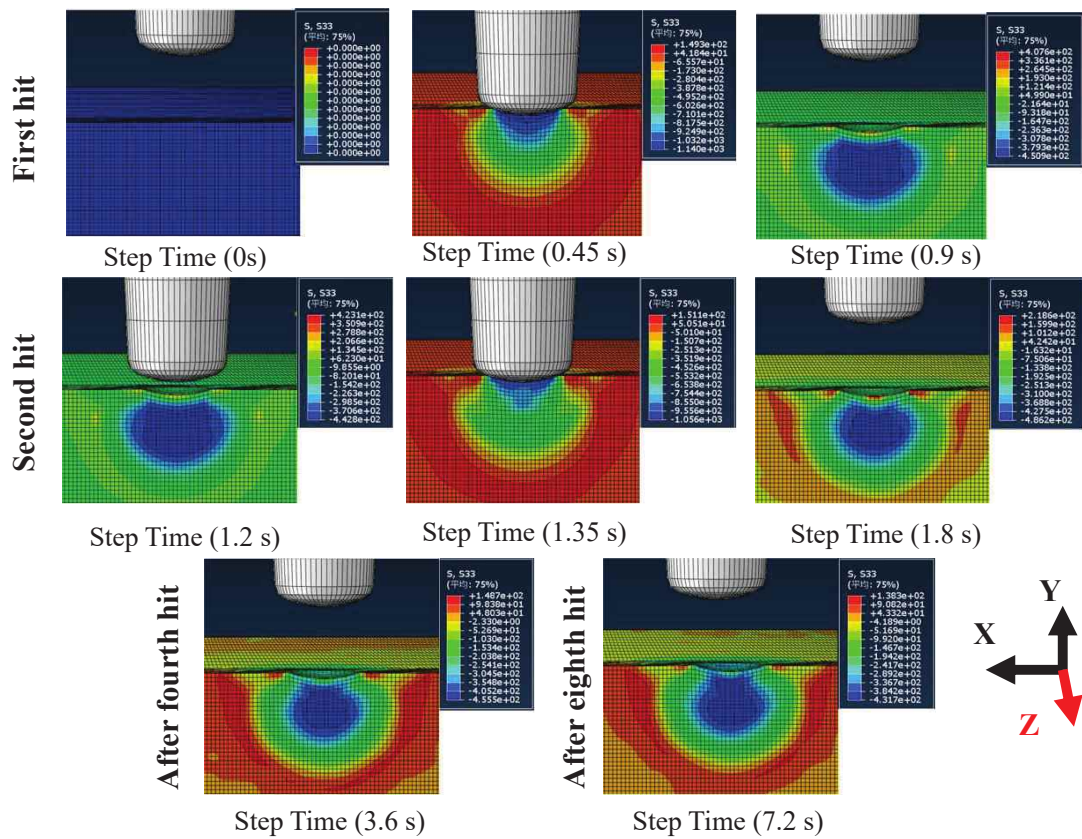


Figure 3-8 Time history of HFMI simulation on the flat steel plate model

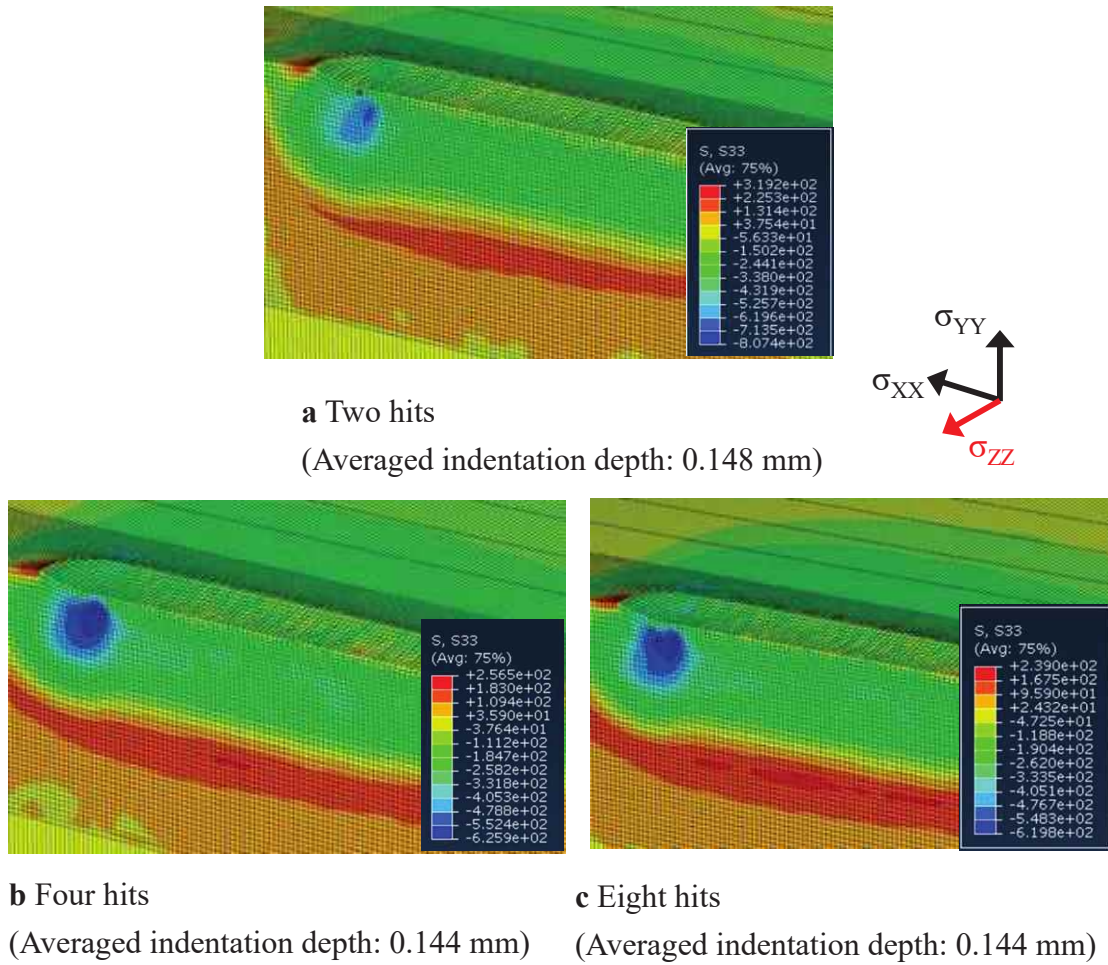


Figure 3-9 Counter figures of transverse residual stress by the different number of hits

3.2.5 Influence of surface removal after HFMI simulation on residual stress state

In order to survey the influence of surface removal after the HFMI simulation on the residual stress state, electropolishing was carried out numerically. This electropolishing was performed with the aid of a function of model change on Abaqus 6.21, with static general solver [70]. Numerical electropolishing was carried out to the result of the HFMI simulation of the number of two hits. A surface removal area of 7.5×15 (the $z \times x$ directions) in mm, as shown in Fig. 3-10, was selected such that the surface removal area corresponds to the experimental one in [40]. Then, the surface of the selected area was removed step by step with an increment of 0.125 mm up to 2.0 mm in depth, see Fig.3-10. The reason why the increment was 0.125mm was because 0.125 mm was the minimum element size of the flat steel plate model. Material properties during the numerical electropolishing were the same as those of the HFMI simulations.

Figure 3-10 shows the result of the numerical electropolishing. It is found that induced compressive residual stresses are redistributed due to the numerical electropolishing. The compressive residual stress in transverse direction is relaxed and is well in agreement with the experimental results in a depth of up to 0.375 mm and in a depth of 1.0 mm. However, the results in a depth around 0.5 mm and in a depth of more than 1.2 mm are overestimated. This could be because large compressive residual stresses left beneath the last hit (see Fig. 3-10) influence residual stress state after the surface removal. Thus, the change of residual stress state due to electropolishing after the HFMI treatment can be reproduced by the numerical electropolishing after the HFMI simulation, and the numerical electropolishing can slightly improve the accuracy of the simulated result in a depth direction.

Although residual stress relaxation/redistribution due to electropolishing after HFMI treatment simulation was reproduced, the trend of estimated residual stress distribution is still different from the experimentally measured results. One possibility of this is scattering of indentation depth. This HFMI simulation used averaged indentation depth of 0.14 mm. However, actual measured indentation depths were in the range of 0.11 mm to 0.18 mm [40]. The indentation depth on the location where the residual stresses were measured is unknown, and hence the indentation depth would be different from the one used in this HFMI simulation. Therefore, further investigation on influence of the indentation depth on the induced residual stress state would be required, which is outside scope of this thesis.

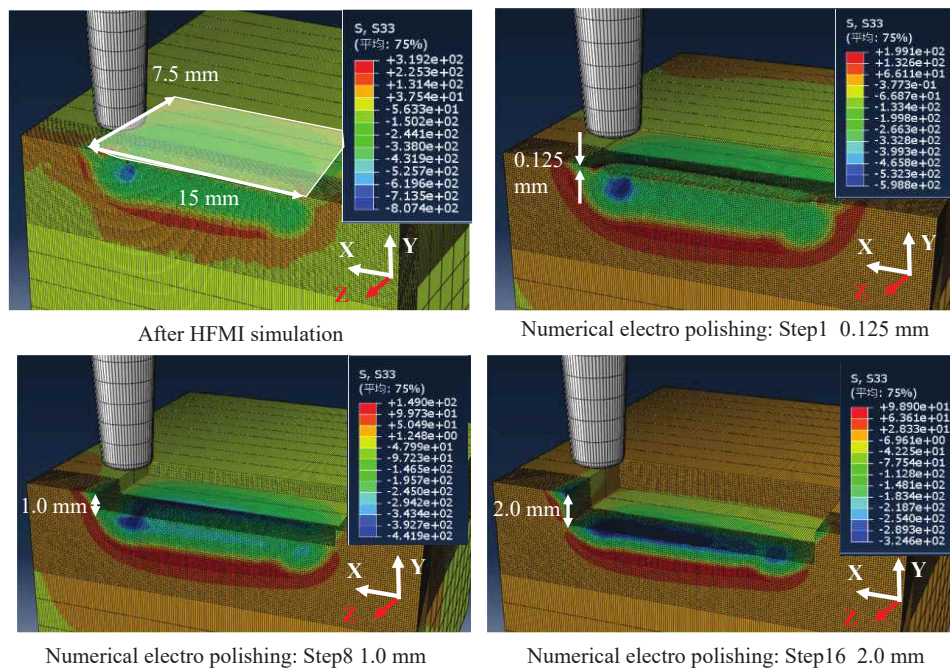


Figure 3-10 Numerical electropolishing after HFMI simulation

3.3 HFMI simulation to bead on steel plate model

3.3.1 Peening treatment on bead on steel plate specimen

Figure 3-11 shows the bead on steel plate specimen made of Japan Industrial Standard (JIS)-SM400. Table 3-4 shows the mechanical property of JIS-SM400. The dimension of the bead on steel plate specimen was $200 \times 200 \times 12$ (width \times height \times thickness) in mm. The welding was conducted 150 mm long on the base steel plate. MX-Z200 (JIS-Z3313) electrode was used in the CO₂ type of welding. The bead on steel plate specimen was treated by Portable Pneumatic needle-Peening (PPP). The PPP is one of the post weld treatment methods, yet it is not categorized as HFMI. The PPP equipment uses a needle pin with a 1.5 mm radius vibrated by compression air. The PPP was performed on both sides of the weld toes, with the condition of the PPP treatment according to [98]. After the PPP treatment, residual stresses were measured at the center of peened area, with the aid of portable X-ray residual stress analyzer, called μ -360n made by PULSTEC Industrial Co., Ltd. Cos α method using $K\alpha$ radiation of chromium was utilized, and a collimator was 2.0 mm in a diameter. Residual stress measurement was performed step by step up to a depth of 1.0 mm, with the aid of using electropolishing.

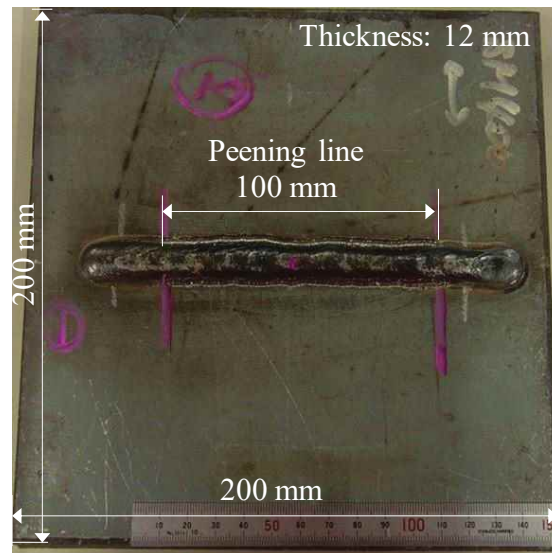


Figure 3-11 Bead on steel plate specimen

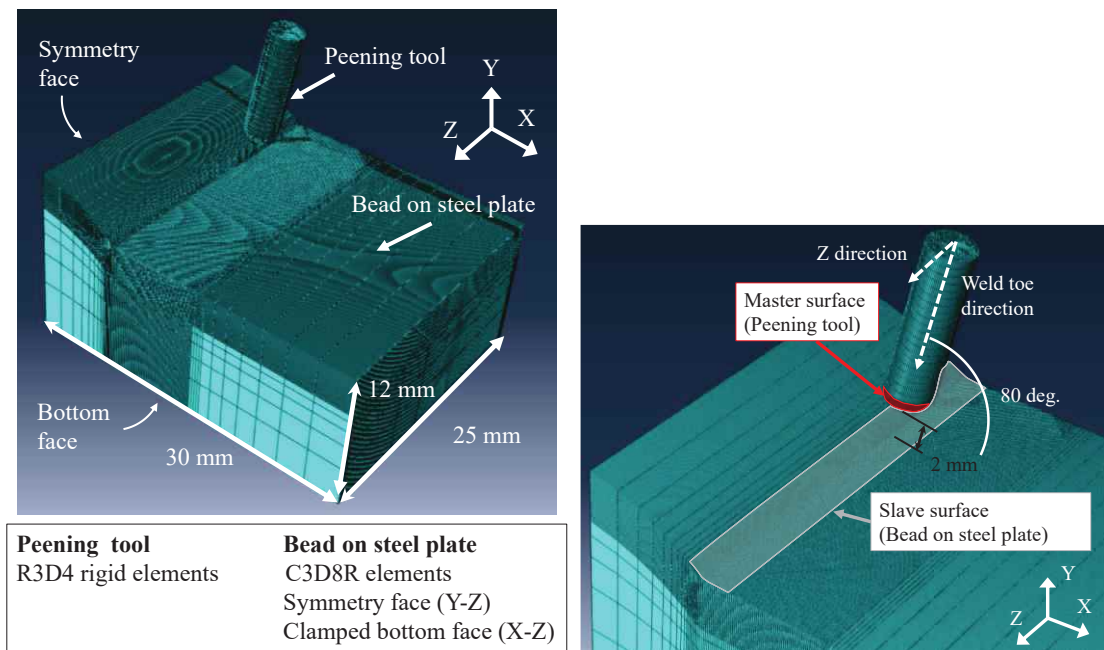
Table 3-4 Mechanical properties and chemical composition of SM400

Type of steel	Yield strength	Tensile strength	Elongation	Chemical composition [%]				
				C	Si	Mn	P	S
	[MPa]		[%]	$\times 100$			$\times 1000$	
SM400	288	429	31	17	19	51	19	5

3.3.2 FE modeling of bead on steel plate specimen and peening tool

Figure 3-12 shows the bead on steel plate model used in FE HFMI simulation. A small section of the bead on steel plate specimen shown in Fig. 3-11 was modeled. The dimension of the bead on steel plate model was $30 \times 25 \times 12$ (width \times depth \times height) in mm. Boundary conditions were given in the Y–Z plane ($u_x=0$) and the bottom face (the X–Z plane, $u_x=u_y=u_z=0$). The shape of the welded bead was modeled by using the experimentally measured mean values of the dimensions, resulting in the weld radius and the flank angle of the model being set to 0.6 mm and 143 deg, respectively. The HFMI tool was modeled by 1.5×10 (tip radius \times length) in mm. For the bead on steel plate model and the HFMI tool model, the element type, minimum mesh size, and contact algorithm were the same as the HFMI simulation described in **section 3.2.1**. Since large deformation was anticipated during the HFMI simulation, ALE adaptive meshing was assigned to the area of hits, see Fig.3-12b.

The HFMI tool model was moved toward the weld toe direction and the Z-direction in order to carry out by DC HFMI simulation. The inclination angle was 80 deg, as shown in Fig. 3-12b. The enforced displacement was given toward the weld toe direction so that permanent indentation depth was set to 0.21 mm, which is in accordance with the experimentally measured mean value. The HFMI treatment simulation was carried out 10 mm in the Z-direction by the feed rate of 0.4 mm/hit.



a The bead on steel plate model

b Setting of HFMI tool

Figure 3-12 The bead on steel plate model used in FE HFMI simulation

For the hardening model, the isotropic hardening model of S355 grade steel was employed since JIS-SM400 grade steel has similar mechanical properties (see Tables 3-2 and 3-4). In this simulation, the change of the material properties of heat affected zone and welded zone due to the welding process were not considered. According to [46], when the influences of residual stress field caused by the welding is not considered, it leads to approximately 15% higher surface compressive residual stress. Thus, it is assumed that the influence of welding residual stress on estimated residual stress could be comparably small value. It is noted that the influence of welding residual stress on induced residual stress by HFMI is considered later in **Chapter 4**, and it is confirmed that the influence is a minor, see **section 4.4**.

3.3.3 Comparison of experimental and simulation results

Figure 3-13 shows the comparison of experimental and simulation results. Simulated residual stresses were averaged over multiple integration points corresponding to the area of 1.0 mm. This is because averaged residual stress values corresponding to the area of 1.0 mm were almost similar to the ones corresponding to the area of 2.0 mm. Since the mass scaling method was employed in the simulation, the energy balance during the HFMI simulation was examined. From the result, it is confirmed that the simulation was well controlled (see Fig. 3-4b). Figure 3-14 shows time history during HFMI simulation to bead on steel plate model. Although the depression area of the bead on steel plate model is larger than the one of the flat steel plate model because the HFMI tool hits the weld toe, large mesh deformation was not confirmed due to the hit and hence the mesh quality was maintained throughout the HFMI simulation, see Fig. 3-14.

From the experimental results, introduced compressive residual stress can be observed up to 1.0 mm in depth. At 0.125 mm in depth, the compressive residual stress is around -150 MPa. The maximum compressive residual stress is -300 MPa at 1.0 mm in depth. The magnitude of compressive residual stress tends to increase as the depth increases. From the simulation results, the estimated residual stress is relatively in well agreement with experimental results in depth around 0.125 mm to 0.375 mm, even when the residual stress due to welding are not considered in the model. However, estimated residual stresses are slightly larger than experimental ones in more than 0.5 mm depth. This could be because the yield strength of S355 is larger than that of SM400 (see Tables 3-1 and 3-4). Thus, the DC simulation can give reasonable results in a depth of around 0.2 mm even when welding residual stress is not considered.

In addition, in order to confirm whether an accuracy of simulated results to experimental results can be improved, the HFMI simulation with the number of two hits

was performed, and the numerical electropolishing was conducted, as similar to **section 3.2.5**. The results show that the residual stresses in a depth of more than 0.5 mm are relaxed due to surface removal. The value of simulated result, especially in the depth of 0.775 mm, becomes close to that of experimental result. Thus, applicability of numerical electropolishing after HFMI simulation can be confirmed to the bead on steel plate model.

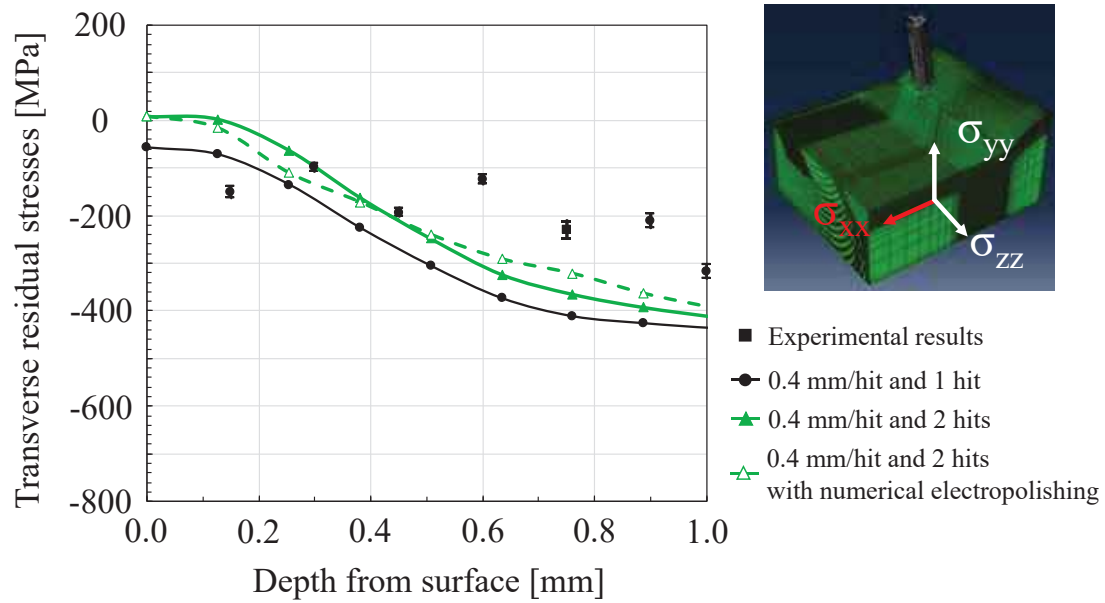


Figure 3-13 Comparison of experimental and simulation results

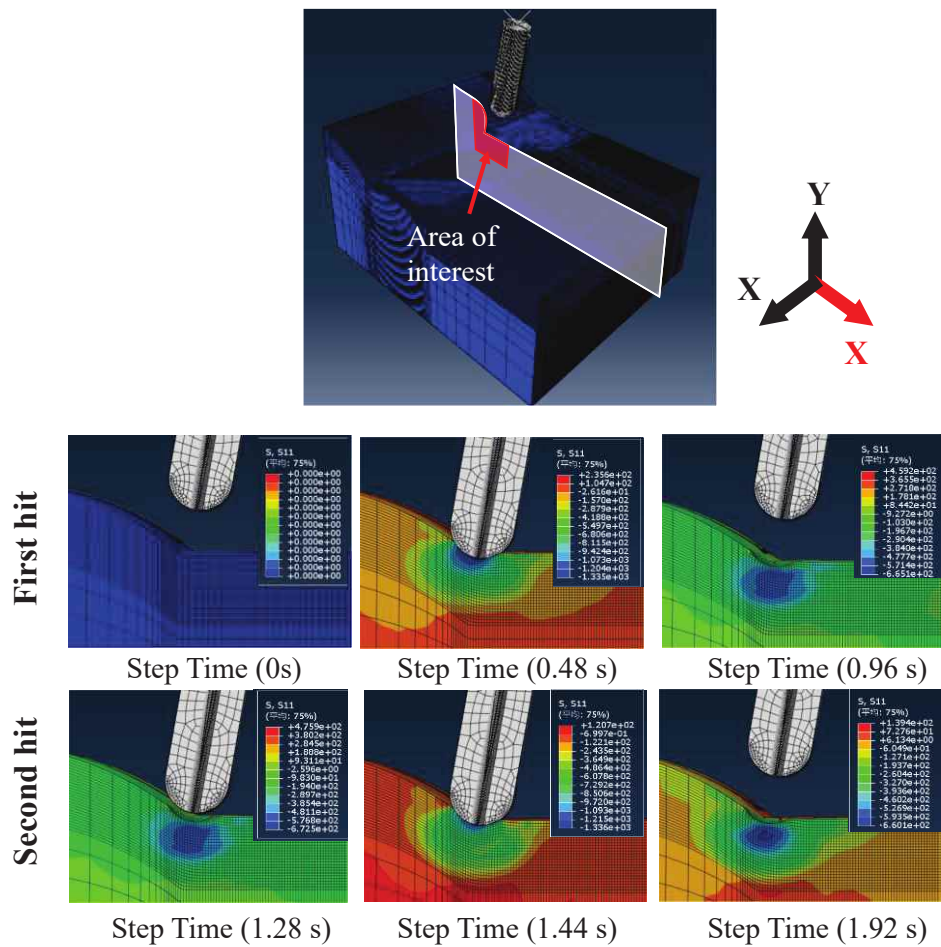


Figure 3-14 Time history during HFMI simulation on the bead on steel plate model

3.4 Conclusions

The objective of this chapter is to verify the validity of HFMI simulation implementing an isotropic hardening model for residual stress estimation using a flat and bead on steel plates models. The HFMI simulations were performed on the flat steel plate model, and the influence of the feed rate and the number of hits on residual stress state was investigated. In addition, electropolishing after the HFMI simulation was conducted to examine the influence of surface removal on residual stress state. Then, the HFMI simulations were carried out on the bead on steel plate model, and the estimated residual stresses were compared with experimental measurement results. The conclusions can be summarized as followings:

1. When the mass scaling method is employed in the HFMI simulations, simulation time of more than 90 % can be reduced in comparison with the time by the simulations without the mass scaling method. However, when longitudinal residual stresses are of importance, it must carefully consider the usage of the mass scaling method.
2. From the under-treatment simulations, it is observed that high feed rate of treatment can influence residual stress state near the treated surfaces. When individual indentations are visible on the treated surface, tensile residual stress in transverse direction would be introduced around individual indentations even if HFMI treatment is performed.
3. From the over-treatment simulations, it is observed that increase in the number of hits is independent of the amount of induced residual stress. This is because the amount of induced compressive residual stress could be saturated by the primary hit in case yield strength is low.
4. With surface removal due to electropolishing conducted after the HFMI simulation, a change of induced residual stress can be reproduced, and the accuracy of the numerically estimated residual stress in a depth direction can be slightly improved.
5. From the HFMI simulation against based on steel plate model, it is found that the simulations using isotropic hardening model can give reasonable estimation of the residual stresses in a depth of 0.2 mm even when the residual stresses due to the welding are disregarded in the model.

Chapter 4

Defect tolerance analysis considering crack opening-closing behavior in HFMI treated welds

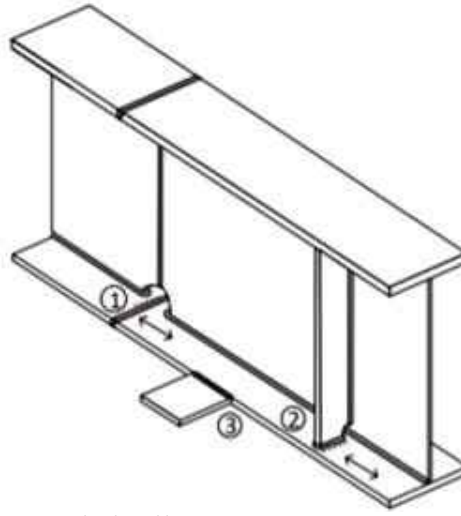
4.1 Introduction

The objective of this chapter is to understand the effect of HFMI treatment on pre-fatigued welds and crack opening-closing behavior in HFMI treated welds based on HFMI simulation using a combined hardening model. The rat-hole detailed weld, which is one of the fatigue-prone details in steel bridges, was used in the HFMI simulation. In order to simulate initial cracks, the detailed rat-hole models included a rectangle slit with different depths in their weld toes. Elastic thermal analysis was used to estimate initial welding residual stress. Then, the HFMI simulation and subsequent initial axial cyclic loading was conducted. Induced compressive residual stress, change of slit geometry, and opening-closing behavior of the HFMI treated slit under axial loading were investigated numerically.

In addition, the crack opening-closing behavior was investigated experimentally using pre-fatigued out-of-plane gusset welded joint specimen treated by Impact Crack-Closure Retrofit (ICR) treatment, with the aid of an ultrasonic testing system. The behavior was examined based on a change of echo height ratio from the crack.

4.2 Review of experimental study on pre-fatigued rat-hole specimen treated by HFMI

In order to investigate the effect of HFMI treatment on fatigue life extension of pre-fatigued welded joints, three different details of welded joints where fatigue cracks typically occur in steel bridges were selected and tested in the previous study [80]. Figure 4-1 shows the three different details of welded joints. Figure 4-2 shows the geometry of the rat-hole specimen which is made of S355 grade steel with plate thickness 16 mm. The gusset height is 100 mm. For the fatigue test using the rat-hole specimen, in order to examine the effect of cracks in HFMI treated welds on the fatigue life extension, the cracks were measured using ultrasonic testing-time off flight diffraction. HFMI treatment was carried out, and fatigue tests were conducted under axial constant loading, where the applied maximum and minimum stresses were 150 and 15 MPa. It was found that HFMI treatment gives superior fatigue life even when existing fatigue cracks are shallower than 1.5 mm through plate thickness.



- ① Rat-hole or notch detail
- ② The welded detail between vertical stiffener and girder flange
- ③ The gusset plate connection to girder flange

Fig.4-1 Three different details of welded joints [80]

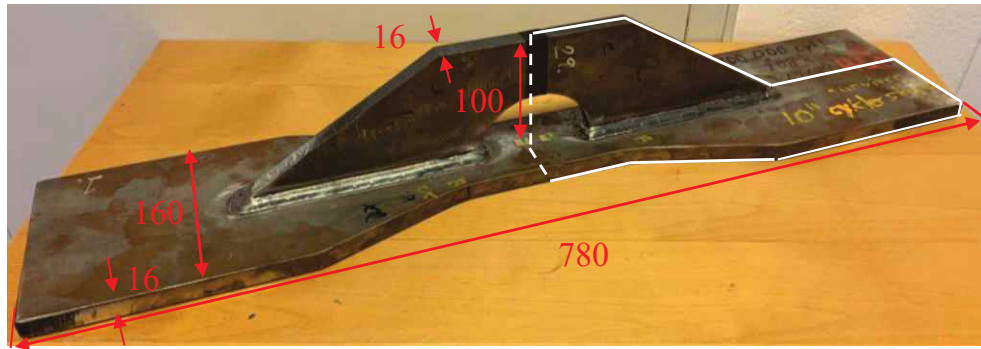


Fig. 4-2 The geometry of the rat-hole detailed specimen [Unit: mm]

4.3 Numerical investigation of defect tolerance considering crack opening-closing behavior on pre-fatigued welded joints treated by HFMI

4.3.1 Modeling of the specimen and fatigue crack

In order to understand the effect of HFMI treatment on pre-fatigued welds and crack opening-closing behavior in HFMI treated welds, the rat-hole welded specimen shown in Fig 4-2 was used in the HFMI simulation. Figure 4-3 shows the FE simulation model of the rat-hole specimen, hereafter called the rat-hole model. A quarter model was employed, as shown in 4-3a. For each symmetry face of the rat-hole model, boundary conditions were defined: $u_z=r_x=r_y=0$ for the X-Y plane and $u_x=r_y=r_z=0$ for the Y-Z plane. For the bottom face (the X-Z plane), $u_y=0$ was defined since cyclic loading to the X-

direction was applied after the HFMI simulation, see green arrows in Fig. 4-3a. The rat-hole model consisted of 8-node brick elements with reduced integration (C3D8R). Hourglass control with stiffness was used to prevent large element distortion during the HFMI simulation. In addition, ALE adaptive meshing was adopted around the area where the HFMI tool hit. The minimum element edge length of 0.125 mm recommended by Föhrenbach et al. [50] was used. For the weld bead modeling, the experimentally measured mean values of the dimensions were used, resulting in the leg length and the weld radius being set to 7.5 mm and 0.5 mm, respectively.

Figure 4-3b shows model of the HFMI tool. The tip diameter and tip radius of the HFMI tool were 3.0 and 1.5 mm, respectively. The HFMI tool was modeled as a rigid body in order to reduce simulation time and consisted of 4-node tetrahedral elements (C3D4). A contact pair was defined between the HFMI tool model (master surface) and the rat-hole model (slave surface), as shown in right figure of Fig.4-3b, using penalty contact algorithm with a friction coefficient $\mu=0.15$.

HFMI simulation was performed based on Displacement-Controlled (DC) simulation. To perform the DC HFMI simulation along the weld seam, 31 different strikes with the HFMI tool were set, as shown in the left figure of Fig. 4-3b. The HFMI strikes were numbered in counterclockwise order. First, the two HFMI strikes numbered as 1 and 2 set in front of the weld toe were moved toward the weld toe direction and the Z-direction, as shown right figure of Fig. 4-3b. Although the experimentally mean measured value of indentation depth after HFMI treatment was around 0.3 mm, an enforced displacement toward the weld toe direction was set so that an indentation depth after HFMI treatment simulation is about 0.2 mm. This modeling adjustment is used since the DC HFMI simulation with slit failed due to large deformation occurred when indentation depth of more than 0.2 mm is used. HFMI treatment was carried out 8 mm along the Z-direction by the feed rate of 0.4 mm/hit, i.e., totally 20 HFMI hits. Then, HFMI tools that were numbered from 3 to 31 start the HFMI treatment simulation in the numbered order, see left figure of Fig. 4-3b. Those HFMI tools were lined up such that the distance of the adjacent one is 0.4 mm and hence moved toward the weld toe direction only, i.e., totally 29 HFMI hits were carried out. The inclination angle of the HFMI tool was set as 70 degrees. During the DC HFMI simulation, the rat-hole specimen was stationary. For the DC HFMI simulation, Abaqus Explicit solver was used.

Pre-existing toe crack was simulated as a rectangle slit, for the sake of simplicity. The rectangle slit was inserted in the center of the weld toe, as shown in Fig. 4-3c. The slit depth and width were determined using the proposed formula for the ends of longitudinal stiffeners using Eq. (4-1) [99].

$$c = \frac{6.71 + 2.58 \cdot a}{2} \text{ [mm]} \quad (\text{Eq.4-1})$$

where a is fatigue crack depth [mm] and c is fatigue crack width [mm]. Since the effect of HFMI treatment on the life extension for the rat-hole welded specimen shown in Fig. 4-2 can be limited by the existing toe crack size of more than 1.5 mm [80], the slit depth was up to 2.0 mm every 0.5 mm, i.e., 0.5-, 1.0-, 1.5- and 2.0 mm as shown table in Fig. 4-3c. As aforementioned, the DC HFMI simulation to the model with slit failed due to that large mesh deformation occurs when indentation depth of more than 0.2 mm was given. This deformation was caused due to that the slit nodes on the meshes penetrate themselves. Hence, in order to prevent node penetration on the slit faces due to the deformation by the HFMI treatment, kinematic contact algorithm, in which any penetration is not allowed, was assigned on the slit faces with the friction coefficient $\mu=0.15$. Thereby, the DC simulation to the model with the slit was successful under the condition of indentation depth of 0.2 mm.

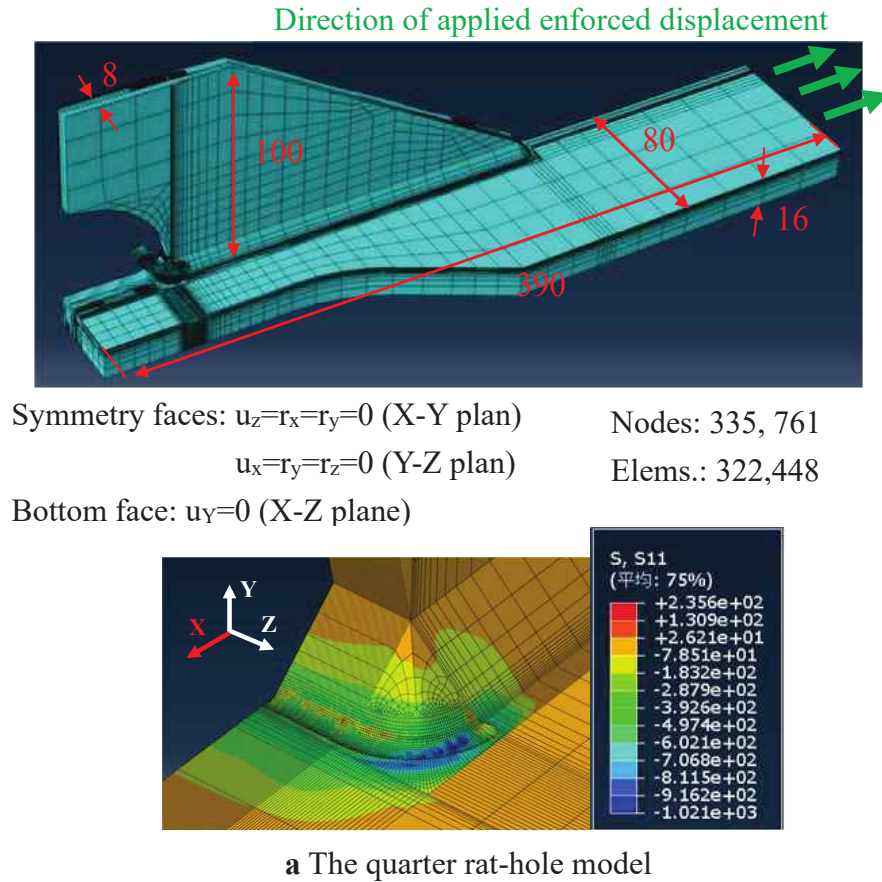
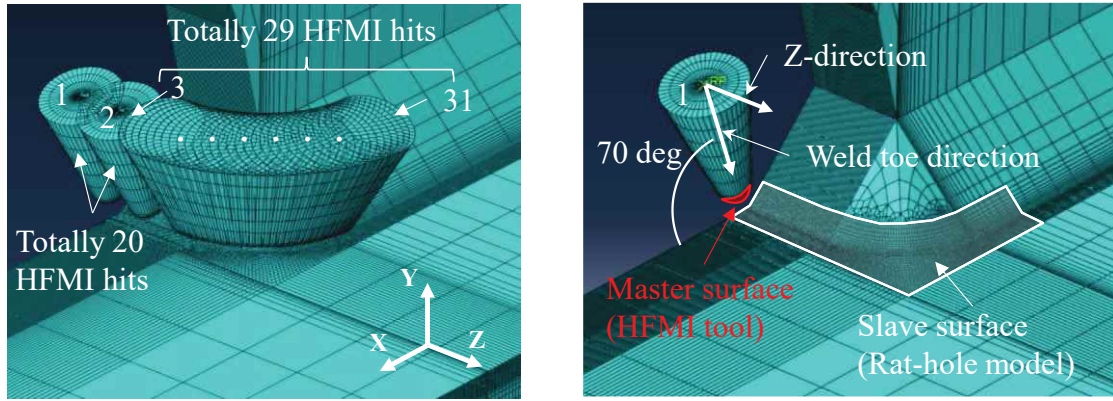
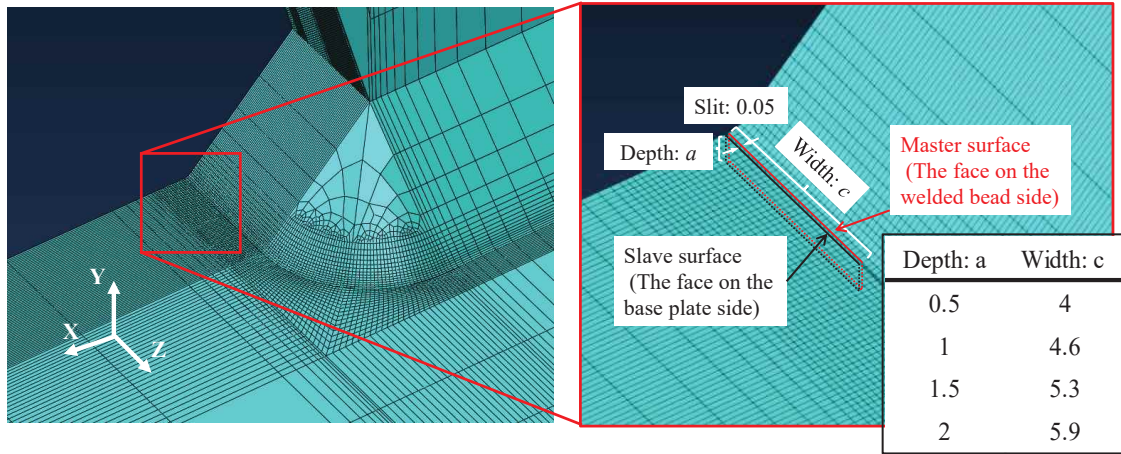


Figure 4-3 The rat-hole model used in FE HFMI simulation



b HFMI tool setting



c Rectangle slit inserted in the weld toe of the rate-hole model

Figure 4-3 The rat-hole model used in FE HFMI simulation (Continued)

4.3.2 Material hardening model

Typically, two types of material hardening models have been often used in HFMI simulation: isotropic hardening model and combined isotropic and kinematic hardening model. The latter is well known as the Chaboche model [69]. Khurshid et al. [40] recommended that the Chaboche model can be the most appropriate for FE simulation of residual stress state if subsequent relaxation due to external cyclic loading is studied. In this study, HFMI simulation and subsequent initial cyclic loading will be performed in order to investigate the opening-closing behavior of the slit in the rat-hole model. The induced compressive residual stress by the HFMI simulation may be relaxed while the rat-hole model is subjected to cyclic loading. Therefore, the Chaboche model was adopted in this study.

Material properties in the weld bead would be different from those in the base steel plates due to welding processes itself. Leitner et al. [45] carried out welding

simulation with material properties for S355 grade steel where the subsequent DC HFMI simulation was carried out on a model including the welding residual stresses from the welding simulation as initial stresses. The result showed that compressive residual stress filed after the HFMI simulation and the residual stress redistribution after applying initial cyclic loading could be estimated well. The material properties in [45] were used in this study. The mechanical weld heterogeneity in terms of final residual stress state is of a secondary importance since the previous studies [45, 46] have shown the influence of welding residual stress on the final residual stress state after the HFMI simulation is less than 15 %. Hence, the mechanical weld heterogeneity was not considered in this study. An elastic modulus $E=2.0 \times 10^6$ MPa and poisson's ratio $\nu=0.3$ were used in all simulations.

4.3.3 Elastic thermal analysis for initial welding residual stress

Welding residual stress estimation using FE simulation is demanding and requires long computational time. The amount of studies where welding FE simulations in combination with HFMI simulations are not many [45, 46]. Even when the welding residual stress is ignored, the difference of the magnitude of the induced compressive residual stress after the HFMI simulation in a model consisting of S355 grade steel is approximately 15 % [45, 46], and therefore the influence of the welding residual stress on the HFMI introduced compressive residual stress is small. However, it may be anticipated that the influence of the welding residual stress is larger when the yield strength of the base material is larger, e.g., high strength steel. An alternative approach replacing the welding simulation in order to include the welding residual stresses in the model could be used. In this study, elastic thermal analysis was used to estimate initial welding residual stress.

The initial welding residual stress distributions were estimated by means of a predefined temperature field in Abaqus [70]. Figure 4-4 shows the area to input temperature field. To produce temperature field, temperature gradient is needed. In order to generate temperature gradient, the origin (weld toe) and on ± 2 mm from the origin were selected as temperature value input lines, as shown in left figure of Fig.4-4. Then, in 3D volume, keeping the selected three lines, the area was 8 mm in the Z-direction from the origin, see right figure of Fig.4-4. Thereafter, temperature values were given to the three lines. The temperature values, ΔT , were determined by converting the predefined residual stress by using Eq. 4-2.

$$\Delta T = \frac{\sigma_{RS}}{E \cdot \alpha} \quad (\text{Eq. 4-2})$$

where α is the thermal expansion coefficient, with $\alpha = 1.2 \times 10^{-5}$ being used. The benefit of this approach is that the initial residual stress can be estimated as the initial step before starting the HFMI simulation step and automatically calibrated considering the stress-equilibrium within the selected region.

The predicted residual stress distribution was estimated by probabilistic analysis using more than 100 experimental data of residual stress distribution collected from the literature covering yield strength between 307 and 1050 MPa and for different welded details with varying thicknesses from 5 to 100 mm [100]. The residual stress distribution can be determined by using Eqs. (4-3), (4-4), and (4-5).

$$RS_{the\ surface} = 0.35 \cdot f_y \text{ [MPa]} \quad (\text{Eq.4-3})$$

$$RS_{the\ knee\ point} = -0.2 \cdot f_y \text{ [MPa]} \quad (\text{Eq.4-4})$$

$$The\ knee\ point = 0.35 \cdot T \text{ [mm]} \quad (\text{Eq.4-5})$$

where f_y is yield strength and T is plate thickness of a specimen. In this study, $f_y = 390$ [MPa] and $T = 16$ [mm] of the rat-hole model were used. The residual stresses on the surface are estimated as 137 and -78 MPa, and the knee point is determined as 5.6 mm in depth, see the black solid line in Fig. 4-5. Note that, mesh distortion due to thermal strain was as quite minute as can be ignored, as shown in Fig. 4-4, because the mesh distortion was controlled by ALE adaptive meshing being assigned to the area for the sake of subsequent HFMI simulation. Figure 4-5 also shows the estimated residual stress distribution resulting in the elastic thermal analysis conducted for the rat-hole models without and with different slit depths, see the black dot line and the colored solid lines in Fig. 4-5. It should be note that residual stress redistribution due to fatigue crack initiation and/or propagation to the slit depths was not considered and the initial welding residual stresses were given to the rat-hole models such that the magnitude of residual stress at slit tip corresponds with that of determined residual stress at the same depth of the slit tip. Therefore, consideration of residual stress relaxation and/or redistribution could result in a large difference in initial welding residual stress. Hence, this would require further investigation and simulation, which is outside scope of this thesis.

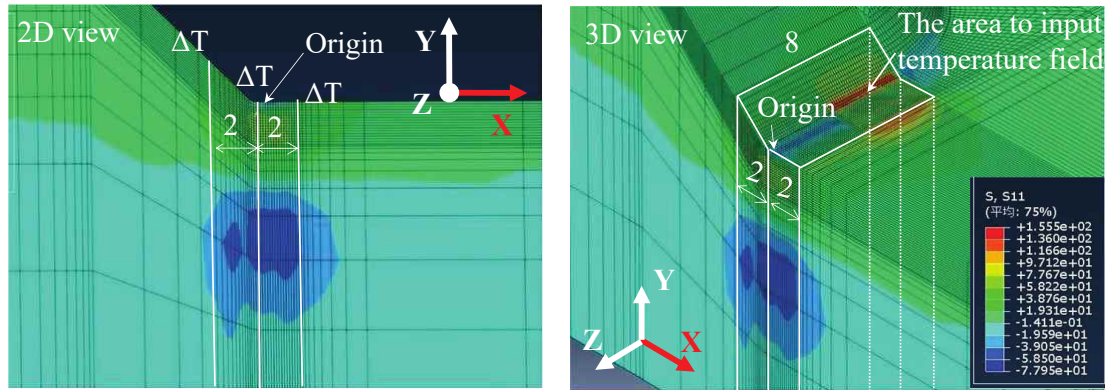


Fig. 4-4 Elastic thermal analysis [Unit: mm]

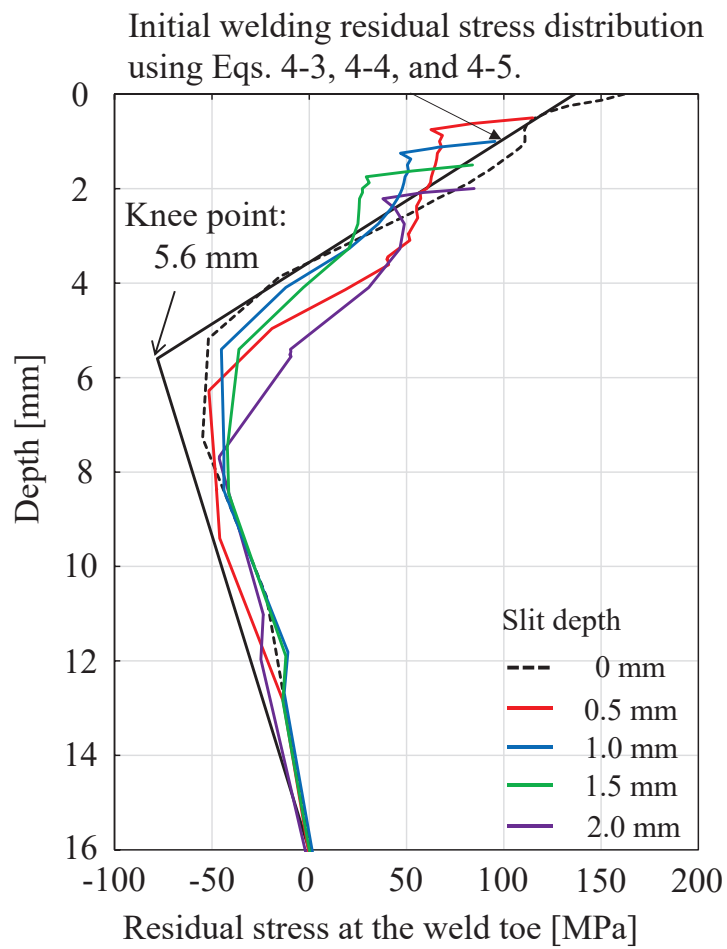


Fig. 4-5 Initial welding residual stress distributions by elastic thermal analysis

4.3.4 Applied cyclic loading

After HFMI simulation, initial cyclic loading was applied to the rat-hole model to examine the opening-closing behavior of the HFMI treated slit. Enforced displacements were applied to the model in the X-direction, see Fig. 4-3a. The generated stresses by the enforced displacements were monitored on the base plate, nominal stress. Following the study in [80], the maximum nominal stress of about 150 MPa was applied in this study. The minimum nominal stress was around 0 MPa. Hence, the applied stress amplitude was about 150 MPa.

4.4 Numerical investigation results

The rat-hole model has a rectangular slit in the center of its weld toe. When a semi-elliptical fatigue crack is assumed and overlaid to the slit, the left side of the rectangle slit corresponds with the deepest crack area, see Fig. 4-6. Therefore, the effect of HFMI treatment on pre-fatigued welds, such as induced compressive residual stress, change of slit geometry, and opening-closing behavior of the slit after HFMI treatment simulation was observed at the area of interest shown in Fig. 4-6 in the following sections.

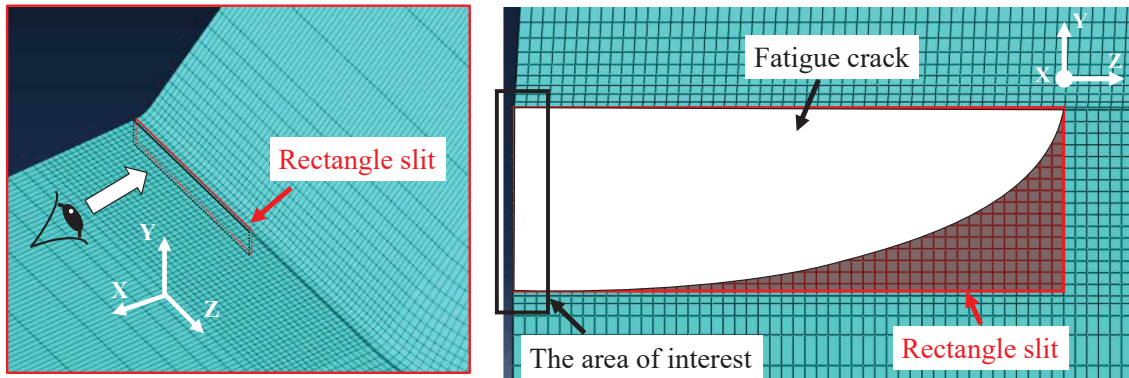


Fig. 4-6 The area of interest for defect tolerance considering crack opening-closing behavior

4.4.1 Induced compressive residual stress

Figure 4-7 shows the results from the HFMI simulations with and without the slits. The averaged four elements value on the longitudinal stress (the X-direction) is shown. Figure 4-7a shows the influence of initial, welding, residual stress on induced compressive residual stress. The compressive residual stress, due to the HFMI treatment, without the initial welding residual stress indicates -161 MPa at the treated surface while the compressive residual stresses when the initial welding residual stress is considered are -135 MPa. It can be concluded that there is a minor difference in the compressive

residual stress when the initial welding residual stress is disregarded in the HFMI simulation, less than 15 %. This difference agrees well with previous studies [45, 46]. Thus, a methodology for incorporating the initial welding residual stress in a simplified way is implemented and the simulation shows that the initial welding residual stress have a minor effect on the compressive residual stress due to the HFMI treatment.

Figure 4-8 show the residual stress distribution during HFMI treatment simulation on the rat-hole models including the slit with different depths. For the slit depth of 0.5 mm, it can be found that significant compressive residual stress was produced around the slit tip and compressive residual stress field is produced up to 2.5 mm, see total time 0.8 in Fig. 4-8a. The produced compressive residual stress is homogenized by

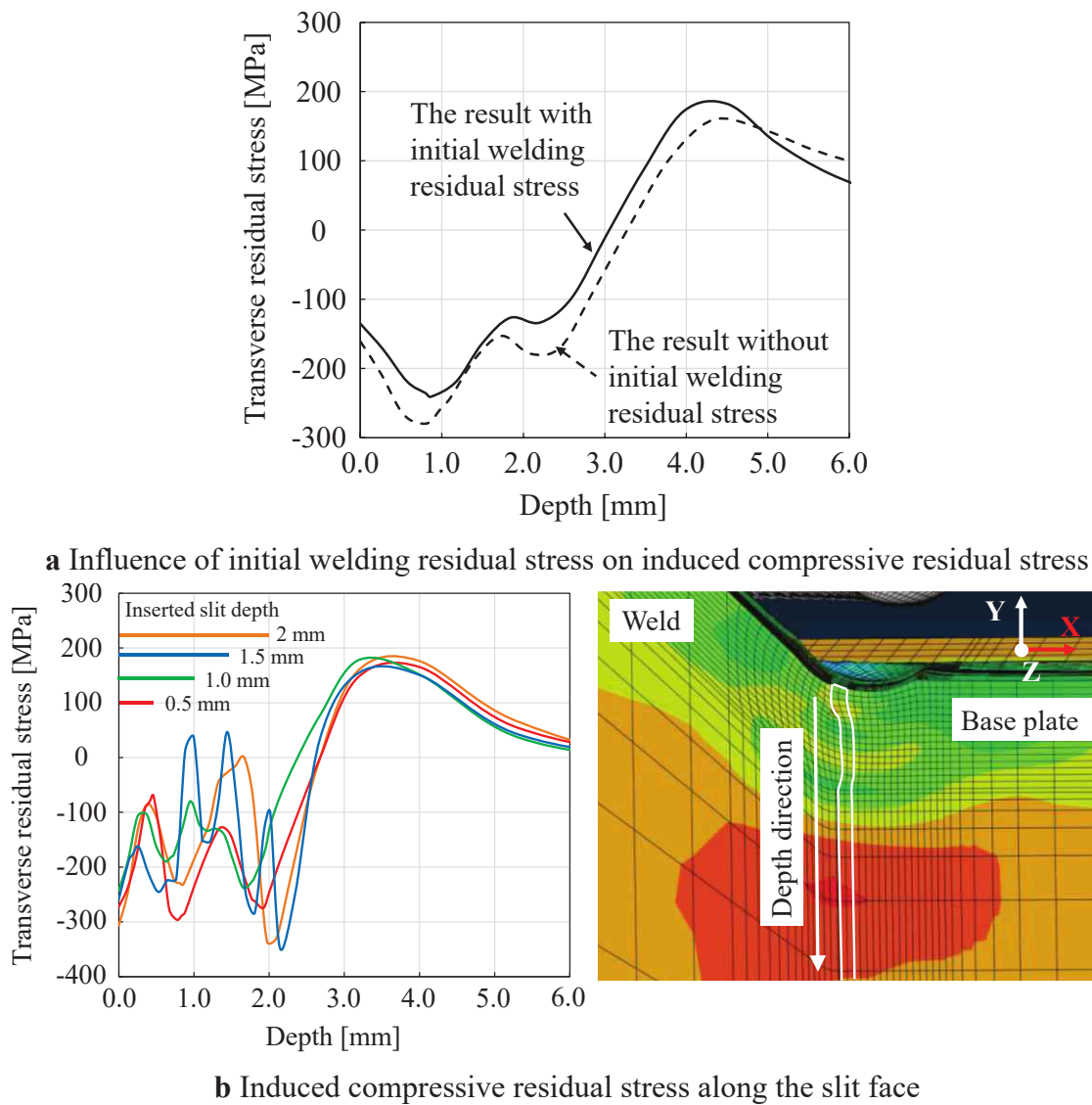
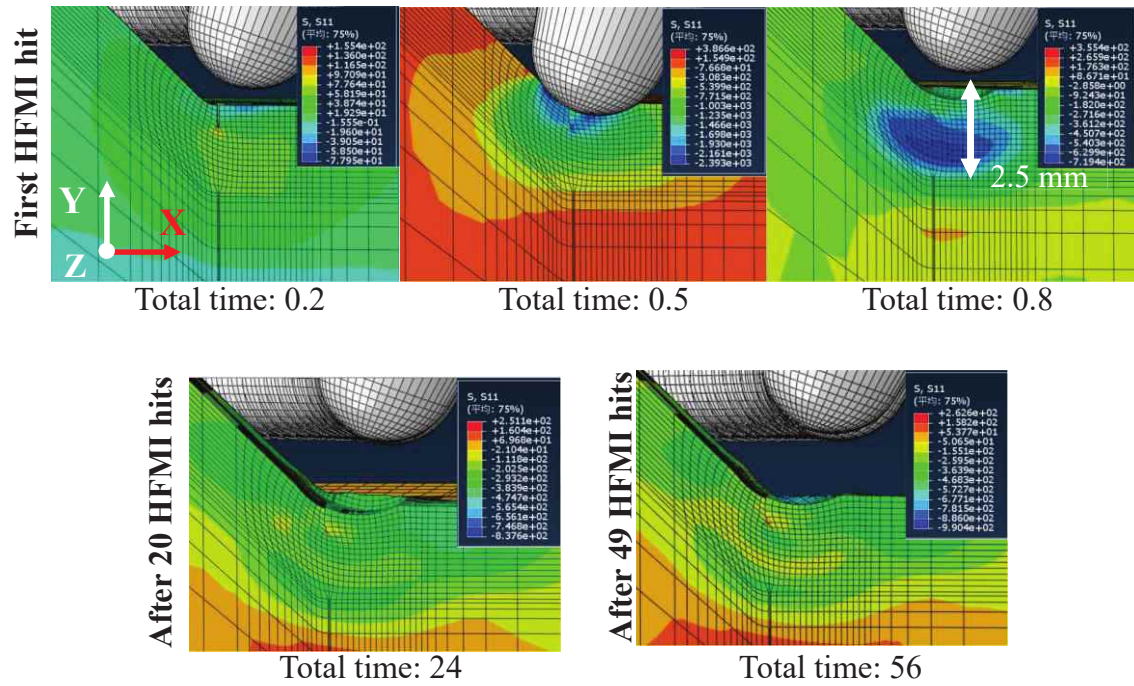


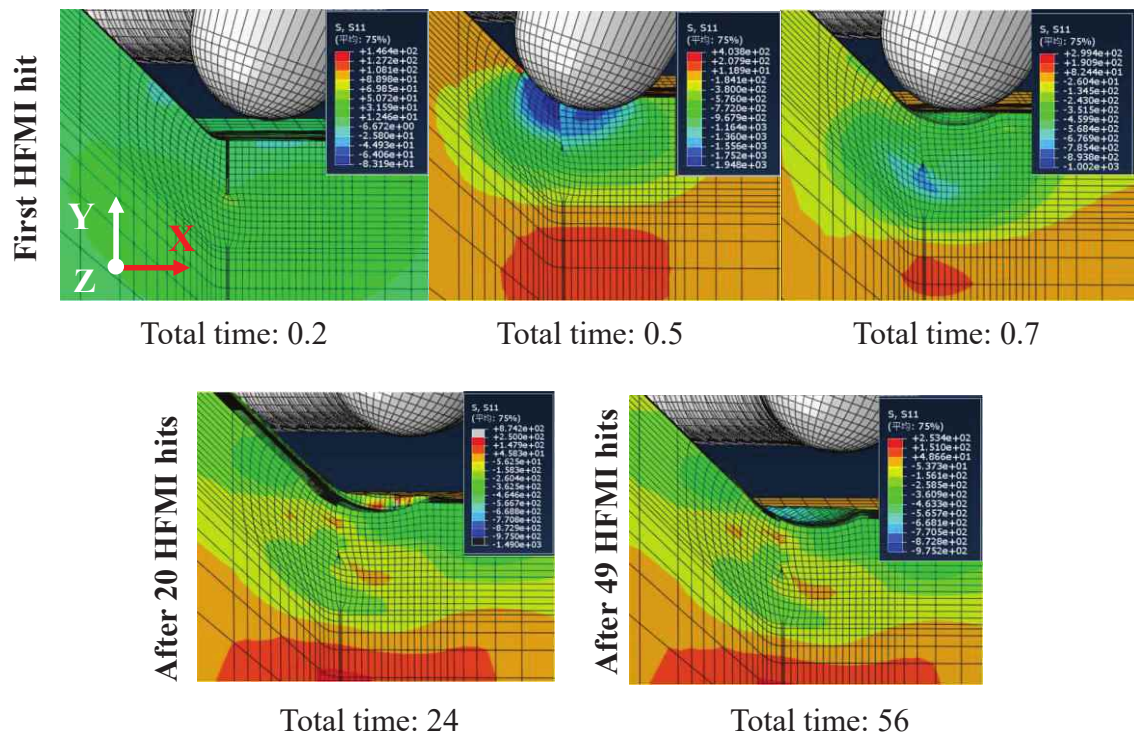
Figure 4-7 Induced compressive residual stress to the rat-hole model with and without slit

subsequent HFMI hits, as shown in total times 24 and 54. Similar trends can be seen from the residual stress distribution in the slit depth of 1.0 mm, see Fig. 4-8b. For the slit depth of 1.5 mm, the domain of compressive residual stress produced by HFMI treatment simulation is the same as those of slit depths of 0.5 and 1.0 mm. However, the amount of introduced compressive residual stress around the slit tip seems to be reduced, as shown in total time 0.7 in Fig. 4-8c. Induced compressive residual stress was influenced by subsequent HFMI hits and was partly relaxed, see total time 24. For the slit depth of 2.0 mm, although the domain of compressive residual stress produced by HFMI treatment simulation is the same as other results, introduction of compressive residual stress to the slit tip is prevented, and tensile residual stress are generated around the slit tip. This generated tensile residual stress was not turned into compressive residual stress even when subsequent HFMI hits were finished along the weld toe, see total time 24 and 56. Therefore, it can be concluded that the slit depth significantly affects introduced residual stress state especially for the slit tip, although the domain of HFMI produced compressive residual stress is almost the same.

Figure 4-7b shows the induced compressive residual stress along the slit face. The residual stress distributions were taken from the elements along the slit at the total time 56. Induced compressive residual stresses at the treated surface are about -250 to -300 MPa and are independent of the slit depths. Similar residual stress distributions can be observed up to a depth of 0.5 mm. For the depth up to 2.0 mm, compressive residual stress of approximately -100 MPa can be observed for the slit depth of 0.5 mm and 1.0 mm. On the other hand, a difference is observed in the compressive residual stresses for the slit depth of 1.5 mm and 2.0 mm. For the slit depth of 1.5 mm, tensile residual stresses are observed around the depths of 1.0 and 1.5 mm. For the slit depth of 2.0 mm, the magnitude of compressive residual stress is considerably reduced at a depth of 1.6 mm. This is the reason why HFMI treatment cannot close the slit when its depth is deeper as shown in Figs. 4-8c and 4-8d. Therefore, the magnitude of induced compressive residual stress around the slit tip is reduced when the slit depth is larger than 1.5 mm. Note that HFMI treatment simulation locally introduced compressive residual stress, e.g., the slit face near the HFMI treated welds and beneath the slit tip as shown in Fig. 4-8, although the introduction of compressive residual stress around the slit tip is prevented. This could be the reason why compressive residual stresses whose distributions are up and down up to 2.5 mm as shown in Fig. 4-7b.

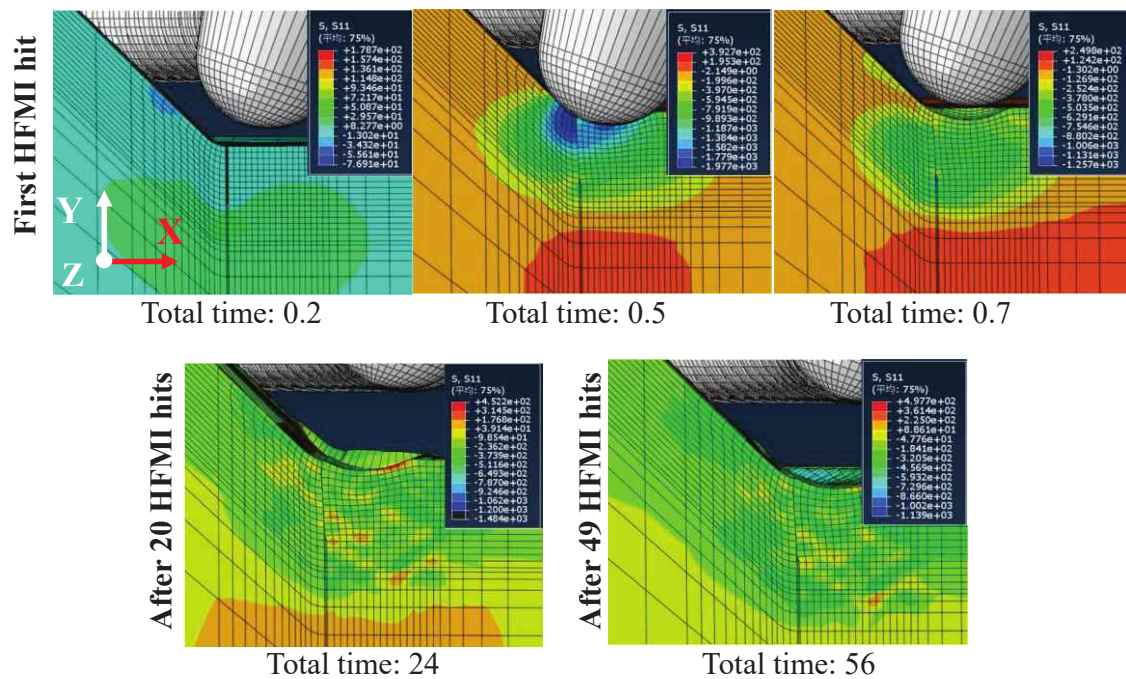


a Slit depth of 0.5 mm

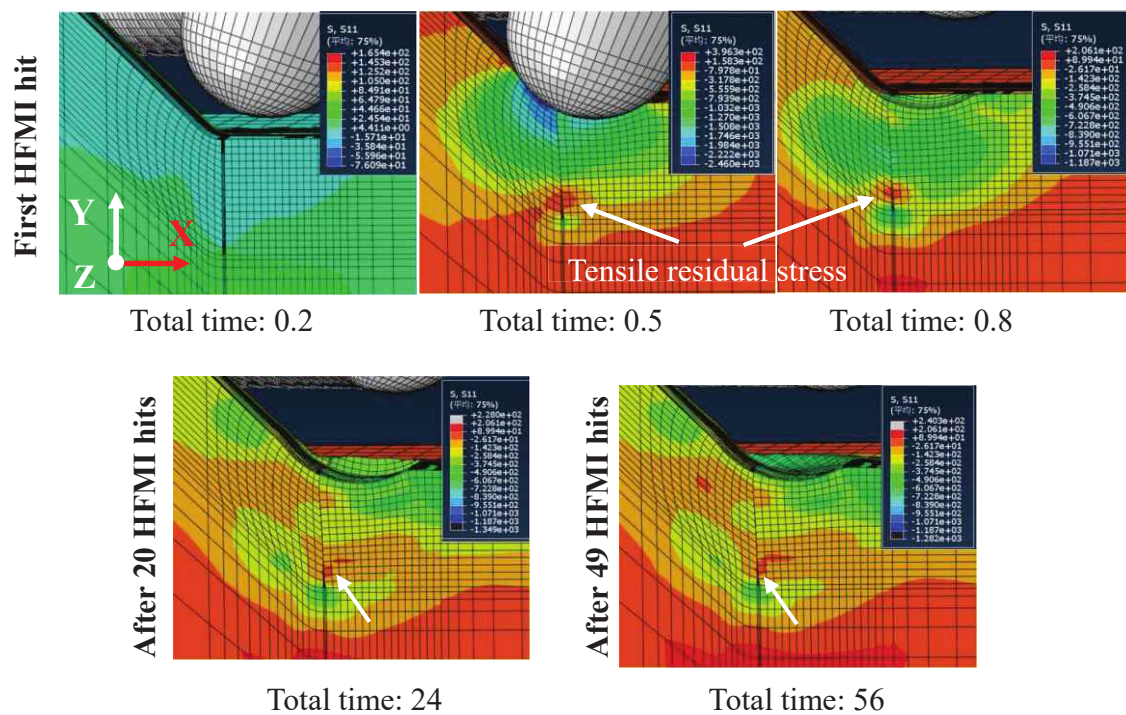


b Slit depth of 1.0 mm

Figure 4-8 Residual stress distribution during HFMI treatment simulation



c Slit depth of 1.5 mm

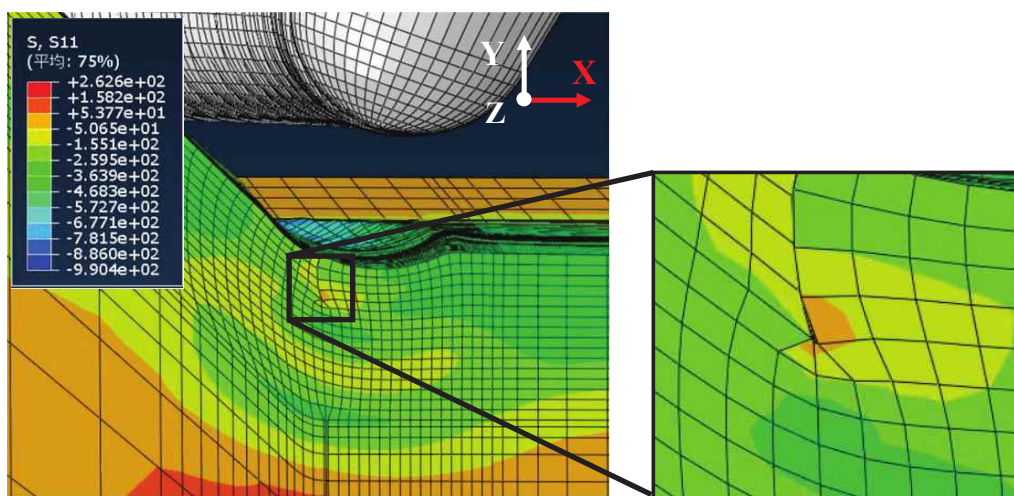


d Slit depth of 2.0 mm

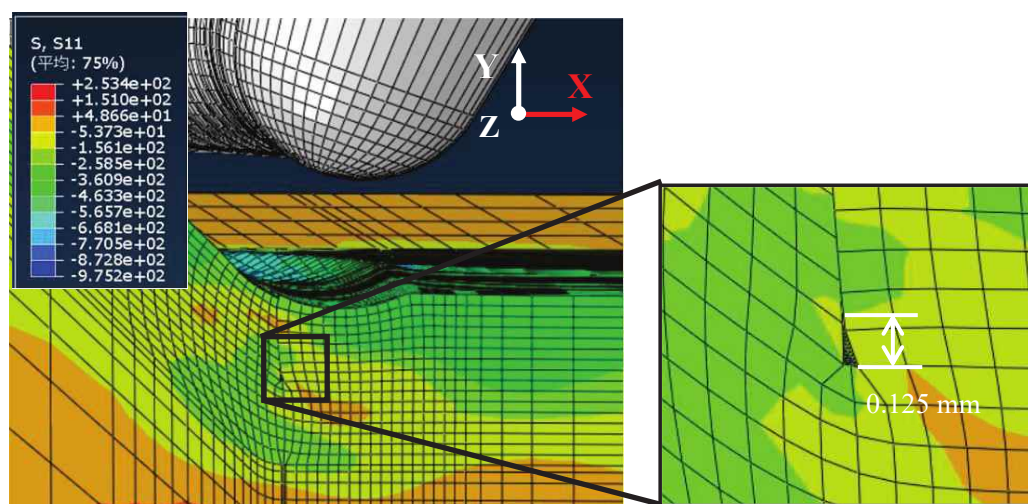
Figure 4-8 Residual stress distribution during HFMI treatment simulation (Continued)

4.4.2 Observation of change of slit geometry after HFMI simulation

Figure 4-9 shows the residual stress distribution when the slit geometry is changed. The results show that all slits around the treated surface are closed after HFMI treatment simulation. For the slit depth of 0.5 mm, the slit is entirely closed. When the slit depth is 1.0 mm, 0.125 mm of the slit remains open. This could be due to that the minimum mesh size of 0.125 mm used in the FE model. Similar size of remained open slit is observed for the slit depth of 1.5 mm. Hence, the HFMI treatment simulation tends to close the slit depth of less than 1.5 mm. On the other hand, a slit of 0.375 mm remains open in the case of the slit depth of 2.0 mm. This is due to that the magnitude of compressive residual stress is considerably reduced around the slit tip, see Figs. 4-7b and 4-8d. However, although tensile residual stresses are observed at 1.0 and 1.5 mm, the remained slit size of the result of 1.5 mm is smaller than that of the result of 2.0 mm. A possible explanation could be due to the intensity of HFMI treatment simulation, i.e., indentation depth of 0.2 mm. The indentation depth would influence the slit closure depth. This would require further investigation and simulations with other intensities/indentations depth, which is outside the scope of the current study. It can here be concluded that, HFMI treatment simulation can close a slit of less than 1.5 mm, by introducing high compressive residual stresses in the vicinity of the slit, under the condition of indentation depth of 0.2 mm which is in a qualitative agreement with the experimental result by Lefebvre et al. [9] where HFMI treatment was used as repair method and where fatigue cracks of 1.0 mm in depth could remain closed after the HFMI treatment.

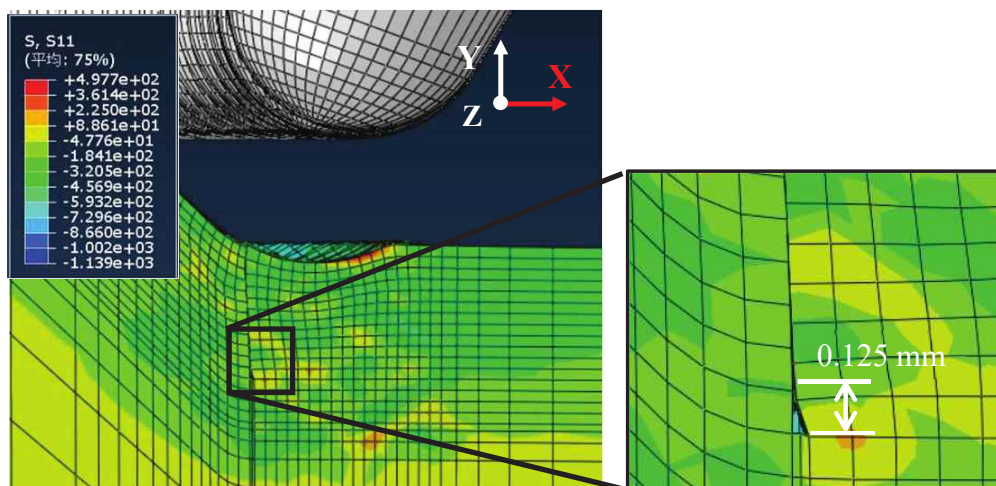


a Slit depth: 0.5 mm

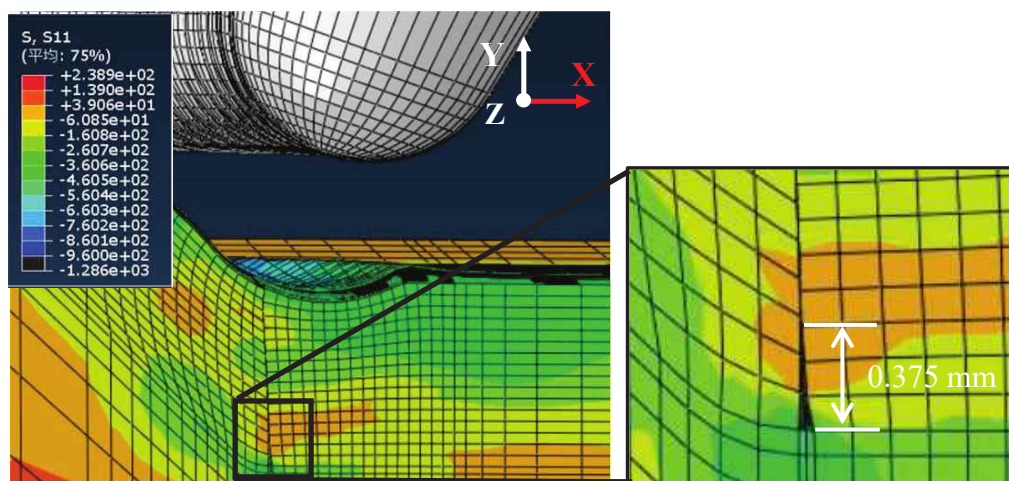


b Slit depth: 1.0 mm

Figure 4-9 Observation of change of slit after HFMI simulation



c Slit depth: 1.5mm

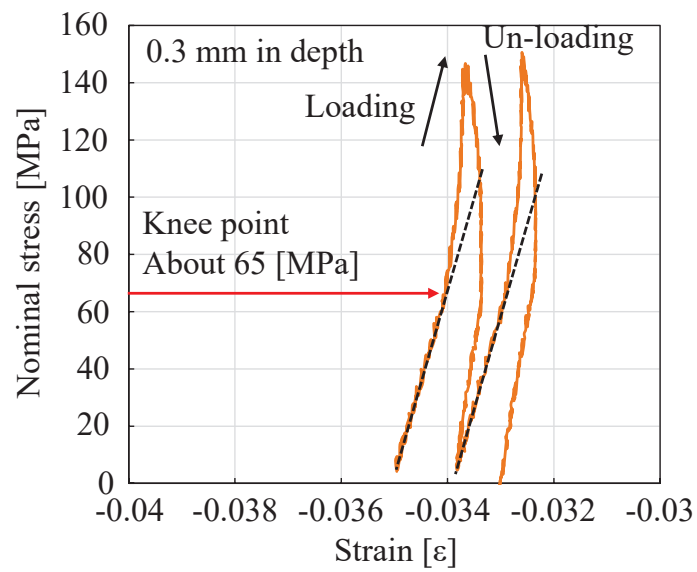
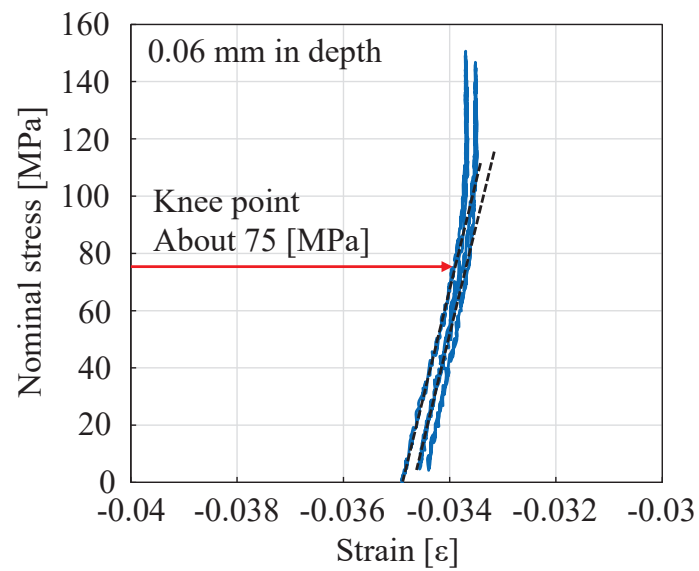
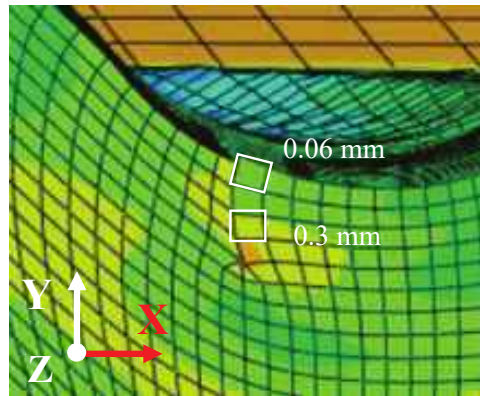


d Slit depth: 2.0 mm

Figure 4-9 Observation of change of slit after HFMI simulation (Continued)

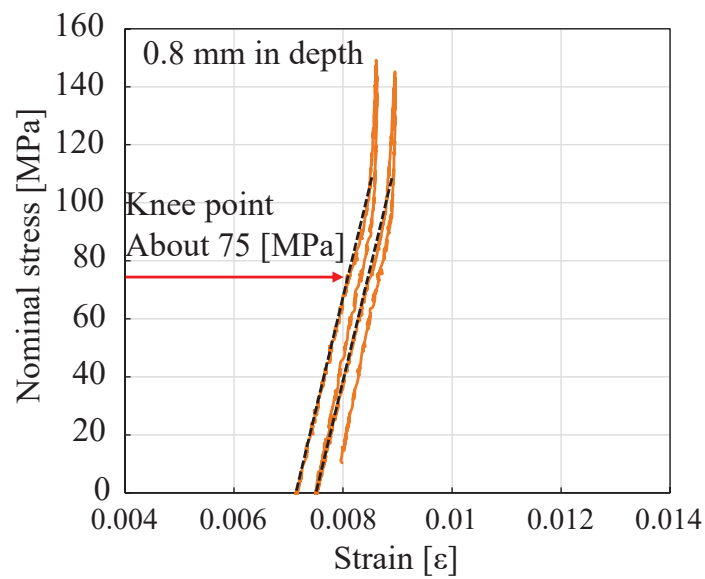
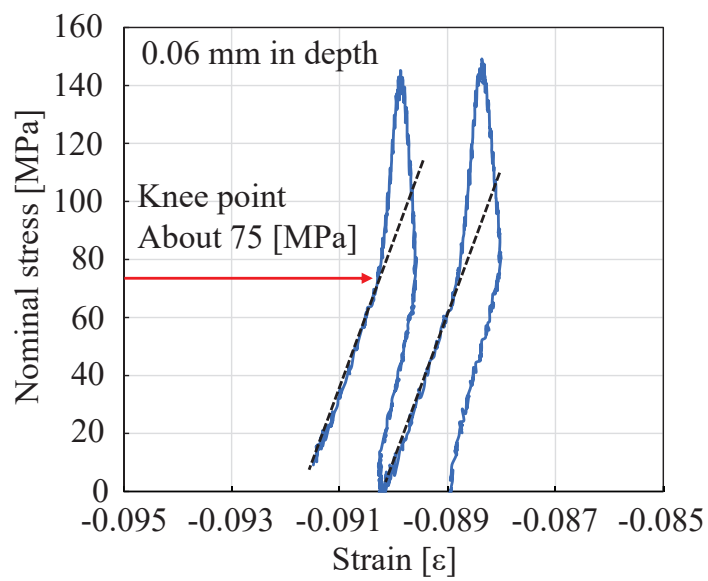
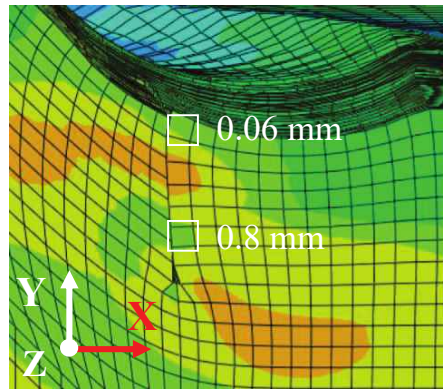
4.4.3 Observation of opening-closing behavior of HFMI treated slit

Figure 4-10 shows the opening-closing behavior of the HFMI treated slit. The opening-closing behavior of the HFMI treated slit was evaluated based on a change of strains from the centroid points along the slit face while the FE model is subjected to axial loading. The figures show nominal stress on the vertical axis versus strains on the horizontal axis. Figure 4-10a shows the result for the model with a slit depth of 0.5 mm. Stress-strain curves at 0.06- and 0.3 mm in depth are varied linearly first with increasing nominal stress. When the nominal stress gradually increases, the stress-strain curves show a nonlinear behavior. This is due to that the closed slit is opened and the axial loading is not transferred through the slit. The magnitude of nominal stress when this change occurs is defined as the slit opening stress. From the result of the slit depth of 0.5 mm, see Fig. 4-10a, the stress is about 75 MPa at the treated surface and 65 MPa at 0.03 mm in depth. From the result of a slit depth of 1.0 mm as shown in Fig. 4-10b, the stress is about 75 MPa. A variation of the slit opening stress is observed for the slit depths of 1.5 and 2.0 mm (see Figs. 4-10c and 4-10d). In the result of 1.5 mm, the stress is approximately 90 MPa at the treated surface whereas the one is 85, 75, and 50 MPa at 0.8-, 1.1-, and 1.3 mm in depth. The magnitude of the stress is decreased as the slit depth increases. This implies that the slit closed by HFMI treatment opens from its inside prior to its surface. Similarly, in the result of 2.0 mm, the same trend as the result of 1.5 mm is observed, where the stress is approximately from 80 to 100 MPa up to 1.0 mm in depth while the one is 40 MPa at 1.3 mm. At the 1.6 mm in depth (see Fig. 4-10d), the slit opening stress vanishes due to that the slit is not closed. It can be concluded that the closed slit by HFMI treatment opens from the inside, i.e., the bottom side of the closed slit opens prior to the HFMI treated surface.



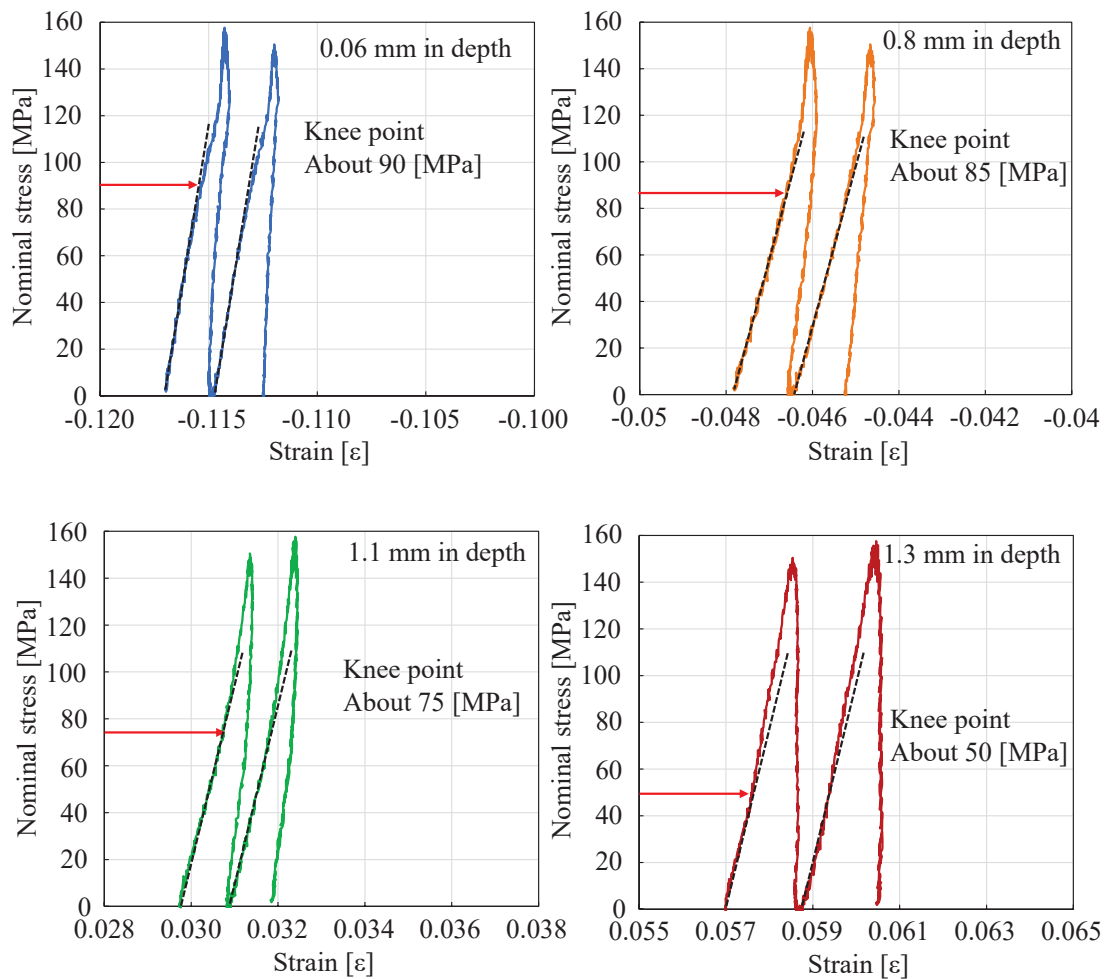
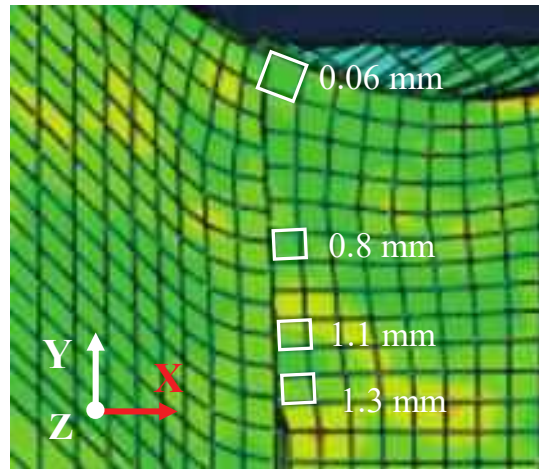
a Slit depth of 0.5 mm

Figure 4-10 Observation of opening-closing behavior of HFMI treated slit



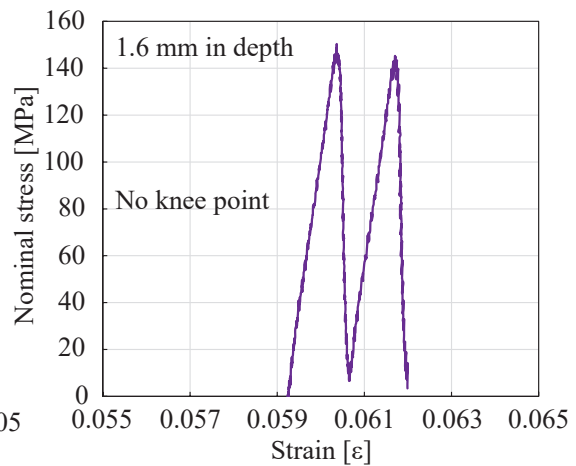
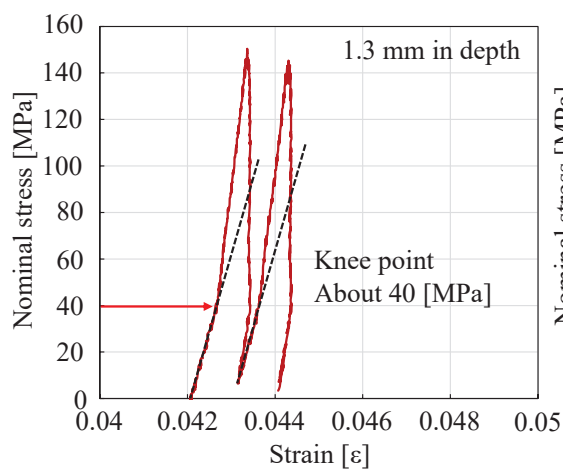
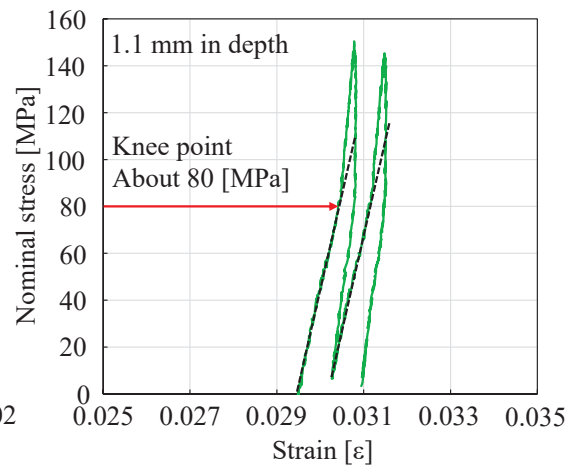
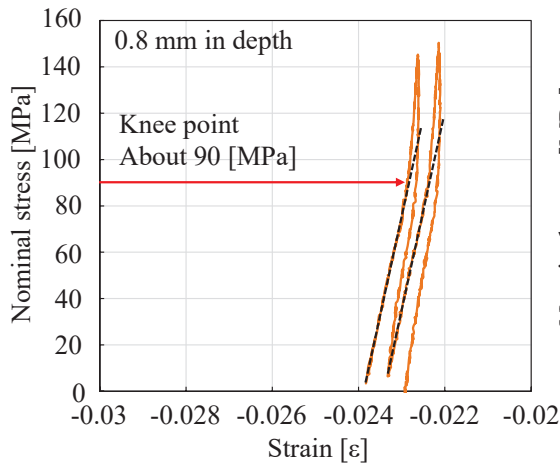
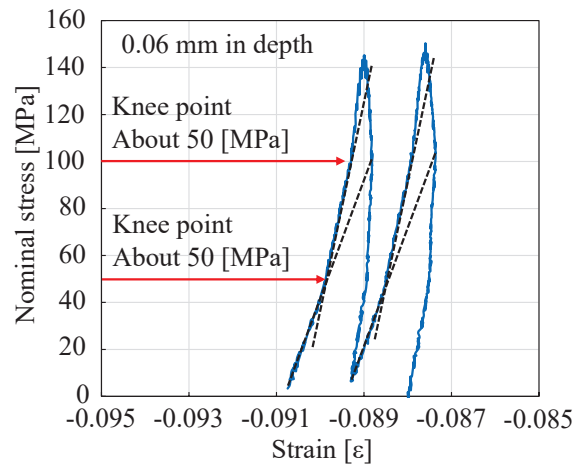
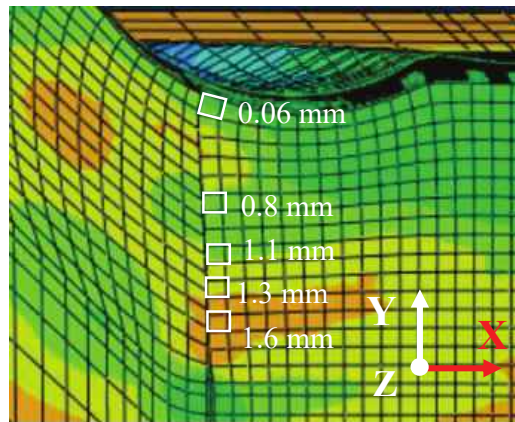
b Slit depth of 1.0 mm

Figure 4-10 Observation of opening-closing behavior of HFMI treated slit (Continued)



c Slit depth of 1.5 mm

Figure 4-10 Observation of opening-closing behavior of HFMI treated slit (Continued)



d Slit depth of 2.0 mm

Figure 4-10 Observation of opening-closing behavior of HFMI treated slit (Continued)

4.5 Experimental investigation of crack opening-closing behavior on pre-fatigued welded joint treated by hammer peening

4.5.1 Experimental procedure

Figure 4-11 shows the configuration of the out-of-plane gusset welded joint specimen. The specimen is made of Japan industrial standard SM490 grade steel with a plate thickness of 10 mm. Pre-fatigue test was carried out under axial constant loading and continued until fatigue cracks initiated at the weld toe and propagated to the edges of the seam weld. Thereafter, the specimens were treated with ICR treatment in order to repair/rehabilitate the specimen by closing the cracks.

The ICR treatment is a peening technique originally developed by Yamada et al. [21] in Japan. Figure 4-12 shows the ICR apparatus [21]. It has a rectangle indenter, and the tip is a flat surface of 4×5 mm with rounded corners. The apparatus impacts the base plate in transition to the fatigued weld toe. Due to the shape of the indenter, a large plastic deformation on the base plate can result into closing open cracks, which will result in large fatigue life enhancement [20]. The power source is compression air. The frequency during the impact is around 90 Hz. The ICR treatment was performed, with according to the previous study in [20, 23], to the pre-fatigued specimen.

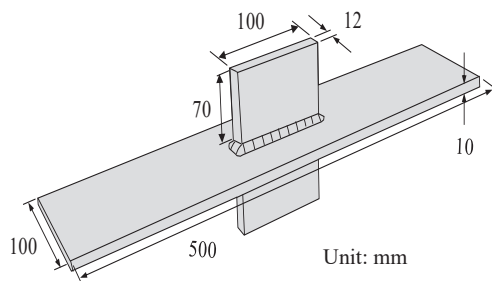


Figure 4-11 Out-of-plane gusset welded joints specimen



Figure 4-12 The ICR apparatus [21]

4.5.2 Non-destructive ultrasonic testing

Ultrasonic testing was carried out for the evaluation of fatigue crack opening-closing behavior. Miki et al. [101] investigated detectability of incomplete penetration in T-joints by using their developed tandem array transducer and found that crack tip opening can be observed by echo height from the crack tip and fatigue crack could be detected by comparing echo height for loading and unloading. A Phased Array Ultrasonic Testing (PAUT) system that is newly developed especially focusing on the non-

destructive evaluation for fatigue cracks in welds has demonstrated to be a reliable tool and its applicability was investigated and verified by several researchers [102, 103].

Kinoshita et al. [104] carried out an experimental investigation of crack opening-closing behavior on pre-fatigued welded joints treated by the ICR treatment and PPP by using the PAUT system and could identify the crack opening-closing behavior based on changing echo height ratio from the crack. Although the study by Kinoshita et al. [104] was conducted under bending loading, it is assumed that the PAUT system can detect and identify a fatigue crack opening-closing behavior under axial loading. The crack opening-closing behavior under axial loading was investigated using the PAUT system in this study.

Figure 4-13 shows the PAUT equipment made by OLMPAS Co. Ltd used in this study. The transducer has a linear array consisting of 16 channels with an operating frequency of 5.0 MHz. Sector scan was used for incident of ultrasonic wave. Thereby, the incident wave angles within 40~70 degrees can be swept without moving the transducer. Figure 4-14 shows detection methods and locations of crack tip attempting detection by

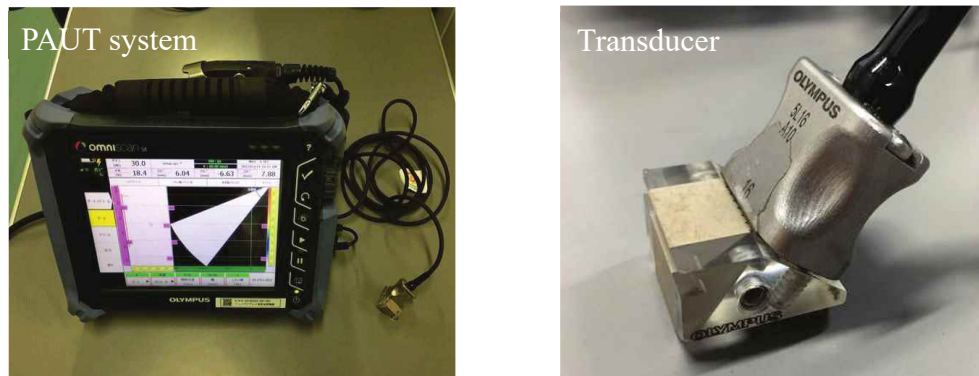


Figure 4-13 The PAUT equipment

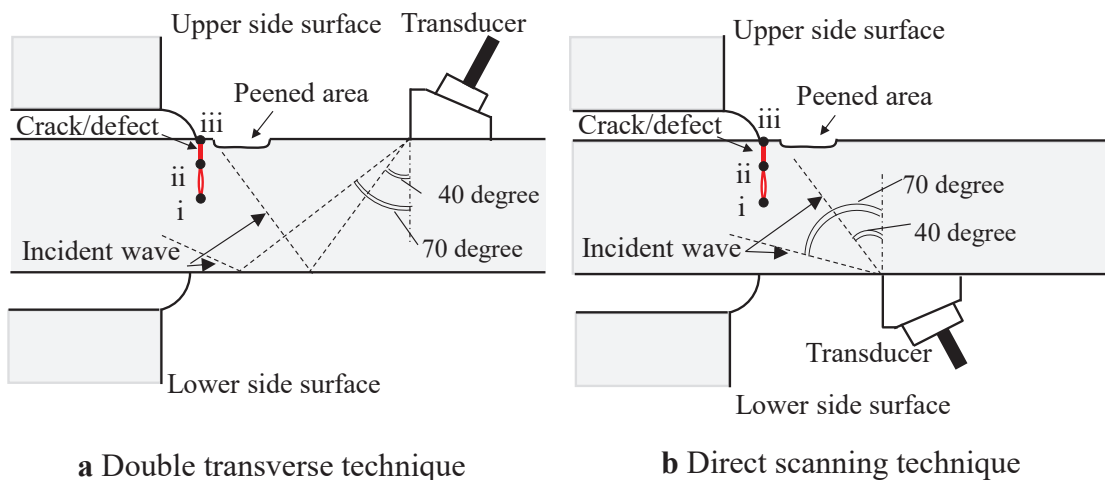


Figure 4-14 Detection methods and locations of cracks

using the PAUT system. For the locations of the crack tip, three locations were aimed: (i) the crack tip, (ii) the closed crack on the bottom side, and (iii) the closed crack on the treated surface. First, the treated surface was defined as the upper side surface, and the opposite was the lower side surface. Then, the transducer was put on both surfaces to measure echo height from every crack tip. On the measurement from the upper side, double transverse technique was adopted (see Fig. 4-14a), while on the opposite side, direct scanning technique was adopted (see Fig. 4-14b). The measurement of echo height using the PAUT system was conducted with axial loading up to a maximum nominal stress of 100 MPa with incremental increase of 10 MPa.

4.5.3 Experimental investigation result

Figure 4-15 shows the fractured surface. A semi-elliptical crack with a width of 18.5 mm and a depth of 6.0 mm was identified on the surface. Moreover, a portion on the surface has metallic luster. That is because fatigue crack faces were pressed by plastic deformation of the treated base plate due to the ICR treatment. The depth of the luster was 2.0 mm, i.e., it can be said that the fatigue crack of at least 2.0 mm in depth was closed by the ICR treatment and the remained crack of about 4.0 mm was left open. This is in agreement with previous experimental investigation, where fatigue cracks with a depth of 1.0 mm remained closed after the ICR treatment and subsequent loading [105].

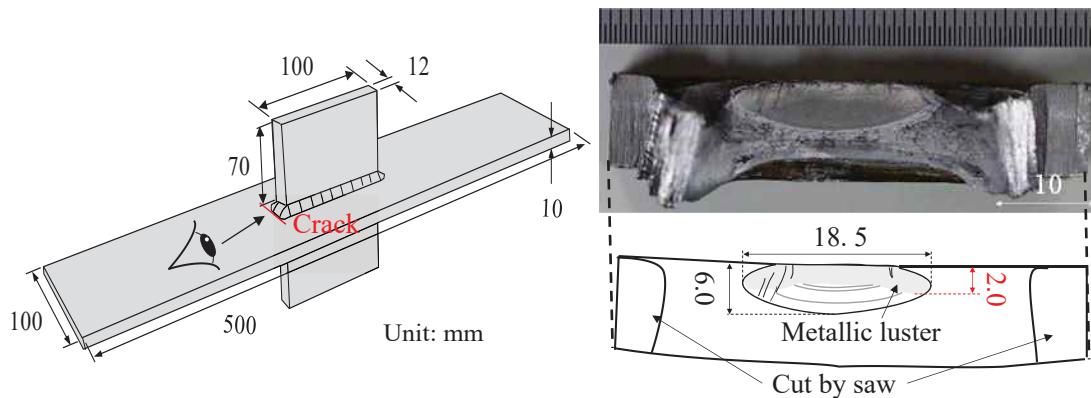
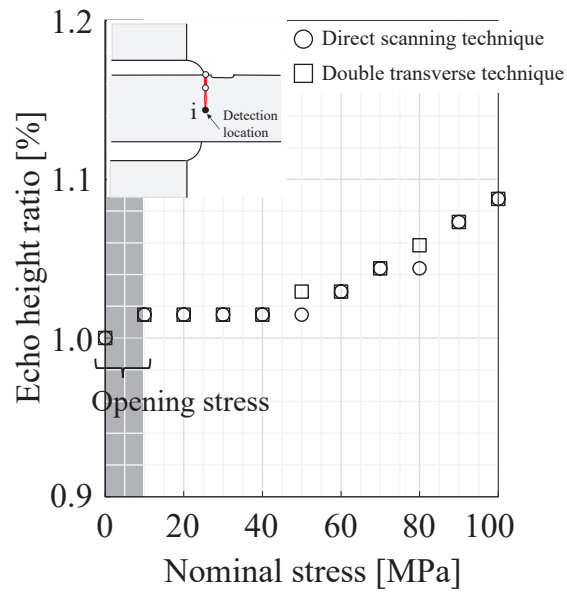


Figure 4-15 Observation of the fractured surface [Unit: mm]

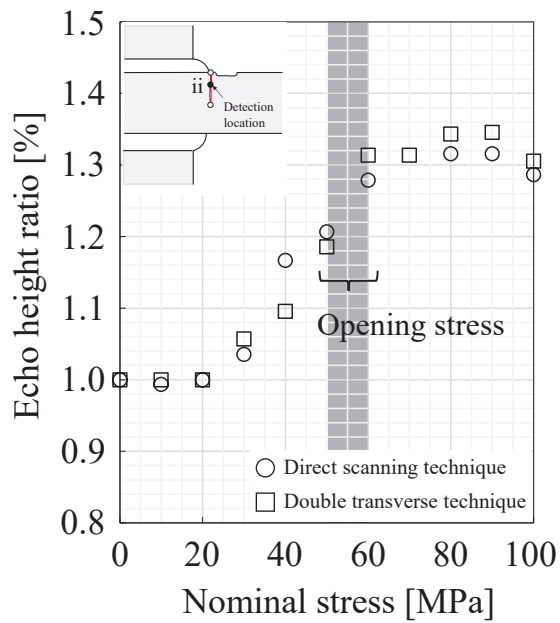
Figure 4-16 shows the relationship between echo height ratio and nominal stress range. The echo height ratio was calculated by dividing echo height at each nominal stress by initial echo height at zero stress. In Figure 4-16, the results of two types of detection methods are depicted. The previous studies [101, 104] observed that no change of echo height ratio occurs when an applied load is small, and the change starts when the applied load is gradually increased, and then it becomes stable when the applied load is large enough. This is mainly due to that the amount of reflection echo is small as incident echo

can pass through a closed crack, while, when crack opening starts, the amount of the reflection echo is drastically increased as the incident echo is prevented from passing due to a gap by crack opening [101]. Hence, focusing on a change of echo height ratio can identify the nominal stress level for crack opening.

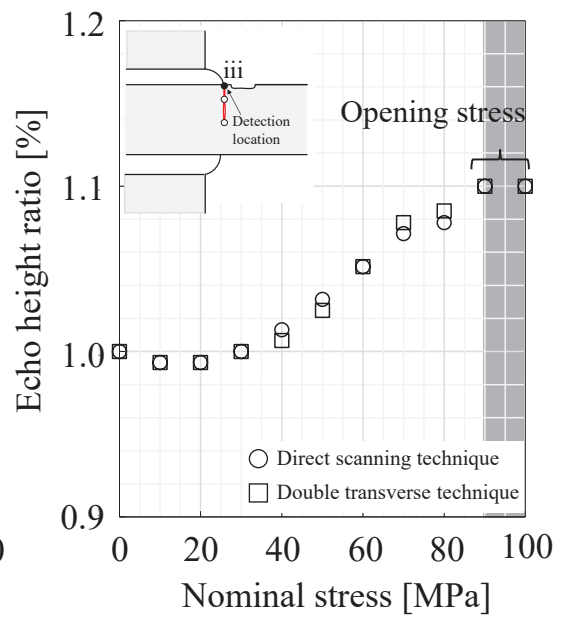
From the result of the crack tip, see Fig. 4-16a, an increment of echo height ratio is observed at 10 MPa in nominal stress, and then the change of the ratio becomes stable, which is caused by the crack opening. From the result of the closed crack on the bottom side, see Fig. 4-16b, the increment of the echo height ratio due to crack opening starts at the nominal stress of 20 MPa, and then the increment is stable around 60 MPa in nominal stress. The closed crack on the bottom side seems to be completely opened between nominal stresses of 50 to 60 MPa. From the result of the closed crack on the treated surface, see Fig. 4-16c, the echo height ratio increases at 40 MPa and the ratio becomes constant at a nominal stress of 90 MPa and it can be confirmed that the closed crack on the treated surface is opened at a nominal stress of 90 MPa. The increment of the echo height ratio of the crack tip starts at a nominal stress of 40 MPa, at the same time the increment of the echo height ratio of the closed crack on the treated surface is observed. Accordingly, the increment of the crack tip can be explained due to crack opening on the treated surface. The nominal stresses that each crack is completely opened are, approximately 10 MPa on the crack tip, approximately 50 to 60 MPa on the closed crack on the bottom side, and approximately 90 MPa on the closed crack on the treated surface. The magnitude of the nominal stress is increased in the order of (i), (ii), and (iii). Hence, it can be observed that the closed crack is opened from its inside prior to the treated surface. This crack opening order is similar to the FE HFMI simulations of the rat-hole specimen, presented in this study. Accordingly, the crack opening behavior of pre-fatigued welded joints treated by ICR treated welds can be identified experimentally using the PAUT system.



a (i) The crack tip



b (ii) The crack on the treated bottom side



c (iii) The crack on the treated surface

Figure 4-16 The relationship between echo height ratio and nominal stress

4.6 Conclusions

The objective in this chapter is to understand the effect of HFMI treatment on pre-fatigued welds and crack opening-closing behavior in HFMI treated welds. Numerical investigations with the aid of FE HFMI simulation were carried out on the rat-hole models inserting a rectangle slit with different depths in their welds. In addition, the crack opening-closing behavior on pre-fatigued out-of-plane gusset welded joint treated by the ICR treatment was investigated experimentally using the PAUT system. The main findings of this study are summarized as follows:

1. The initial welding residual stress was introduced along the weld toe by elastic thermal analysis, which is an alternative and simplified approach compared to full computational welding simulation. The analysis results show that the initial welding residual stress has a minor effect on the final residual stress state after HFMI simulation.
2. HFMI simulations were carried out on the rat-hole models inserting rectangle slit with different depths. The results show that the magnitude of the induced compressive residual stress around the slit tip is reduced when the slit depth becomes larger, resulting in that the slit remained partly open. In this study, HFMI simulation with indentation depth of 0.2 mm was carried out inserting 2.0 mm slit depth, resulting in an opened remain slit of about 0.4 mm. Hence, HFMI treatment can close fatigue cracks less than 1.5 mm in depth.
3. After the HFMI simulation, opening-closing behavior of the HFMI treated slit was observed based on a change of strains along the slit face while applying axial loading. The results show that the slit is opened from the bottom side prior to the treated surface.
4. In addition, the crack opening-closing behavior was investigated experimentally using pre-fatigued out-of-plane gusset welded joints treated by the ICR treatment with the aid of the PAUT system. The behavior can be identified based on the change of echo height ratio from the crack. It is also observed that the crack is opened at the crack tip, closed crack on the bottom side, and closed crack on the treated side. Similar crack opening-closing behavior could be observed in the FE simulations.
5. From the numerical and experimental investigations, the behavior would be summarized as shown in Fig. 4-17.

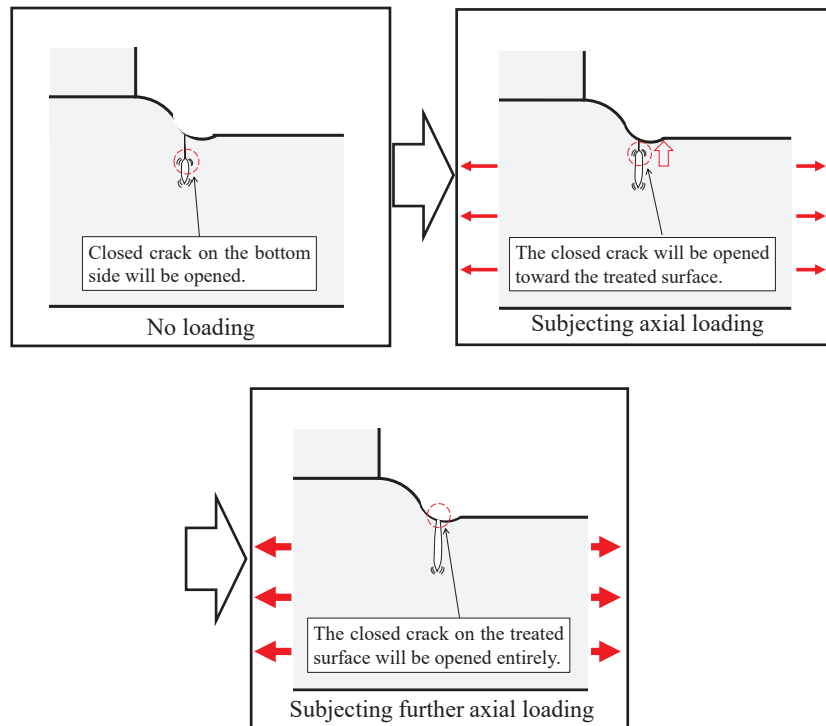


Fig. 4-17 Identified crack opening-closing behavior on pre-fatigue welded joints treated by HFMI

Chapter 5

Life extension analysis considering crack opening-closing behavior in HFMI treated welds

5.1 Introduction

The objective of this chapter is to investigate defect tolerance of HFMI treated welds in bridge application for life extension. The rat-hole models with different fatigue crack depths in the HFMI treated welds were used in 3D Crack Propagation Analysis (CPA) based on Linear Elastic Fracture Mechanics (LEFM). At first, compressive residual stresses introduced by HFMI treatment simulation were considered over those cracks faces in the HFMI treated welds. Crack opening stress at the crack tip in HFMI treated weld was investigated considering the crack opening-closing behavior studied in **Chapter 4**. Then, the 3D CPA based on LEFM was carried out under fatigue load, and crack propagation behavior was studied. Finally, the fatigue life was calculated based on the 3D CPA results, and the defect tolerance of the HFMI treated welds in bridge application for life extension was investigated. Those investigations were made using the commercial software Franc3D [106].

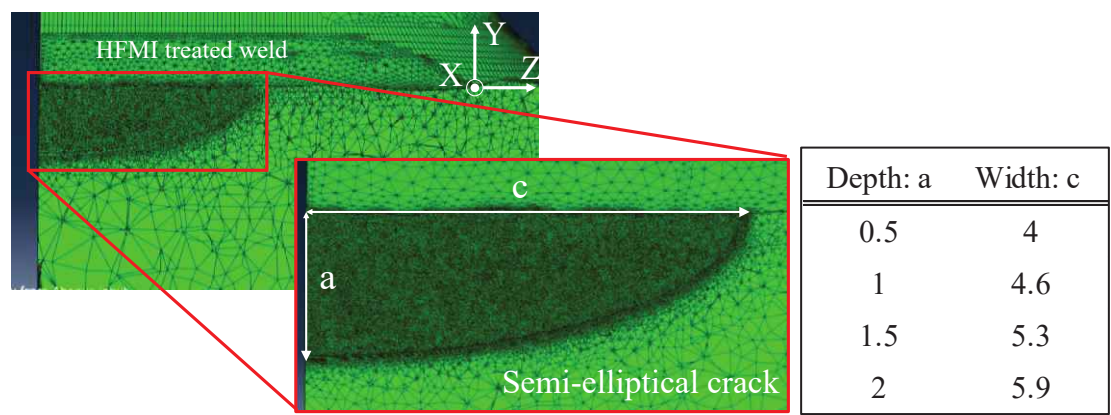
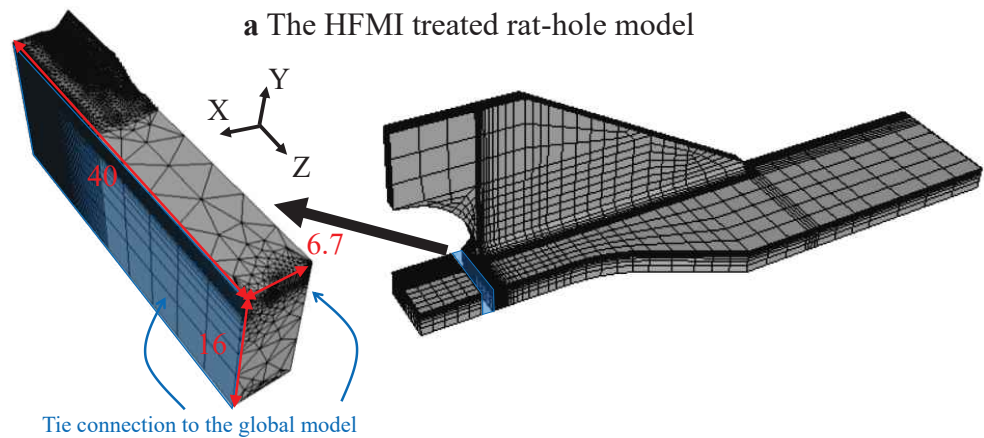
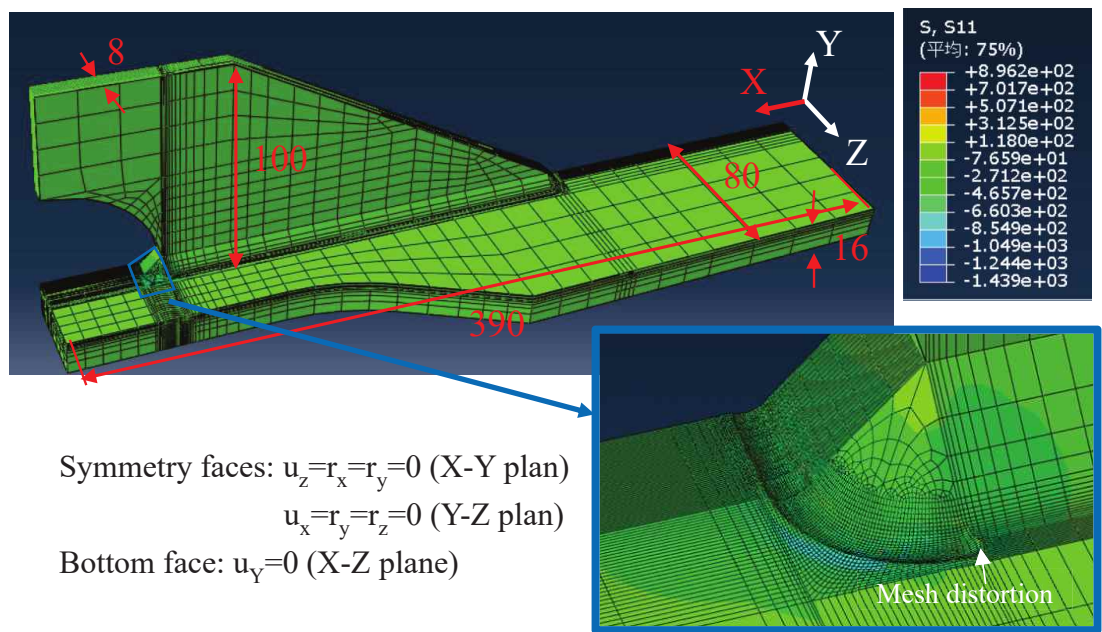
5.2 Simulation model

5.2.1 The rat-hole model

Figure 5-1 shows the quarter rat-hole model used in the CPA. For each symmetry face of the rat-hole model, boundary conditions were defined: $u_z=r_x=r_y=0$ for the X-Y plane and $u_x=r_y=r_z=0$ for the Y-Z plane. For the bottom face (the X-Z plane), $u_y=0$ was defined since initial cyclic loading was applied to the X-direction after HFMI treatment simulation. In order to insert fatigue crack into a HFMI treated weld, the rat-hole model was treated by HFMI treatment simulation under the same manner as **section 4.3.1**. The HFMI simulation was carried out in Abaqus with explicit solver. The HFMI simulation results in indentation depth of 0.2 mm, see Fig. 5-1a. This HFMI treated rat-hole model was used for subsequent CPA.

The HFMI treated rat-hole model was imported into Franc3D in order to insert fatigue crack in the HFMI treated weld. Fig. 5-1b shows the rat-hole model imported into Franc3D. Franc3D allows to divide FE simulation model into global and local models for the sake of reducing simulation time. Therefore, the rat-hole model was divided into global and local models, see Fig. 5-1b. The local model was chosen as a small portion of the rat-hole model. Since HFMI treatment simulation made mesh distortion at the weld seam edge, subsequent fatigue crack insertion failed when the local model included the edge, see Fig. 5-1a. Although the small portion of the rat-hole model was chosen as the local model, transition of the mesh size on the global and local models was enough smooth, and hence, the size of the local model would not affect CPA result. The global and local models were connected using tie connection. An elastic modulus. $E=2.0 \times 10^6$

MPa and poisson's ratio $\nu=0.3$ were used in the global and local models.



c Inserted fatigue crack

Figure 5-1 The rat-hole model used in CPA [Unit: mm]

5.2.2 Modeling of fatigue crack

Semi-elliptical fatigue cracks with different depths were inserted into the HFMI treated welds of the local models, as shown in Fig. 5-1c. The fatigue crack depths were 0.5-, 1.0- 1.5- and 2.0 mm, and those widths were determined as the same manner in **Section 4.3.1**, see table in Fig. 5-1c. The local coordinates of inserted fatigue cracks corresponded with those of the HFMI treated slit studied in **Chapter 4**. Although the kink angle of the slit was slightly changed after the HFMI treatment simulation, this change was not considered when the fatigue cracks were inserted into the HFMI treated welds.

After the fatigue cracks were inserted, the local model was automatically re-meshed by Franc3D, see Fig 5-1c. The crack front was re-meshed using 15-nodes wedge elements surrounded by 20-nodes brick elements, as shown in Fig. 5-2. These elements have appropriate side-nodes moved to the quarter points, which allows the element to reproduce the theoretical $1/\sqrt{r}$ stress distribution around the crack tip. The mesh topology around the crack front in Franc3D is illustrated in Fig. 5-3. The number of elements in the radius direction is called template radius. The template radius is defined as the distance that the tubular mesh topology surrounds the crack front. The number of elements in the circumferential direction and the number of rings in the radius direction

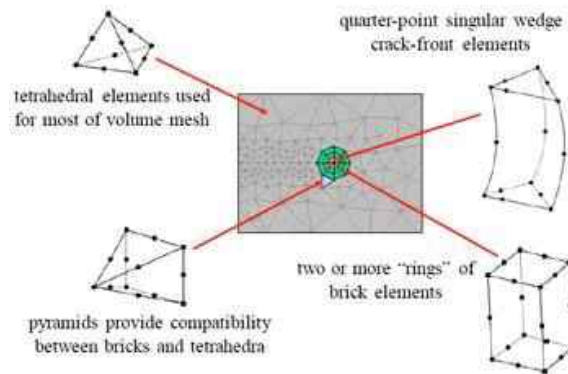


Figure 5-2 Element types used to the mesh around the crack front [107]

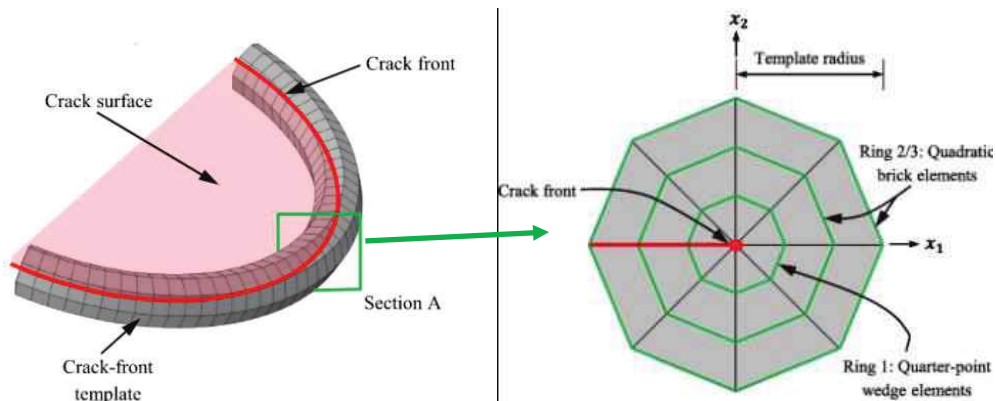


Figure 5-3 Crack front template found in [108]

can be adjusted as crack front template parameters, and they can be manually defined and extruded along the crack front meshing, as shown in Fig. 5-3.

5.2.3 Compressive residual stress

In order to consider compressive residual stresses subjected over the crack face, compressive residual stress distributions obtained from the rat-hole models with different slit depths studied in **Chapter 4** were used. Figure 5-4 shows compressive residual stress distributions obtained from the rat-hole models with different slit depths. In this figure, those distributions after once and twice initial cyclic loadings are subjected, where maximum and minimum nominal stresses are around 150 and 0 MPa, are also shown, see dot lines in Fig. 5-4. Because residual stress redistribution and/or relaxation would occur within a few initial cyclic loadings, as observed in the experimental studies [109, 110]. From the figure, although compressive residual stresses were slightly relaxed after the first cyclic loading from those as HFMI, residual stress relaxation/redistribution after the second initial cyclic loading was quite minor. Hence, it would be assumed that further residual stress distribution/relaxation does not occur in this magnitude of applied nominal stress. Thus, compressive residual stresses distributions after the second initial cyclic loading was subjected to the model were incorporated into the local models with different crack depths.

Franc3D allows a FE simulation model to incorporate residual stress distribution using a function, so-called Crack Face Traction (CFT) [106]. Hence, taken residual stress distributions were incorporated into the local models with different crack depths using CFT. Figure 5-5 shows a schematic diagram when CFT is used for the local model with crack depth of 2.0 mm. The incorporated residual stress distribution works as a boundary condition of the local model and is uniformly distributed over the crack face. Residual stress distributions taken from the elements along the slit at the center of the rat-hole model was used as a representative value. This is because the inserted crack depth and the slit depth are identical to the center of the local model. Each residual stress distribution obtained from the models with different slit depths was set to the local models with corresponded crack depths. Note that the values of compressive residual stress were incorporated into the model as tabular form, and those values are not varied, i.e., redistribution/relaxation of them due to fatigue crack propagation was not considered in Franc3D [106].

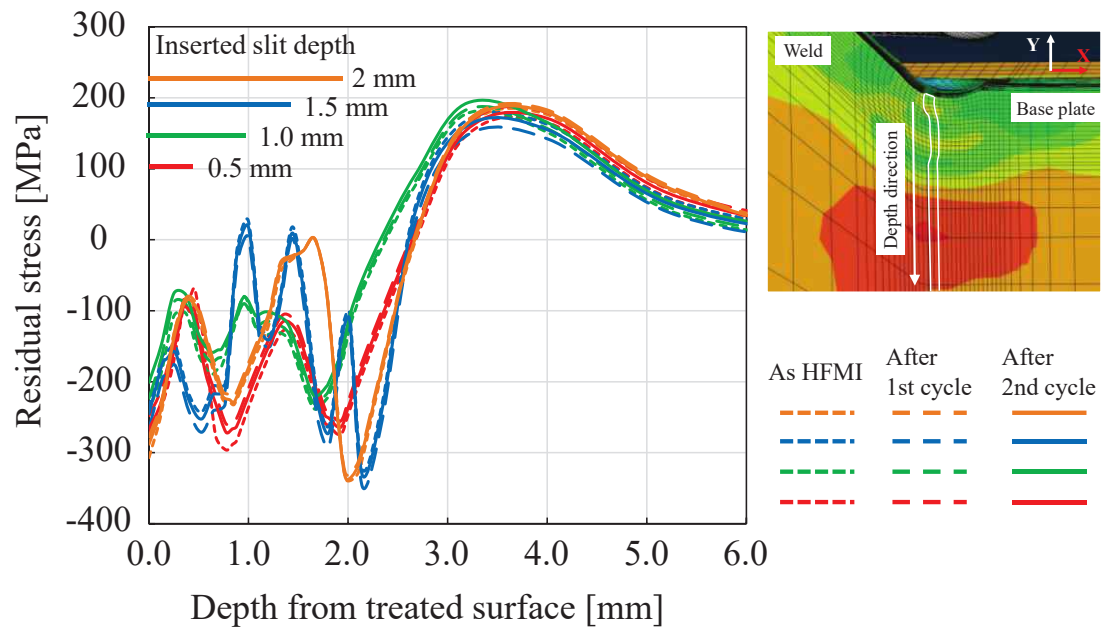


Figure 5-4 Compressive residual stress distributions obtained from the model with different slit depths

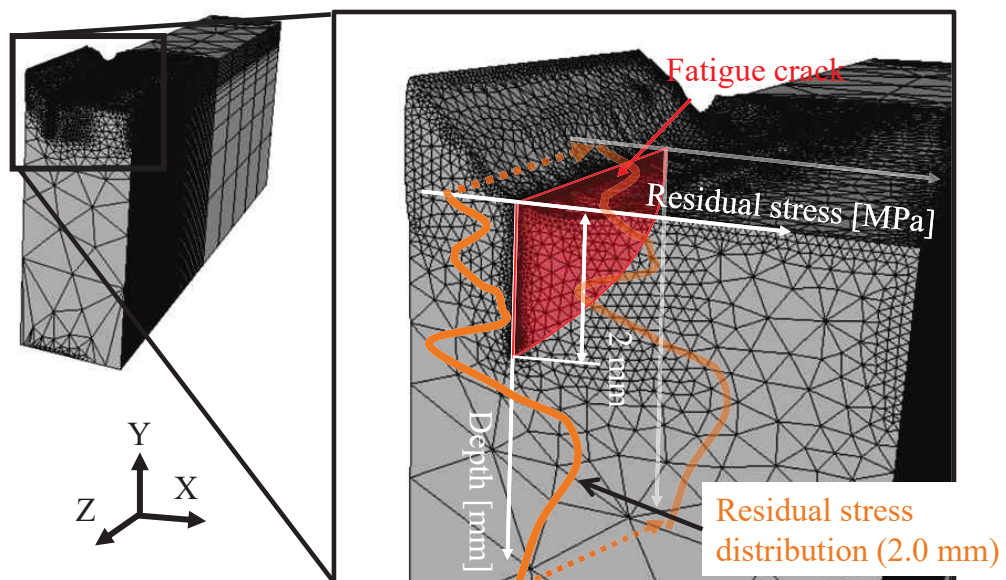


Figure 5-5 Schematic diagram when CFT is used to the local model with crack depth of 2.0 mm

5.3 Linear elastic fracture mechanics

5.3.1 M-integral for stress intensity factor determination

Stress Intensity Factor (SIF) is used in fracture mechanics to predict the stress state near the crack tip and would be very useful to evaluate whether cracks propagate. Several methods are available for calculating the SIFs [111-114]. In this study, M-integral method [114] implemented in Fracn3D was employed to quantify SIF value because of its high accuracy [114, 115]. M-integral was developed from J-integral by Yan et al. [114] in order to calculate the three modes of SIFs for an isotropic and anisotropic materials. Hereafter, the formulation of M-integral is present.

M-integral is derived from J-integral. J-integral measures the energy flow into the crack tip region shown in Fig. 5-6, as denoted by Eqs. (5-1) and (5-2).

$$\bar{J} = \int_{\Gamma} \left(\sigma_{ij} \frac{\partial u_i}{\partial x_1} - W \delta_{1j} \right) \frac{\partial q}{\partial x_j} ds \quad (\text{Eq.5-1})$$

$$W = \frac{1}{2} \sigma_{ij} \varepsilon_{ij} \quad (\text{Eq.5-2})$$

where, Γ is a counterclockwise closed contour around the crack tip, W is a strain energy density of a material, σ_{ij} is the stress tensor, ε_{ij} is the strain tensor, u_i is the displacement tensor, ds is the increment of arc length, x is the position of vector of the integration points, δ_{1j} is the crack tip opening displacement and q is a function from the crack tip to zero on the boundary of the integration domain. \mathbf{n} shown in Fig. 5-6 is the outward unit vector normal to Γ .

In 3D volume, J-integral is evaluated within a cylindrical domain centered on a portion of the crack front shown in Fig. 5-7, denoted by Eq. (5-3).

$$J = \frac{\int J(S) q_t(S) ds}{\int q_t(S) ds} = \frac{\bar{J}}{A_q} \quad (\text{Eq.5-3})$$

For linear elastic material, the principle of superposition is hold. Therefore, arbitrary stress, strain, and displacement tensor and SIFs can be superimposed, see Eqs. (5-4) and (5-5).

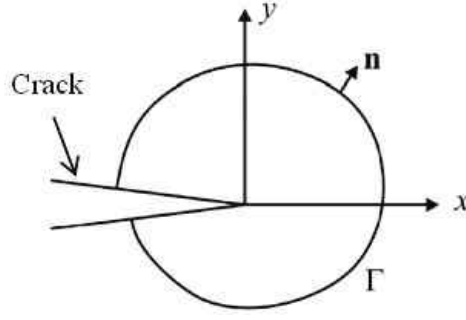


Figure 5-6 J-integral loop at the crack tip [107]

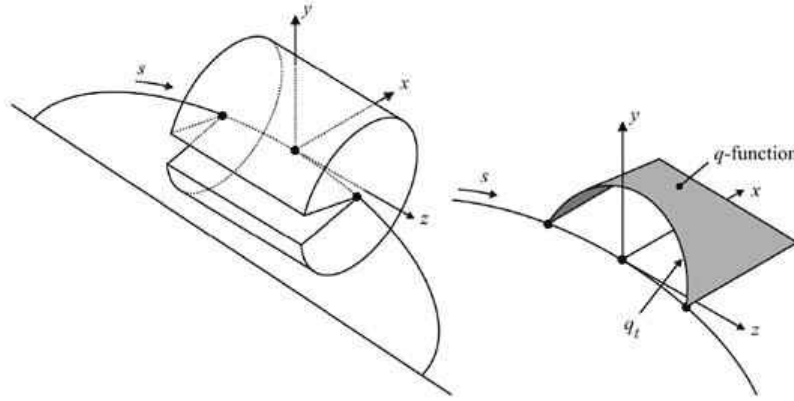


Figure 5-7 J-integral loop at the crack front in 3D volume [107]

$$\sigma_{ij} = \sigma_{ij}^{(1)} + \sigma_{ij}^{(2)} \quad \varepsilon_{ij} = \varepsilon_{ij}^{(1)} + \varepsilon_{ij}^{(2)} \quad u_{ij} = u_{ij}^{(1)} + u_{ij}^{(2)} \quad \text{Eq.(5-4)}$$

$$K_I = K_I^{(1)} + K_I^{(2)} \quad K_{II} = K_{II}^{(1)} + K_{II}^{(2)} \quad K_{III} = K_{III}^{(1)} + K_{III}^{(2)} \quad \text{Eq.(5-5)}$$

where, superscript (1) is the FE simulation results, and superscript (2) is the auxiliary fields that are selected from the analytical expressions for the crack front field. Eq. (5-4) is substituted into the expression of J-integral shown in Eq. (5-1). J-integral can be described as Eq. (5-6).

$$\bar{J} = \bar{J}^{(1)} + \bar{J}^{(2)} + \bar{M}^{(1,2)} \quad \text{Eq.(5-6)}$$

Where, $\bar{M}^{(1,2)}$ is M-integral shown in Eq. (5-7).

$$\bar{M}^{(1,2)} = \int_{\Gamma} \left(\sigma_{ij}^{(1)} \frac{\partial u_i^{(2)}}{\partial x_1} + \sigma_{ij}^{(2)} \frac{\partial u_i^{(1)}}{\partial x_1} - W^{(1,2)} \delta_{1j} \right) \frac{\partial q}{\partial x_j} ds \quad \text{Eq.(5-7)}$$

On the other hand, under the small scale yielding condition, the J-integral is identical to the energy release rate, G [83], expressed by Eq. (5-8)

$$G = J = \frac{1 - \nu^2}{E} K_I^2 + \frac{1 - \nu^2}{E} K_{II}^2 + \frac{1 + \nu}{E} K_{III}^2 \quad \text{Eq.(5-8)}$$

Substituting Eq. (5-5) into Eq. (5-8) and rearranging the equation, J-integral can be derived as Eqs. (5-9) and (5-10).

$$J = J^{(1)} + J^{(2)} + M^{(1,2)} \quad \text{Eq.(5-9)}$$

where,

$$M^{(1,2)} = \frac{1 - \nu^2}{E} K_I^{(1)} K_I^{(2)} + \frac{1 - \nu^2}{E} K_{II}^{(1)} K_{II}^{(2)} + \frac{1 + \nu}{E} K_{III}^{(1)} K_{III}^{(2)} \quad \text{Eq.(5-10)}$$

Substituting Eqs. (5-6) and (5-9) into Eq. (5-3) and solving the equation in terms of M-integral, Eq. (5-11) can be lead.

$$\bar{M}^{(1,2)} / A_q = \frac{2(1 - \nu^2)}{E} K_I^{(1)} K_I^{(2)} + \frac{2(1 - \nu^2)}{E} K_{II}^{(1)} K_{II}^{(2)} + \frac{2(1 + \nu)}{E} K_{III}^{(1)} K_{III}^{(2)} \quad \text{(Eq.5-11)}$$

The auxiliary fields states are then defined such that one solution is obtained for each pure mode using three simple auxiliary solutions, such as 2a, 2b, and 2c, see Eqs. (5-12), (5-13), (5-14) and (5-15).

$$K_I^{(1)} = \frac{E}{2(1 - \nu^2)} \cdot \frac{\bar{M}^{(1,2a)}}{A_q} \quad \text{(Eq.5-12)}$$

$$K_{II}^{(1)} = \frac{E}{2(1 - \nu^2)} \cdot \frac{\bar{M}^{(1,2b)}}{A_q} \quad \text{(Eq.5-13)}$$

$$K_{III}^{(1)} = \frac{E}{2(1 + \nu)} \cdot \frac{\bar{M}^{(1,2c)}}{A_q} \quad \text{(Eq.5-14)}$$

$$(K_I^{(2)}, K_{II}^{(2)}, K_{III}^{(2)}) = \begin{cases} (1,0,0) \text{ Pure Mode I} \\ (0,1,0) \text{ Pure Mode II} \\ (0,0,1) \text{ Pure Mode III} \end{cases} \quad \text{(Eq.5-15)}$$

5.3.2 Incorporation of compressive residual stress

One of the most frequently used features in SIF is that linearity prevails and thus superposition is possible, i.e., the superposition principle. Hence, stress intensity factor calculated from compressive residual stress introduced by the HFMI treatment simulation can be superimposed into one from a remote load, which is the effective stress intensity factor, K_{eff} , denoted by Eq. (5-16).

$$K_{eff} = K_{applied} + K_{CRS} \quad \text{Eq.(5-16)}$$

where, $K_{applied}$ is by a remote loading, and K_{CRS} is by a compressive residual stress.

On the other hand, the range of ΔK_{eff} does not change even when compressive residual stress is superimposed, as described below Eq. (5-17). Hence, crack closure model that was proposed by Elber [116] was introduced to calculation of ΔK_{eff} . Superimposed compressive residual stress can decrease both K_{max} and K_{min} . Fatigue cracks only propagate when the crack tip exists tensile condition, i.e., $K > 0$. In the case of $K < 0$, crack propagation does not occur and therefore the crack closure model deals with that K value as $K = 0$, see Eq. (5-18). Moreover, stress ratio at the crack tip can be influenced by compressive residual stress, and hence, the effective stress ratio, R_{eff} , was employed, see Eq. (5-19).

$$\Delta K_{eff} = (K_{applied}^{max} + K_{CRS}) - (K_{applied}^{min} + K_{CRS}) = K_{applied}^{max} - K_{applied}^{min} \quad \text{Eq.(5-17)}$$

$$\Delta K_{eff} = (K_{applied}^{max} + K_{CRS}) - \max(0, K_{applied}^{min} + K_{CRS}) \quad \text{Eq.(5-18)}$$

$$R_{eff} = \frac{K_{applied}^{min} + K_{CRS}}{K_{applied}^{max} + K_{CRS}} \quad \text{Eq.(5-19)}$$

5.4 Investigation of influence of crack front template on SIF

The study by Aygöl [88] recommended investigation of the influence of the crack front template parameters on SIF value since those parameters may affect the SIF value. Hence, the influence of the crack front template parameters, such as template radius, num rings, and num circumferential elements, on SIFs was investigated. In addition, the study by Gadallah et al. [117] reported that SIF values calculated by a remote load and CFT have a possibility to make a difference. Hence, how large difference appeared on SIF values by the remote load and CFT was also investigated.

Axial remote load whose magnitude is 150 MPa in nominal stress was applied

to the local model including crack depth of 2.0 mm. Figure 5-8 shows the generated nominal stress through thickness. The figure also shows the local stress distribution in the corresponded location where fatigue crack was inserted. This local stress distribution was subjected over crack face via CFT. At first, the number of num rings and elements was fixed as 3 and 8, and template radius was changed as 0.03, 0.02, 0.1 and 0.3. Then, template radius was fixed as 0.03 and the number of num rings and num elements were changed as 5 and 16, respectively.

Figure 5-9 shows the investigation results of the influence of the crack front template on SIF value. Vertical axis and horizontal axis show K_I value and normalized distance along the crack front. The crack mouth and crack deepest points are represented at 0 and 1.0, respectively, as shown in Fig. 5-9a. From the results of change template radius, it is observed that K_I values around the crack deepest points are not affected even when the template radius is changed, whereas those around the crack mouth are severely affected. This is because wider portion of roughness of the HFMI treated surface is included into the SIF calculation due to larger template radius. The K_I value converges when template radius is finer less than 0.03, and the difference is not observed when template radius is 0.02 and 0.03 (see Fig. 5-9b). From the results of change the number of num rings and num elements, clear difference on the K_I value is not observed (see Fig. 5-9c) since the integral area is not changed.

Figure 5-9 also shows the K_I value by CFT, see dot lines. Compared with the K_I value by the remote load, difference between them seems to be a minor. The magnitude of the difference is about 2.0 % at the crack mouth points (0.0), is about 1.5 % from the 0.3 to 0.5, and is about 3.5 % at the crack deepest point (1.0) when template radius was 0.03 and the number of num rings and num elements was 3 and 8, respectively. Similar difference is observed even when template radius was 0.02 and it was not improved even after the number of num rings and num elements were changed to 5 and 16, see Fig. 5-9c.

Thus, it is found that template radius is severely affected to SIF value, especially for the HFMI treated surface, whereas the influence of the number of num rings and num elements is a minor. The maximum difference of SIF value by remote load and CFT is appeared at the crack front, and it is less than 3.5 %, which is a minor. From this result, template radius was 0.03 and the number of num rings and num elements was 3 and 8 for subsequent analysis.

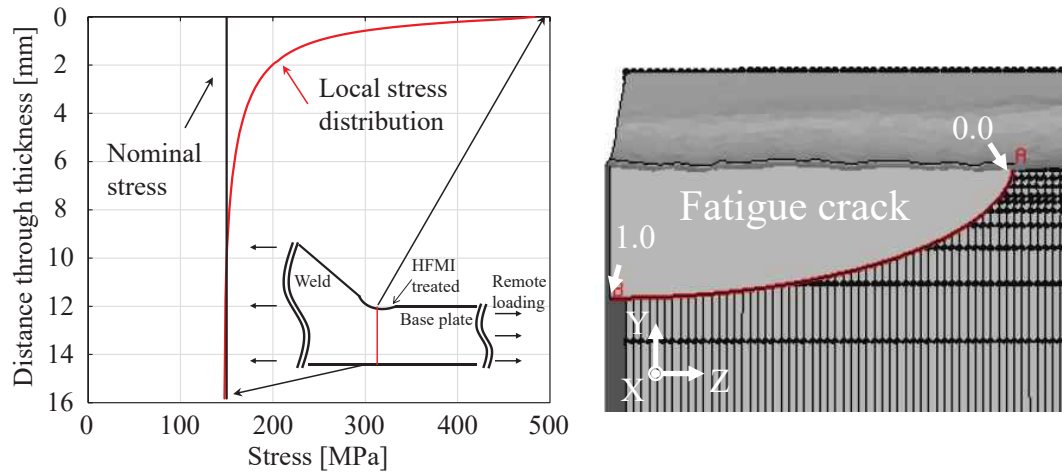
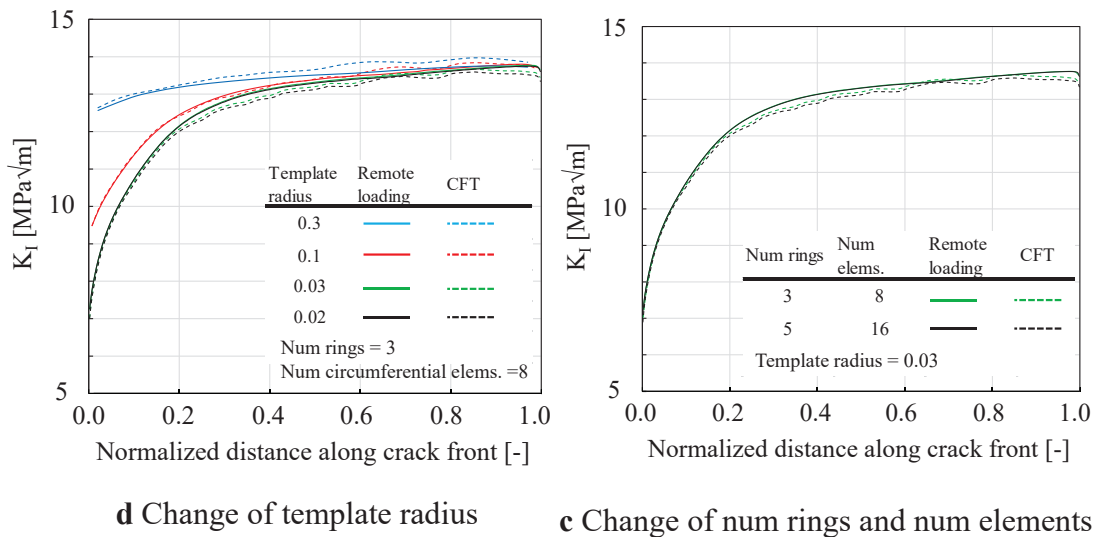


Figure 5-8 Generated stress distribution through thickness

a Normalized distance along crack front



d Change of template radius

c Change of num rings and num elements

Figure 5-9 Investigation results of the influence of crack front template on SIF

5.5 Investigation of crack opening stress at crack tip

Yamada and Ishikawa [118] assumed a remained crack in the ICR treated per-fatigued weld as an internal elliptical crack and calculated SIF value at the crack tip in the ICR treated weld for the fatigue life evaluation based on LEFM. They demonstrated that the fatigue life of the ICR treated pre-fatigued weld was well estimated. Therefore, it can be assumed that SIFs at the crack tips in HFMI treated welds would be investigated as the same manner as the study by Yamada and Ishikawa [118]. When the SIFs at the crack tips in HFMI treated welds are known, crack opening stress at the crack tip in HFMI

treated weld can also be evaluated using the obtained SIF values. That would be able to reveal when the cracks in HFMI treated welds start to propagate.

In order to investigate SIF value at the crack tip in HFMI treated weld, remained cracks in HFMI treated welds are assumed as semi-elliptical cracks considering the opening-closing behavior of the HFMI treated slit studied in **Chapter 4**. Table 5-1 shows the list of the crack shape in HFMI treated weld determined from the behavior. At first, depending on the magnitude of applied nominal stress, the crack shape is assumed as either an internal elliptical crack (case 1) or a semi-elliptical crack (case 2), see Fig. 5-10. Then, a crack shape, either case 1 or case 2, was inserted into the local model and corresponded nominal stress was applied to it, and ΔK_{eff} value at the crack tip was calculated. Since compressive residual stress field was superimposed over the crack face, ΔK_{eff} value will show minus value when no stress is applied to the model. Hence, the crack opening stress at the crack tip was defined when ΔK_{eff} value is more than 0.

Table 5-1 List of the crack chape in HFMI treated welds determined from the opening-closing behavior of the HFMI treated slit studied in **Chapter 4**

Applied stress in nomi.[MPa]	Crack depth of 0.5 mm			Applied stress in nomi.[MPa]	Crack depth of 1.5 mm		
0	a	c	-	0	a	c	Case 1
	-	-			0.125	5.3	
65	a	c	Case 1	50	a	c	Case 1
	0.2	4			0.2	5.3	
75	a'	c'	Case 2	75	a	c	Case 1
	0.5	4			0.4	5.3	
150	a'	c'	Case 2	90	a'	c'	Case 2
	0.5	4			1.5	5.3	
				150	a'	c'	Case 2
					1.5	5.3	
Applied stress in nomi.[MPa]	Crack depth of 1.0 mm			Applied stress in nomi.[MPa]	Crack depth of 2.0 mm		
0	a	c	Case 1	0	a	c	Case 1
	0.125	4.6			0.375	5.9	
75	a'	c'	Case 2	40	a	c	Case 1
	1.0	4.6			0.7	5.9	
150	a'	c'	Case 2	80	a	c	Case 1
	1.0	4.6			0.9	5.9	
				100	a'	c'	Case 2
					2.0	5.9	
				150	a'	c'	Case 2
					2.0	5.9	

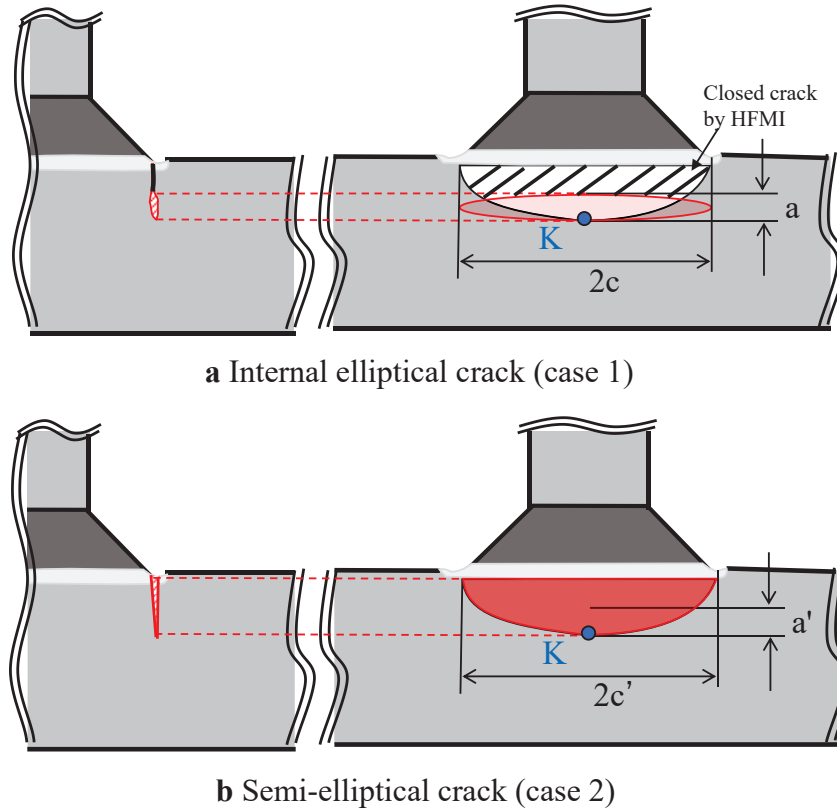


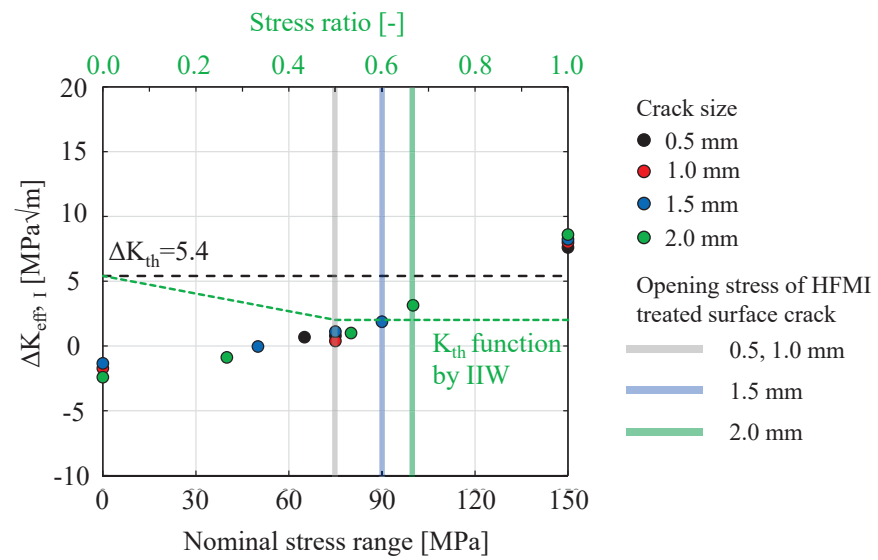
Figure 5-10 Assumed crack shape in HFMI treated welds

Figure 5-11 shows the investigation results of SIFs, of Mode-I and Mode-II, at the crack tip. This figure shows the K_{th} function considering stress ratio provided by IIW [99], see green dot line. The ΔK_{th} , derived from $R_{eff}=0.0$, is also described as black dot line. Opening stresses at HFMI treated surface crack are also depicted as shadow and colored shadow lines. ΔK_{eff} value at the crack deepest point was taken from 10 % inside of the local model. This adjustment is that the K value could be influenced when the point where K value is taken accords with the model's boundary condition [106].

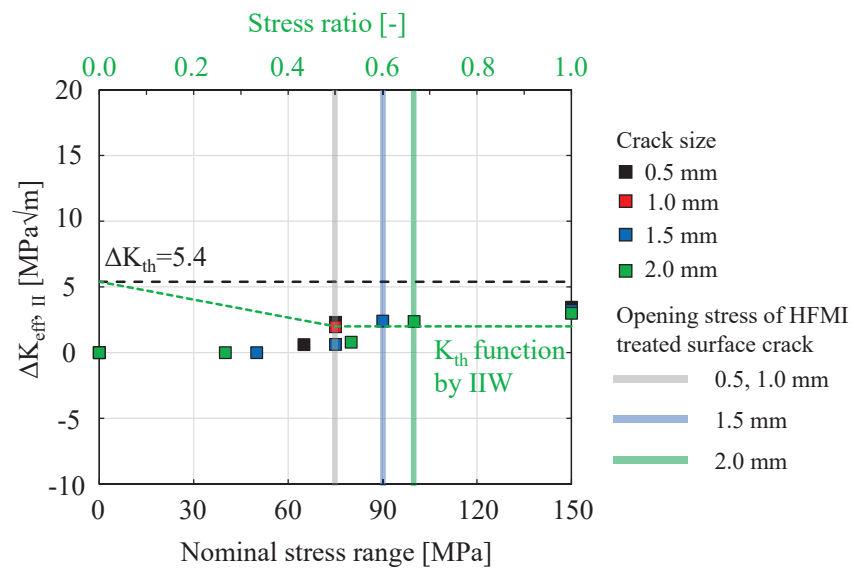
From the results of Mode-I shown in Fig. 5-11a, when no stresses were applied to the models with crack depths of from 0.5 to 2.0 mm, the $\Delta K_{eff, I}$ at the cracks tips were calculated from the case 1, see Fig. 5-10a, and it showed minus values. After nominal stress increases up to around 40 MPa, the $\Delta K_{eff, I}$ value of the crack depth of 1.5 and 2.0 mm is below 0, which means fatigue crack tips are not opened. When the nominal stress reaches 65 MPa, the $\Delta K_{eff, I}$ value of the crack depth of 0.5 mm is beyond 0. Similarly, the $\Delta K_{eff, I}$ value of the crack depths of 1.0, 1.5, and 2.0 mm are beyond 0 when the nominal stress reaches around 80 MPa in nominal stress. Therefore, crack opening stresses at the crack tip are between around 65 and 80 MPa. Meanwhile, the nominal stresses when the

HFMI treated surface cracks are opened were 75 MPa for crack sizes of 0.5 and 1.0 mm, 90 MPa for 1.5 mm, and 100 MPa for 2.0 mm. Those stresses are almost identical or below the crack opening stresses at the crack tips. It should be noted that, as mentioned in **Chapter 4**, initial welding residual stresses were given to the rat-hole models after the slits were inserted. This procedure did not consider the influence of residual stress redistribution/relaxation due to crack initiation/propagation. This would affect compressive residual stress distribution after HFMI treatment simulation and whether the cracks in HFMI treated welds propagate. Accordingly, further investigation would be required, which is outside of this thesis. After the HFMI treated surface cracks are opened, the $\Delta K_{eff, I}$ value drastically increases and is far above the $\Delta K_{th}=5.4 \text{ MPa}\times\text{m}^{(1/2)}$ derived by $R_{eff}=0$ when the nominal stress reaches at 150 MPa. Hence, it can be here concluded that the cracks in the HFMI treated welds propagate after the HFMI treated surface crack is opened.

From the results of Mode-II shown in Fig. 5-11b, the $\Delta K_{eff, II}$ value of the crack tips of the crack depths of 0.5-, 1.0-, 1.5-, and 2.0 mm shows around 0 when the nominal stress is 0 MPa. Even when the nominal stresses reach the crack opening stress at the HFMI treated surface cracks, i.e., 75 MPa for crack sizes of 0.5 and 1.0 mm, 90 MPa for 1.5 mm, and 100 MPa for 2.0 mm, the $\Delta K_{eff, II}$ value of the cack tips are still around 0. After the HFMI treated surface cracks are opened, the $\Delta K_{eff, II}$ value is around $3 \text{ MPa}\times\text{m}^{(1/2)}$ and below the ΔK_{th} value. Further increase of those values is not observed when the nominal stress increases up to 150 MPa. Therefore, it can be said that Mode-II would not contribute to crack propagation.



a Mode-I



b Mode-II

Figure 5-11 Investigation results of SIF at the crack tip

5.6 Crack propagation analysis using LEFM

5.6.1 Crack propagation using quasi-static growth model

There are two types of crack propagation models in Franc3D: the quasi-static growth model and sub-critical crack growth model [106]. The main difference between them is whether a critical value, ΔK_{th} value, and stress ratio are considered on crack propagation. Even though crack propagation is performed using the quasi-static growth model, those values can be considered when fatigue life is calculated. The aim of this CPA is not to predict precise fatigue life after HFMI treatment but to investigate defect tolerance of HFMI treated welds in bridge application for life extension. Hence, fatigue cracks in HFMI treated welds propagate using the quasi-static growth model and crack propagation behavior is first studied. The quasi-static growth model allows crack front propagation based on the crack growth increment and the computed SIFs value at the crack front points, see Fig. 5-12. The amount of crack front extension is determined by the simple power law expressed in Eq. (5-20).

$$\Delta a_i = \Delta a_{medium} \left(\frac{K_i}{K_{medium}} \right)^n \quad \text{Eq.(5-20)}$$

where, Δa_i is the crack front extension in the crack front point, Δa_{medium} is the crack growth increment which can be specified manually. K_i is the crack growth rate computed on the i th crack surface point, K_{medium} is the crack front growth rate computed on a crack surface point extended by Δa_{medium} . n is coefficient and 2 is provided by Franc3D. After current crack surface is extended by Δa_i , new crack surface appears. This new crack surface front was fitted automatically using polynomial curves, see Fig. 5-13. In this study, moving polynomial curve provided by Franc3D was used for the new crack front fitting.

No recommendations are provided in literature or design codes for the crack growth increments that should be used. The small crack growth increment would result in many analyses steps in the case of large fatigue cracks. The size of crack growth increment most likely affects the prediction of the fatigue life [119]. Objective of this investigation is not to predict fatigue life accurately but to understand crack propagation behavior of crack in HFMI treated weld. Hence, crack growth increments were arbitrarily adjusted in the range of 0.1 to 0.3 mm until the crack depth reached around 3 mm in total depth. This adjustment of crack growth increment is because cracks did not propagate when constant crack growth increment was used due to given compressive residual stress distributions.

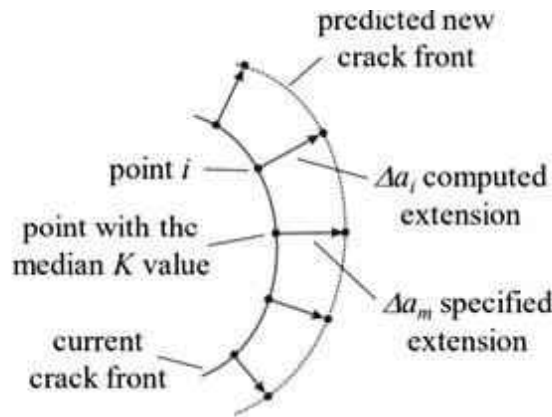


Figure 5-12 Crack propagation based on crack growth increment [117]

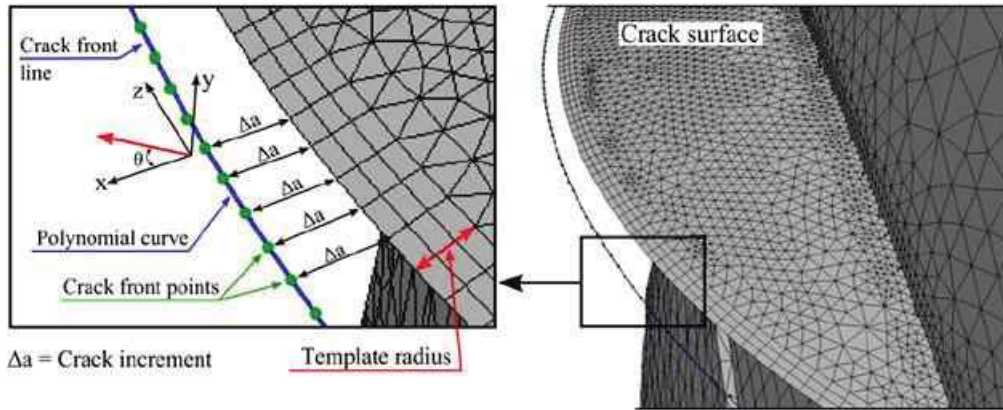


Figure 5-13 Curve fitting of crack front points found in [88]

5.6.2 Results of crack propagation analysis in HFMI treated welds

Figure 5-14 shows the observation of crack shape after CPA. Fatigue cracks in HFMI treated welds were extended assuming to be coplanar ($\theta=0$) under the condition of $\Delta K_{eff} = K_{150 MPa} + K_{CRS}$ since $K_{15 MPa} + K_{CRS}$ is below 0. CPA results in the final crack depth of around 3.0 mm. In further depth, any curve fitting of crack front provided by Franc3D failed, and therefore, CPA was not able to be performed more than around 3 mm. Fatigue cracks shaped by black line and by red line show the initial and final crack sizes, respectively.

The result of the crack depth of 0.5 mm shows that the initial fatigue crack propagates maintaining semi-elliptical shape up to final crack depth of 1.8 mm. Although last a few curve fittings near the HFMI treated surfaces are rough, see Fig. 5-14a, this rough curve fitting could be due to that superimposed compressive residual stress is uniformly distributed in the width direction of the crack and given crack growth increment is large. For the results of the crack depths of 1.5 and 2.0 mm, fatigue cracks propagate

maintaining a roughly semi-elliptical shape up to 2.5 mm in depth, see Figs. 5-14c and 5-14d. On the other hand, for the result of the crack depth of 1.5 mm, fatigue crack propagates in depth direction with a convex shape downward when the crack depth is more than 2.4 mm, see Fig. 5-14d, and crack shape becomes distorted. This crack shape is because given compressive residual stress state to the model is turned into tensile at a depth of around 2.5 mm, see Figs. 5-4 and 5-5. Therefore, the magnitude of crack front extension in depth direction becomes remarkably larger than one near the HFMI treated surface. This distorted crack shape is due to the difference of the magnitude of crack front extension in width and depth directions. On the other hand, increase of crack growth speed in depth direction when the crack depth becomes larger was deduced in previous experimental studies relating fatigue life extension of HFMI treated pre-fatigued welds [9, 120, 121]. This CPA result would demonstrate those deductions. However, it would be assumed that obtained crack shape when the crack depth is more than 2.5 mm in depth significantly differs from a crack shape observed in an experimental study. Accordingly, when 3D CPA considering compressive residual stress introduced by HFMI treatment is

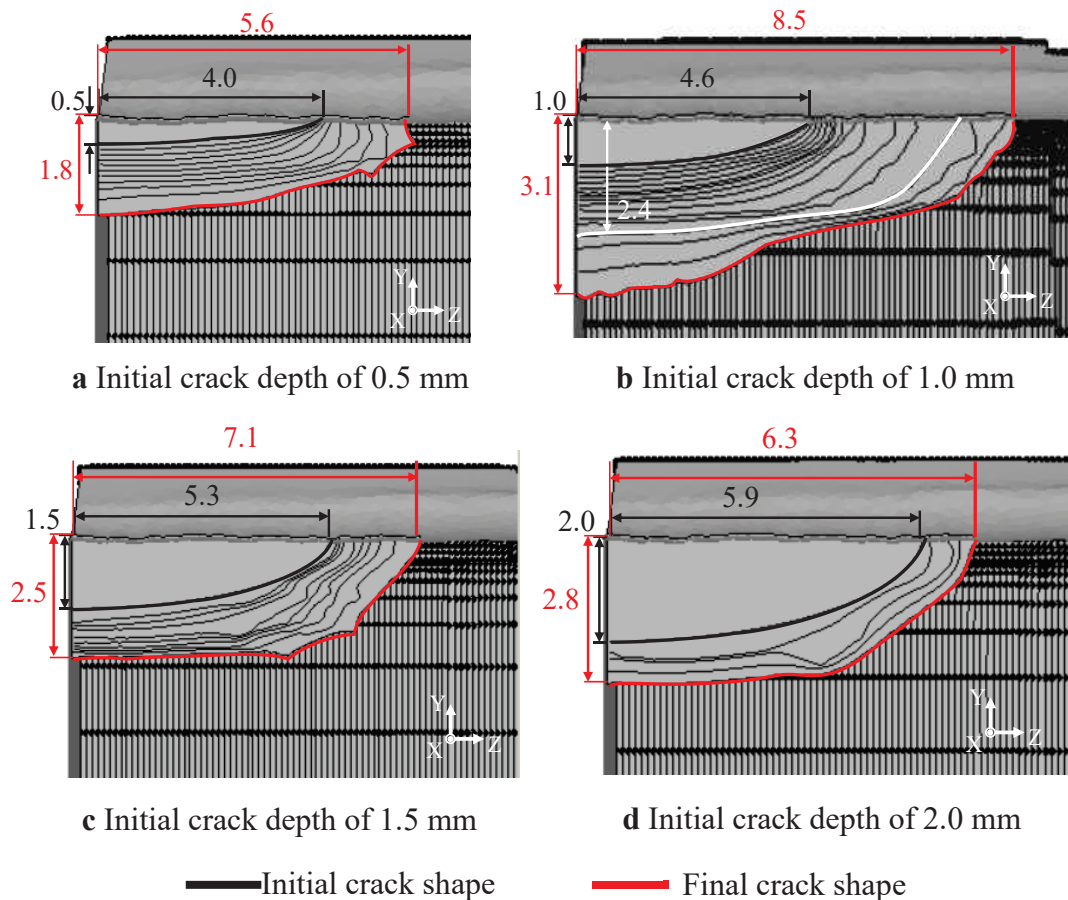


Figure 5-14 Observation of crack shape after crack propagation [Unit: mm]

accomplished to be carried out more than 2.5 mm in depth, further improvements would be required, e.g., consideration of stress redistribution/relaxation due to crack propagation, which is outside of this thesis.

5.6.3 Fatigue life calculation

After CPA, fatigue life from initial crack depth to final crack depth was calculated in order to investigate defect tolerance of HFMI treated welds in bridge application for life extension. For calculation of the number of cycles, the Paris and Erdogan law [87] considering threshold stress intensity factor was employed, as denoted by Eqs. (5-21) and (5-22).

$$\frac{da}{dN} = C(\Delta K_{eff} - \Delta K_{th})^m \quad (\text{Eq.5-21})$$

$$N = \int_{a_i}^{a_f} \frac{da}{C(\Delta K_{eff} - \Delta K_{th})^m} \quad (\text{Eq.5-22})$$

where, $C=5.21 \times 10^{-13} \text{ N} \times \text{mm}^{(-2/3)}$ and $m=3$, provided by IIW [99], are used. For threshold stress intensity factor, $\Delta K_{th}=2.0 \text{ MPa} \times \text{m}^{(1/2)}$ was used instead of $\Delta K_{th}=5.4 \text{ MPa} \times \text{m}^{(1/2)}$ [99]. In Franc3D, fatigue life calculation is stopped under either conditions; 1) the K_{max} at any crack front points on a crack reaches a critical value, 2) ΔK for all points on the crack front fall below a ΔK_{th} , and 3) a total of applied load cycles reaches a subscribed load cycle. However, although specific reason is unknown, fatigue life calculation of HFMI treated weld was stopped even when neither condition was achieved. Hence, this adjustment of threshold stress intensity factor was to avoid calculation stopping due to numerical problem, recommended by Franc3D [106]. A fatigue life can be directly estimated by integrating the Paris and Edgren law, see Eq. (5-16). a_i is initial crack size, a_f is critical or final crack size, and N is the number of cycles when a crack grows from a_i to a_f . The number of cycles was calculated using SIF of Mode-I.

5.6.4 Results of fatigue life calculation

Figure 5-15 shows the results of fatigue life calculation in depth direction. Path to calculate the number of cycles is also shown. Initial crack depth was correlated by using each crack depth. Since fatigue crack shape is distorted when the crack depths are more than 2.5 mm, the fatigue life is compared up to 2.5 mm in depth.

From the results, fatigue crack propagates in depth direction with increasing the number of cycles. Compared with the number of cycles at 2.5 mm in depth, the results of crack depths of 1.5 and 2.0 mm show around 300 000 cycles. The result of 1.0 mm shows around 500 000 cycles, and further cycles is necessary to reach a depth of 2.5 mm in the case of 0.5 mm. Hence, the effect of life extension by HFMI treatment is increased as the initial crack depth is shallower, whereas it is almost the same when the crack depth is more than 1.5 mm. On the other hand, the fatigue strength of the rat-hole weld is categorized as FAT70 [99]. Considering the fatigue test condition, $\Delta \sigma = 135$ MPa, its fatigue life to failure would be 300 000 cycles. The number of cycles of 1.5 and 2.0 mm is almost the same as the number of cycles, whereas 0.5 and 1.0 mm exceeds the one. Therefore, although the limited comparison of the number of cycles up to a crack depth of 2.5 mm was made, it can be concluded that the effect of fatigue life extension could be obtained effectively when HFMI treatment is carried out to pre-fatigued welds, including cracks that are shallower than 1.5 mm in depth.

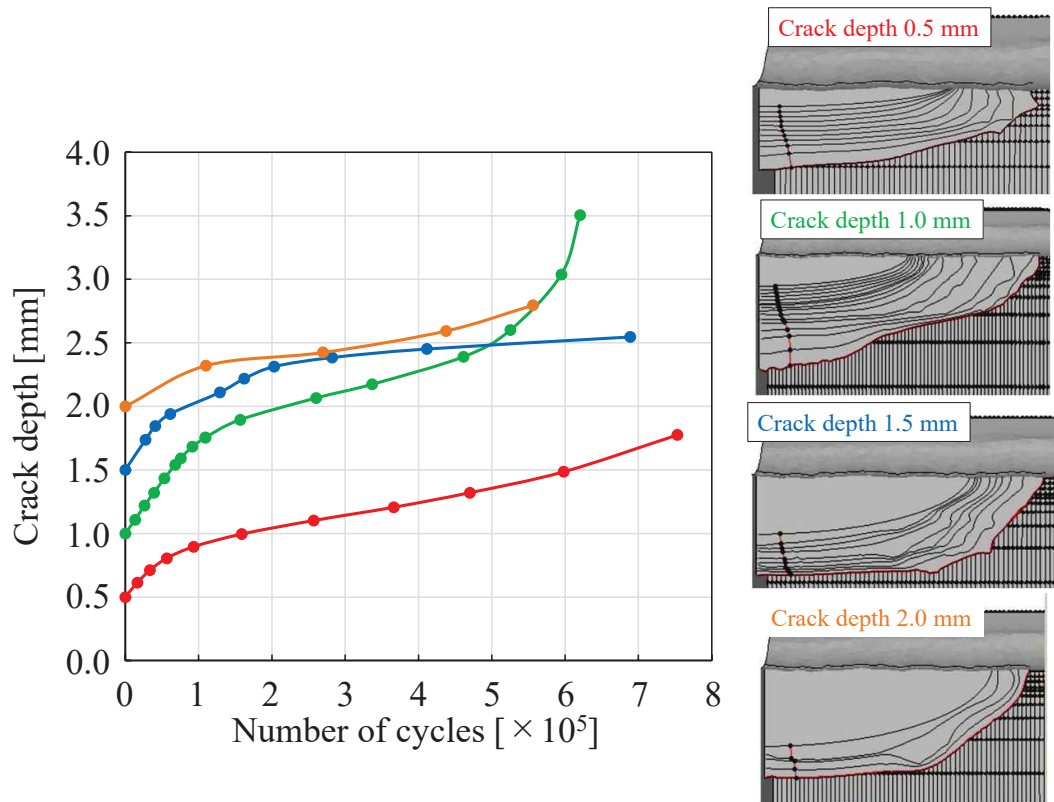


Figure 5-15 Results of fatigue life calculation in depth direction
(Maximum stress 150 MPa, Minimum stress 15 MPa)

5.7 Conclusions

The objective of this chapter is to investigate defect tolerance of HFMI treated

welds in bridge application for life extension. Rat-hole models with different fatigue crack depths in the HFMI treated welds were used in 3D CPA based on LEFM, considering compressive residual stresses introduced by HFMI. At first, crack opening stress at the crack tip in HFMI treated weld was investigated numerically considering the crack opening-closing behavior. Then, the 3D CPA based on LEFM was carried out under fatigue load, and crack propagation behavior was studied. The fatigue life was calculated based on the CPA results, and the defect tolerance of HFMI treated welds in bridge application for life extension was investigated. The conclusions can be summarized as followings:

1. Crack opening stress at the crack tip in HFMI treated welds was investigated numerically considering the crack opening-closing behavior. The numerical investigation results show that the crack opening stress at the crack tip, which was defined as $\Delta K_{eff} \geq 0$, were between around 65 and 80 MPa in nominal stress, which is less than the stresses when the HFMI treated surface cracks are opened. Furthermore, it is found that the cracks in HFMI treated welds would propagate under Mode-I based on the SIF evaluation results at the crack tips.
2. 3D CPA was carried out under fatigue load and crack propagation behavior was studied. Fatigue cracks in HFMI treated welds propagated maintaining semi-elliptical shape up to 2.5 mm in depth. In further depth of more than 2.5 mm, the crack propagated in depth direction with a convex shape downward. This is because given compressive residual stress is turned into tensile, and crack growth speed is significantly changed in depth and width directions. Hence, the crack propagation behavior could be studied up to 2.5 mm in depth, but further improvement of the model, such as stress relaxation/redistribution due to crack propagation, would be required for more depth.
3. Fatigue life from initial crack depth to final crack depth was calculated based on the 3D CPA results. Although the limited comparison in the number of cycles was made up to a crack depth of around 2.5 mm, the calculation results show that the effect of fatigue life extension could be obtained effectively when HFMI treatment is carried out to pre-fatigued welds including the cracks that are shallower than 1.5 mm in depth.

Chapter 6

Conclusions

6.1 Conclusions

The objective of this thesis is to propose defect tolerance of HFMI treated welds in bridge application for life extension based on numerical FE simulations. In line with the objective, followings were carried out in the subsequent chapters of this thesis.

First, review of literature including the authors' previous study was conducted in **Chapter 2** in order to determine the subjects for the subsequent chapters of this thesis. Background of the necessary knowledge of the state-of-the-arts peening techniques, such as hammer and needle peening and HFMI treatment, was briefly introduced. Numerical HFMI simulation, which has been gathering a lot of interest nowadays, was introduced, and optimum settings and parameters for the HFMI simulation were introduced and discussed. Then, experimental investigation on life extension of pre-fatigued weld using the peening techniques was introduced and the effect of life extension was discussed. Thereafter, the basic knowledge of Linear Elastic Fracture Mechanics (LEFM) was briefly introduced and fatigue life estimation of HFMI treated weld using LEFM was discussed. As a results of the review of literature including the author's previous study, the subjects for the subsequent chapters were determined.

Prior to the investigation of defect tolerance of HFMI treated welds, the validity of 3D FE HFMI simulation using an isotropic hardening model for residual stress estimation was verified for two models: flat and bead on steel plates in **Chapter 3**. First, to reduce simulation time, the mass scaling method was applied to the HFMI simulation, and the influence of the mass scaling method on the HFMI simulation was examined in terms of simulation time, residual stress state, and energy balance during the HFMI simulation. As a result, simulation time of more than 90 % can be reduced. Also, it is found that the mass scaling method should be used carefully when longitudinal residual stress is important. Then, HFMI simulations varying feed rate and the number of hits of the HFMI indenter were carried out to the flat steel plate model. The results show that high feed rate can influence residual stress state near the HFMI treated surfaces, whereas increase in the number of hits is independent of the amount of induced residual stress. In addition, electropolishing was conducted after the HFMI simulation. The result shows that the accuracy of the numerically estimated residual stress in a depth direction can be slightly improved. Finally, the applicability of HFMI simulation using the isotropic hardening model was investigated to the bead on steel plate model. The results show that

the HFMI simulations using the isotropic hardening model can give reasonable estimation of the residual stresses in a depth of 0.2 mm even when welding residual stresses due to the welding are not considered. Through this investigation, the validity of HFMI simulation, especially for the influence of different HFMI treatment process on residual stress estimation, was verified. This verified HFMI simulation was used in the subsequent chapter.

Then, the effect of HFMI treatment on pre-fatigued welds and crack opening-closing behavior in HFMI treated welds were investigated based on the HFMI simulation using a combined hardening model in **Chapter 4**. A rat-hole weld, which is one of the fatigue-prone details in steel bridges, was used in the HFMI simulation. In order to simulate initial cracks, the detailed rat-hole specimen models included a rectangle slit with different depths, of 0.5-, 1.0-, 1.5-, and 2.0- mm, in their weld toes. The initial welding residual stress along the welds of the rat-hole models was estimated using elastic thermal analysis and subsequent HFMI simulations were carried out. As a results, the initial welding residual stress has a minor effect on the final residual stress state after the HFMI simulation. The HFMI simulations to the rat-hole models included different slit depths show that the magnitude of the induced compressive residual stress around the slit tip is reduced when the slit depth becomes larger, resulting in that the slit remained partly open. An opened remained slit was about 0.4 mm in the case that HFMI simulation with indentation depth of 0.2 mm was carried out to the rat-hole model with 2.0 mm slit depth. Hence, it can be said that HFMI treatment can close cracks that are shallower than 1.5 mm in depth. Investigation of opening-closing behavior of the HFMI treated slit based on a change of strains along the slit face under axial loading shows that the closed slit by HFMI treatment is opened from the inside prior to the surface. Additionally, crack opening-closing behavior was investigated experimentally using pre-fatigued out-of-plane gusset welded joints treated by the ICR treatment with the aid of the PAUT system. The results indicate that the behavior can be identified based on the change of echo height ratio from the crack, and similar crack opening-closing behavior was observed in the FE simulations. From both investigations, experimentally and numerically, the behavior on pre-fatigue welds treated by HFMI could be studied successfully.

Finally, defect tolerance of HFMI treated welds in bridge application for life extension was investigated in 3D CPA based on LEFM, using the rat-hole models with different fatigue crack depths in HFMI treated welds in **Chapter 5**. At first, the compressive residual stress state introduced by HFMI treatment simulation was considered over the cracks faces in HFMI treated welds. Crack opening stress at the crack tip in HFMI treated weld was investigated, considering crack opening-closing behavior

studied in **Chapter 4**. The results indicate that the crack opening stresses at the crack tip were between around 65 and 80 MPa in nominal stress, which is lower than the stresses when the HFMI treated surface cracks are opened. The results also indicate that the cracks in HFMI treated welds would propagate under Mode-I. Then, CPA based on LEFM was carried out under fatigue load and crack propagation behavior was studied. The results indicate that the cracks in HFMI treated welds propagate keeping semi-elliptical shape up to 2.5 mm in depth. More than 2.5 mm in depth, the crack propagates in depth direction with a convex shape downward, and the crack shape is distorted. This is caused by the significant change of crack growth speed in depth due to the change of residual stress filed from compression to tension. Hence, the crack propagation behavior could be studied up to 2.5 mm in depth, but further improvement of the model would be required when 3D CPA based on LEFM is conducted in more depth. Finally, fatigue life from initial crack depth to final crack depth was calculated. The results demonstrated that the effect of fatigue life extension could be obtained effectively by HFMI treatment when the fatigue cracks are shallower than 1.5 mm in depth.

Through the investigations conducted in **Chapters 4 and 5**, the size of cracks that HFMI treatment can tolerant and defect tolerance of HFMI treated welds in bridge application for life extension were investigated numerically. Based on those numerical FE simulation results, the author indicates fatigue cracks that are shallower than 1.5 mm in depth as a defect tolerance of HFMI treated rat-hole detailed welds for life extension.

6.2 Recommendation based on the current studies

Hedegård et al. [80] carried out fatigue tests using HFMI treated rat-hole specimens with different crack depths in their weld toe in order to investigate the effect of life extension by HFMI treatment. Fig. 6-1 shows the fatigue tests results organized by the gain factor [79], see red plots in this figure. The gain factor is shown in the vertical axis, defined below Eqs. (6-1), and (6-2).

$$\rho = \frac{N_{Ext}}{N_{Pre}} \quad (\text{Eq.6-1})$$

$$\rho_{new,HFMI} = \frac{N_{treated}}{N_{AW}} \quad (\text{Eq.6-2})$$

where, N_{pre} is the number of cycles of a specimen until fatigue cracks initiate and propagate to a certain fatigue crack depth, and N_{ext} is the number of cycles of the pre-

fatigued specimen treated by HFMI to failure. $\rho_{\text{new, HFMI}}$ is the ratio between the fatigue life of a HFMI treated state without pre-fatigue to that of the same detail in AW state. A ratio $\rho/\rho_{\text{new, HFMI}} > 1.0$ means that fatigue life of pre-fatigued welds could be equivalently extended to the ratio of life extension of a new treated detail. The fatigue test results demonstrate that HFMI treatment can extend the fatigue lives of pre-fatigued welds longer than the one of AW state in case the fatigue cracks are shallower than 1.5 mm through plate thickness. Although, indentation depth of HFMI treatment and the amount of introduced compressive residual stresses were not measured in this study [80] and hence direct comparison with the numerical simulation results was not made, the trend that the life extension can be success when HFMI treatment is carried out to the cracks shallower than 1.5 mm in depth is well in agreement with the numerical results led in this thesis.

Accordingly, based on both investigation results, numerically and experimentally, the author recommends that HFMI treatment be carried out to the rat-hole welds with fatigue cracks that are shallower than 1.5 mm in depth. Within this crack depth, HFMI treatment would be used as a robust life extension technique against fatigue damaged steel bridges.

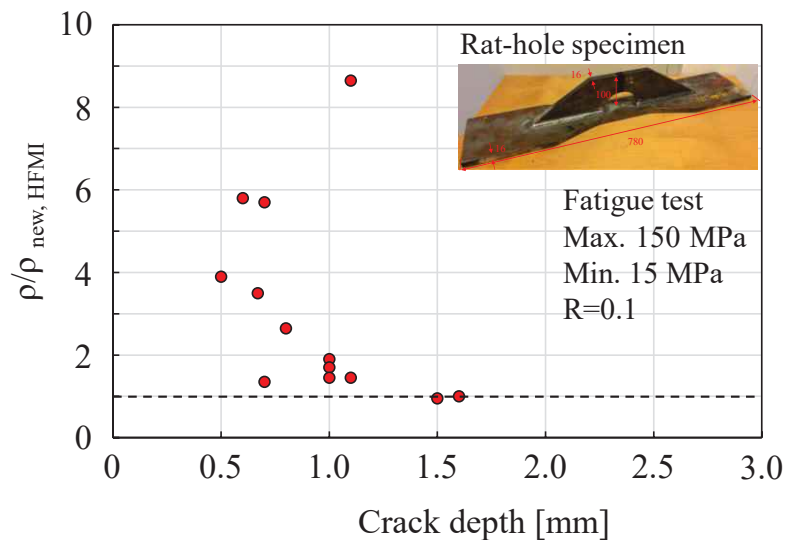


Figure 6-1 Experimental test results of HFMI treated pre-fatigued rat-hole specimen [80]

References

1. Stefan, B. (1929) The First Arc-Welded Bridge in Europe near Lowicz, Poland, The engineer, September 6th.
2. Mickle, D.G., Shumate, C.E., Voorhees, A.M., Carey, W.N. (1970) Welded Highway Bridges, an analysis of inspection factors, National Research Council, National Academy of Science, National Academy of Engineering, Special report, No.114.
3. Tamakoshi, T., Okubo, M., Yokoi, Y. (2014) Technical Note of National Institute for Land and Infrastructure Management, Annual Report of Basic Data on Road Structures in FY 2012, National Institute for Land and Infrastructure Management Ministry of Land, Transport and Tourism, Japan, ISSS 1346-7328, No.776. (In Japanese).
4. Haghani, R. (2013) Needs for Maintenance and Refurbishment of Bridge in Urban Environments, Type of report, Version 28, Chalmers university.
5. Miki, C. (2011) Retrofitting Engineering for Fatigue Damaged Steel Structures, International Institute of Welding, Doc. IIW-XIII-2284r1-09 ver. 2011.
6. Dexter, R.J., Ocel, J.M. (2013) Manual for Repair and Retrofit of Fatigue Cracks in Steel Bridges, FHWA Publication No. FHWA-IF-13-020, March 2013.
7. Miki, C., Mori, T., Tuda, S., Sakamoto, K. (1987) Retrofitting Fatigue Cracked Joints by TIG Arc Remelting, Structural Eng./Earthquake Eng., Vol.4, No.1, pp.85-93.
8. Yildirim, H.C., Marquis, G.B. (2012) Overview of Fatigue Data for High Frequency Mechanical Impact Treated Welded Joints, Welding in the World, Vol.56, pp.82-96.
9. Lefebvre, F., Peyrac, C., Elbel, G., Revilla-Gomez, C., Verdu, C., Buffière, J.Y. (2017) HFMI: Understanding the Mechanisms for Fatigue Life Improvement and Repair of Welded Structures, Welding in the World, Vol.61, pp.789-799.
10. Mori, T., Shimanuki, H., Tanaka, M. (2014) Influence of Steel Static Strength on Fatigue Strength of Web-Gusset Welded Joints with UIT, Journal of JSCE, Vol.70, No.2, pp.210-220. (In Japanese)
11. Roy, S., Fisher, J. W. (2005) Enhancing Fatigue Strength by Ultrasonic Impact Treatment, International Journal of Steel Structures, Vol.5, No.3, pp.241-252.
12. Yildirim, H.C., Leitner, M., Marquis, G.B., Stoschka, M., Barsoum, Z. (2016) Application Studies for Fatigue Strength Improvement of Welded Structures by High-Frequency Mechanical Impact (HFMI) Treatment, Engineering Structures, Vol.106, pp.422-435.
13. Marquis, G.B., Barsoum, Z. (2016) IIW Recommendations for the HFMI Treatment for Improvement the Fatigue Strength of Welded Joints, IIW Collection, Springer,

Singapore.

14. Haagensen, P.J., Maddox, S.J. (2013) IIW Recommendations on Methods for Improving the Fatigue Strength of Welded Joints, IIW-2142-110, Woodhead Publishing.
15. Kirkhope, K.J., Bell, R., Caron, L., Basu, R.I., Ma, K.T. (1999) Weld Detail Fatigue Life Improvement Techniques. Part 1: Review, Marine Structures, Vol.12, Issue. 6, pp.447-474.
16. Knight, J.W. (1978) Improving the Fatigue Strength of Fillet Welded Joints by Peening and Grinding, Welding Research International, No.8, pp.519-540.
17. Masumoto, I., Matsuda, K., Iwata, H., Hasegawa, M. (1984) Effect of Prestrain and Hammer Peening on Fatigue Strength Improvement of Mild Steel Welded Joint, Transactions of the Japan Welding Society, Vol.15, No.2, pp.94-100.
18. Anami, K., Miki, C., Tani, H., Yamamoto, H. (2000) Improving Fatigue Strength of Welded Joints by Hammer Peening and Tig-Dressing, Structural Eng./Earthquake Eng., JSCE, Vol. 17, No.1, 57s-68s.
19. Takashi, N., Katsuyoshi, N., Yasushi, M. (2015) Method of Improving Fatigue Strength by Peening on Base Metal and Development of Mechanized System, JFE technical report, No.20, pp. 118-124.
20. Nakanishi, K., Morikage, Y., Kawabata, A., Tomo, H. (2015) Study on Improvement Method of Fatigue Strength of Weld Joints by Hammer Peening on Base Metal, Structural Eng./Earthquake Eng., JSCE, Vol. 71, No.1, 10s-19s. (In Japanese).
21. Yamada, K., Kakiichi, T., Ishikawa, T. (2009) Extending Fatigue Life of Cracked Welded Joints by Impact Crack Closure Retrofit Treatment, International Institute of Welding, IIW-Doc. XIII-2289r1-09, pp.1-9.
22. Kakiichi, T., Ishikawa T., Yamada, K. (2013) Retrofitting of Fatigue Cracked Fillet Welded Joint by ICR treatment, Journal of Structural Engineering, Vol.59A, pp.665-672. (In Japanese).
23. Ono, Y., Kinoshita, K. (2021) Enhancing Fatigue Strength of Welded Joints Made of SBHS700 by Hammer Peening with ICR apparatus and HFMI treatment, Welding in the World, No.65, pp.301-316.
24. Kirkhope, K.J., Bell, R., Caron, L., Basu, R.I. (1997) Weld Detail Fatigue Life Improvement Techniques, Ship Structure Committee, SSC-400.
25. Inoue, R., Hosomi, N., Irube, T. (2016) Fatigue Strength Improvement Measures of Out-of-Plane Gusset Welded Joints by Portable Pneumatic Needle-Peening, Technical reports of TTK CORPORATION, No.57, pp.38-45. (In Japanese).
26. Stanikove, E.S., Korolkov, O.V., Muktepavel, V.O., Korostel, V.Y. (2008) Oscillating

- System and Tool for Ultrasonic Impact Treatment, Patent Application Publication, US 2008/0035627 A1.
27. Statnikov, S. (1999) Guide for Application of Ultrasonic Impact Treatment Improving Fatigue Life of Welded Structures, International Institute of Welding, IIW/IIS-Document XIII-1757-99.
 28. Marquis, G., Barsoum, Z. (2014) Fatigue Strength Improvement of Steel Structures by High-Frequency Mechanical Impact: Proposed Procedures and Quality Assurance Guidelines, *Welding in the World*, No.58, pp.19-28.
 29. Kudryavtsev, Y., Kleiman, J., Lugovskoy, A., Prokopenko, G.I. (2006) Fatigue Life Improvement of Tubular Welded Joints by Ultrasonic Peening, International Institute of Welding, IIW Document XIII-2117-06.
 30. Yuan, K. (2015) Residual Stress Analysis and Fatigue Strength Assessment of Welded Joints with Ultrasonic Impact Treatment (UIT), Doctoral Dissertation, Yokohama National University.
 31. Lihavainen, V.M., Marquis, G.B, Statnikov, E.S. (2004) Fatigue Strength of a Longitudinal Attachment Improved by Ultrasonic Impact Treatment, *Welding in the World*, Vol. 48, pp.67-73.
 32. Galtier, A., Statnikov, E. S. (2004) The Influence of Ultrasonic Impact Treatment on Fatigue Behaviour of Welded Joints in High-Strength Steel, *Welding in the World*, Vol.48, pp.61-66.
 33. Yildirim, H.C., Marquis, G.B. (2013) A Round Robin Study of High-Frequency Mechanical Impact (HFMI)-Treated Welded Joints Subjected to Variable Amplitude Loading, *Welding in the World*, No. 57, pp.437-447.
 34. Cheng, X., Fisher, J.W., Prask, H.J., Gnäupel-Herold, T., Yen, B.T., Roy, S. (2003) Residual Stress Modification by Post-Weld Treatment and Its Beneficial Effect on Fatigue Strength of Welded Structures, *International Journal of Fatigue*, No. 25, pp.1259-1269.
 35. Weich, I. (2011) Edge Layer Condition and Fatigue Strength of Welds Improved by Mechanical Post-Weld Treatment, *Welding in the World*, Vol. 55, pp.3-12.
 36. Lefevre P (2014) Fatigue Life Improvement of Welded Structures by Ultrasonic Needle Peening, Sonats white paper.
 37. Hanji, T., Anami, K. (2017) Influence of Static Strength of Steels on Fatigue Strength Improvement of Welded Joints by Toe Treatment, *Journal of Structural Engineering*, Vol.63A, pp.646-658. (In Japanese).
 38. Togasaki, Y., Tsuji, H., Honda, T., Sasaki, T., Yamaguchi, A. (2010) Effect of UIT on Fatigue Life in Web-Gusset Welded Joints, *Journal of Solid Mechanics and Materials*

Engineering, Vol.4, No.3, pp.391-400.

39. Yekta, R.T., Ghahremani, K., Walbridge, S. (2013) Effect of Quality Control Parameter Variations on the Fatigue Performance of Ultrasonic Impact Treated Welds, *International Journal of Fatigue*, No. 55, pp.245-256.
40. Khurshid, M., Leitner, M., Barsoum, Z., Schneider, C. (2017) Residual Stress State Induced by High Frequency Mechanical Impact Treatment in Different Steel Grades- numerical and experimental study, *International Journal of Mechanical Sciences*, Vol.123, pp.34-42.
41. Hardenacke, V., Farajian, M., Siegele, D. (2014) Modelling and Simulation of the High Frequency Mechanical Impact (HFMI) Treatment of Welded Joints, *International Institute of Welding*, IIW Doc. XIII-2533-14.
42. Ernould, C., Schubnell, J., Farajian, M., Maciolek, A., Simunek, D., Leitner, M., Stoschka, M. (2019) Application of Different Simulation Approaches to Numerically Optimize High-Frequency Mechanical Impact (HFMI) Post-Treatment Process, *Welding in the World*, Vol. 63, pp.725-738.
43. Hardenacke, V., Farajian, M., Siegele, D. (2014) Simulation of the High Frequency Hammer Peening Process for Improving the Fatigue Performance of Welded Joints, *Conf Proc 2014: ICSP-12 Goslar*, pp. 359-364.
44. Leitner, M., Simunek, D., Shah, S.F., Stoschka, M. (2018) Numerical Fatigue Assessment of Welded and HFMI-Treated Joints by Notch Stress/Strain and Fracture Mechanical Approaches, *Advanced in Engineering Software*, Vol.120, pp.96-106.
45. Leitner, M., Khurshid, M., Barsoum, Z. (2017) Stability of High Frequency Mechanical Impact (HFMI) Post-Treatment Induced Residual Stress States under Cyclic Loading of Welded Steel Joints, *Engineering Structures*, Vol.143, pp.589-602.
46. Schubnell, J., Hardenacke, V., Farajian, M. (2017) Strain-Based Critical Plane Approach to Predict the Fatigue Life of High Frequency Mechanical Impact (HFMI)-Treated Welded Joints Depending on the Material Condition, *Welding in the World*, Vol.61, pp.1199-1210.
47. Liu, Y., Gong, B., Deng, C., Zhao, C., Liu, X., Wang, D. (2018) Numerical Analysis of Optimum Treatment Parameters by High Frequency Mechanical Impact, *Journal of Constructional Steel Research*, Vol.150, pp.23-30.
48. Ruiz, H., Osawa, N., Rashed, S. (2019) A Practical Analysis of Residual Stresses Induced by High-Frequency Mechanical Impact Post-Weld Treatment, *Welding in the world*, Vol. 63, pp.1255-1263.
49. Ruiz, H., Osawa, N., Rashed, S. (2020) Study on the Stability of Compressive Residual Stress Induced by High-Frequency Mechanical Impact Under Cyclic

- Loadings with Spike Loads, *Welding in the World*, Vol. 64, pp.1855-1865.
50. Föhrenbach, J., Hardenacke, V., Farajian, M. (2016) High Frequency Mechanical Impact Treatment (HFMI) for the Fatigue Improvement: numerical and experimental investigations to describe the condition in the surface layer, *Welding in the World*, Vol.60, pp.749-755.
 51. Föhrenbach, J. (2015) Fatigue Life Prediction of High Frequency Mechanical Impact (HFMI) Treated Welded Joints by Numerical Simulation and Damage Mechanics Approaches, Master Thesis, Hochschule Offenburg, University of Applied Science.
 52. Quilliec, G.L., Lieurade, H.P., Bousseau, M., Drissi-Habti, M., Inglebert, G., Macquet, P., Jubin, L. (2011) Fatigue Behaviour of Welded Joints Treated by High Frequency Hammer Peening: Part II, Numerical Study, *International Institute of Welding*, IIW document XIII-2395-11.
 53. Schaumann, P., Keindorf, C. (2008) Experiments and Simulations of Welded Joints with Post Weld Treatment, *DFE2008 Design, Fabrication and Economy of Welded Structures*, pp.493-502.
 54. Zheng, J., Ince, A., Tang, L. (2018) Modelling and Simulation of Weld Residual Stresses and Ultrasonic Impact Treatment of Welded Joints, *Procedia Engineering*, Vol. 213, pp.36-47.
 55. Schubnell, J., Farajian, M., Däuwel, T., Shin, Y. (2018) Numerical Fatigue Life Analysis of a High Frequency Mechanical Impact Treated Industrial Component based on Damage Mechanics Models, *Material Science and Engineering Technology*, Vol. 49, Issue.1, pp.113-127.
 56. Lennart, J. et al. (2018) Committee V.3: Materials and Fabrication Technology, *Proceedings of the 20th International Ship and Offshore Structures Congress (ISSC2018)*, *Progress in marine science and technology*, No.2, pp.143-191.
 57. Gkatzogiannis, S., Knoedel, P., Ummenhofer, T. (2019) FE Simulation of High Frequency Mechanical Impact (HFMI) Treatment – First Results, *NORDIC STEEL 2019, The 14th Nordic Steel Construction Conference*, pp.797-802.
 58. Gkatzogiannis, S (2020) Finite Element Simulation of Residual Stresses from Welding and High Frequency Hammer Peening, *Doctoral Dissertation*, Karlsruhe Institute of Technology.
 59. Schubnell, J., Carl, E., Farajian, M., Gkatzogiannis, S., Knödel, P., Ummenhofer, T., Wimpory, R., Eslami, H. (2020) Residual Stress Relaxation in HFMI-treated Fillet Welds after Single Overload Peaks, *Welding in the World*, Vol.64, pp.1107-1117.
 60. Baptista, R., Infante, V., Branco, C. (2011) Fully Dynamic Numerical Simulation of the Hammer Peening Fatigue Life Improvement Technique, *Procedia Engineering*,

Nol.10, pp.1943-1948.

61. Schubnell, J., Eichheimer, C., Ernould, C., Maciolek, A., Rebelo, J., Farajian, M. (2020) The Influence of Coverage for High Frequency Mechanical Impact Treatment of Different Steel Grades, *Journal of Materials Processing Technology*, Vol. 277.
62. Yang, X., Zhou, J., Ling, X. (2012) Study on Plastic Damage of AISI 304 Stainless Steel Induced by Ultrasonic Impact Treatment, *Materials and Design*, Vol. 36, pp.477-481.
63. Chaobo, G., Shengsun, H., Dongpo, W., Zhijiang, W. (2015) Finite Element Analysis of the Effect of the Controlled Parameters on Plate Forming Induced by Ultrasonic Impact Forming (UIF) Process, *Applied Surface Science*, Vol.353, pp.382-390.
64. Chaobo, G., Zhijiang, W., Dongpo, W., Shengsun, H. (2015) Numerical Analysis of the Residual Stress in Ultrasonic Impact Treatment Process with Single-Impact and Two-Impact Models, *Applied Surface Science*, Vol.347, pp.596-601.
65. Shengsun, H., Chaobo, G., Dongpo, W., Zhijiang, W. (2016) 3D Dynamic Finite Element Analysis of the Nonuniform Residual Stress in Ultrasonic Impact Treatment Process, *ASM international*, Vol.25, pp.4004-4015.
66. Yuan, K., Sumi, Y. (2016) Simulation of Residual Stress and Fatigue Strength of Welded Joints Under the Effects of Ultrasonic Impact Treatment (UIT), *International Journal of Fatigue*, Vol. 92, pp.321-332.
67. Avallone, E.A., Baumeister, T. (1996) Marks' Standard Handbook for Mechanical Engineers - Tenth Edition, McGraw-Hill Publishing.
68. Manoucherifar, A., Rezvani, K. (2011) 3D FE Analysis of Shotpeening Process for Simulation and Research on Shotpeening Process Parameters, 11th International Conference on Shot Peening, pp.67-74.
69. Chaboche, J. L. (2008) A Review of Some Plasticity and Viscoplasticity Constitutive Theories, *International Journal of Plasticity*, Vol.24, Issue.10, pp.1642-1693.
70. Abaqus manual, <http://130.149.89.49:2080/v6.14/books/usb/default.htm>
71. Simunek, D., Leitner, M., Stoschka, M. (2013) Numerical Simulation Loop to Investigate the Local Fatigue Behaviour of Welded and HFMI-Treated Joints, *International Institute of Welding*, IIW-WG2-136-13.
72. Bridge and Tunnel management, TRV, 2010, <https://batman.trafikverket.se/externportal>
73. Fujino, Y., Kawai, Y. (2016) Technical Developments in Structural Engineering with Emphasis on Steel Bridges in Japan, *Journal of JSCE*, Vol.4, pp.211-226.
74. Aldén, R., Barsoum, Z., Vouristo, T., Al-Emrani, M. (2020) Robustness of the HFMI Techniques and the Effect of Weld Quality on the Fatigue Life Improvement of

- Welded Joints, Welding in the World, Vol.64, pp.1947-1956.
75. Akiyama, R., Kinoshita, K. (2016) Effect of ICR Treatment on Fatigue Cracked Welded Joints, Proceeding of Construction Steel, Vol.24, pp. 663-667. (In Japanese)
 76. Fueki, R., Abe, H., Takahashi, K., Ando, K., Houjou, K., Handa, M. (2015) Improving of Fatigue Limit and Rendering Crack Harmless by Peening for Stainless Steel Containing a Crack at the Weld Toe Zone, Journal of High Pressure Institute of Japan, Vol.53, Issue.3, pp.140-148.
 77. Kudryavtsev, Y., Kleiman, J., Lugovskoy, A., Lobanov, L., Knysh, V., Voitenko, O., Prokopenko, G. (2005) Rehabilitation and Repair of Welded Elements and Structures by Ultrasonic Peening, International Institute of Welding, IIW-Doc. XIII-2076-05.
 78. Leitner, M., Barsoum, Z., Schäfers, F. (2016) Crack Propagation Analysis and Rehabilitation by HFMI of Pre-Fatigued Welded Structures, Welding in the World, No. 60, pp.581-592.
 79. Branco, C.M., Infante, V., Baptista, R. (2004) Fatigue Behaviour of Welded Joints with Cracks, Repaired by Hammer Peening, Fatigue and Fracture of Engineering Materials and Structures, Vol.27, Issue. 9, pp785-798.
 80. Hedegård, J., Al-Emrani, M., Edgren, M., Manai, A., Al-Karawi, H., Barsoum, Z. (2020) LifeExt-Prolonged Life for Existing Steel Bridges, open report, INFRA SWEDEB2030.
 81. Al-Karawi, H., Al-Emrani, M. (2021) The Efficiency of HFMI Treatment and TIG Remelting for Extending the Fatigue Life of Existing Welded Structures, Steel Construction, Vol.14, Issue.2, pp.95-106.
 82. ASTM (2012) Standard Test Method for Linear-Elastic Plan Strain Fracture Toughness K_{IC} of Metallic Materials, E 399-12.
 83. Irwin, G.R. (1957) Analysis of Stresses and Strains Near the End of a Crack Traversing a Plate, Journal of Applied Mechanics, Issue 24, pp.361-364.
 84. Barsoum, Z. (2008) Residual Stress Analysis and Fatigue Assessment of Welded Steel Structures, Doctoral thesis, Kungliga Tekniska Högskolan.
 85. Anderson, T.L. (2011) Third Edition Fracture Mechanics Fundamental and Applications, Taylor and Francis Group.
 86. Aamodt, B., Bergan, P.G. (1976) ON THE PRINCIPLE OF SUPERPOSITION FOR STRESS INTENSITY FACTORS, Engineering Fracture Mechanics, Vol.8, pp.437-440.
 87. Paris, P., Erdogan, F. (1963) A Critical Analysis of Crack Propagation Laws, Journal of Basic Engineering, Vol.85, Issue 4, pp.528-533.
 88. Aygül, M. (2013) Fatigue Evaluation of Welded details - using the Finite Element

Method, Doctoral thesis, Chalmers University.

89. Hirt, M.A., Fisher, J.W. (1972) Fatigue Crack Growth in Welded Beams, Fritz Engineering Laboratory Report No. 358.35, Lehigh University.
90. Albrecht, P., Yamada, K. (1977) Rapid Calculation of Stress Intensity Factor, Journal of the Structural Division, Vol.4, Issue.8, pp.377-389.
91. Yamada, K., Hirt, M.A. (1982) Fatigue Crack Propagation from Fillet Weld Toe, Journal of the Structural Division, Vol.108, Issue.7, pp.1526-1540.
92. Miki, C., Sakano, M., Toyoda, Y., Yshizawa, T. (1990) Early-Stage Propagation Behaviour of Fatigue Cracks in Fillet Welded Joints, Structural Eng./Earthquake Eng., Vol.7, No.1, pp.123-131.
93. Al-Karawi, H., Franz, R.U., Al-Emarani, M. (2021) Fatigue Life Extension of Existing Welded Structures via High Frequency Mechanical Impact (HFMI) Treatment, Engineering Structures, Vol.239.
94. Zhang, H., Wang, D., Xia, L., Lei, Z., Li, Y. (2015) Effects of Ultrasonic Impact Treatment on Pre-Fatigued Loaded High-Strength Steel Welded Joints, International Journal of Fatigue, Vol. 80, pp.278-287.
95. SSAB, Multisteel SN, <https://www.ssab.com/products/brands/ssab-multisteel/ssab-multisteel-sn>.
96. Wang, L., Long, H. (2011) Investigation of Material Deformation in Multi-Pass Conventional Metal Spinning, Materials and Design, Vol.32, pp.2891-2899.
97. Ma, N., Umez, Y. (2009) Analysis Application of Explicit FEM to Welding Deformation, Welding International: Translation from the Worlds Welding Press, Vol.23, No.1, pp1-8.
98. Japanese Society of Steel Construction. (2018) JSSC Technical Report, No.115. (In Japanese)
99. Hobbacher, A. (2012) Update of the Fracture Mechanics Chapters of the IIW fatigue Design Recommendations, International Institute of Welding, IIW-doc. XIII-2370r1-11, XV-1376r1-11, pp.1-24.
100. Manai, A., Polach, U., Emrani, A.M. (2020) A Probabilistic Study of Welding Residual Stress Distribution and Their Contribution to the Fatigue Life, Engineering Failure Analysis, Vol.118, pp.1-19.
101. Miki, C., Shirahata, H., Yamaguchi, R., Kinoshita, K., Yaginuma, Y. (2007) Nondestructive Evaluation and Fatigue Crack Detection of Double Bevel T-joint by Ultrasonic Testing, Journal of JSCE, Vol.63, No. 4, pp.628-638. (In Japanese)
102. Shirahata, H., Kamikuri, T. (2016) Non Destructive Evaluation of Rib-to-Deck Fatigue Crack in Deck Plate of Orthotropic Steel Deck System by the Phased Array Ultrasonic Testing, Journal of JSCE, Vol.72, No.1, pp.206-219. (In Japanese)

- 103.Yagi, N., Suzuki, T., Wakabayashi, N., Murano, M., Miki, C. (2016) Detection of Inner Fatigue crack in Welding between Steel Deck Plate and Trough Rib by Phased Array Non-Destructive Testing, Journal of JSCE, Vol.72, No.3, pp.393-406. (In Japanese)
- 104.Kinoshita, K., Obara, K., Nohdo, T., Kozuka, M. (2019) Non-destructive Identification of Closed Fatigue Crack Reopening Mechanism by Ultrasonic Testing, Proceeding of Constructional Steel, Vol.27, pp.1-6. (In Japanese)
- 105.Yamada, K., Ishikawa, T., Kakiichi, T. (2015) Rehabilitation and Improvement of Fatigue Life of Welded Joints by ICR treatment, Advanced Steel Construction, Vol.11, No.3, pp.294-304.
- 106.Franc3D. <https://franc3d.in/software/>
- 107.Wawrzynek, P., Carter, B., Ingraffea, T., Ibrahim, O. (2012) Franc3D Workshop/Training, Corning Glass, May 7, 2012.
- 108.Davis, B.R., Wawrzynek, P.A., Carter, B.J., Ingraffea, A.R. (2016) 3-D Simulation of Arbitrary Crack Growth using an Energy-Based Formulation - Part II: Non-Planar Growth, Engineering Fracture Mechanics, Vol. 154, pp.111-127.
- 109.Tai, M., Miki, C. (2012) Improvement Effects of Fatigue Strength by Burr Grinding and Hammer Peening Under Variable Amplitude Loading, Welding in the World, Vol.56, pp.109-117.
- 110.Takayuki, Y., Hiroshi, S., Takeshi, M. (2019) Relaxation Behavior of Compressive Residual Stress Induced by UIT Under Cyclic Loading, Quarterly Journal of the Japan Welding Society, Vol.37, No.1, pp.44-51. (In Japanese)
- 111.Tada, H., Paris, P.C., Irwin, G.R. (2000) The Stress Analysis of Cracks, Handbook Third Edition, Professional Engineering Publishing.
- 112.Rice, J.R. (1968) A Path Independent Integral and the Approximate Analysis of Strain Concentration by Notches and Cracks, Journal of Applied Mechanics, Vol. 35, pp.379-386.
- 113.Glinka, G., Shen, G. (1991) Universal Features of Weight Functions for Cracks in Mode I, Engineering Fracture Mechanics, Vol. 40, No. 6, pp. 1135-1146.
- 114.Yau, J.F., Wang, S.S., Corten, H.T. (1980) A Mixed-Mode Crack Analysis of Isotropic Solids Using Conservation Laws of Elasticity, Journal of Applied Mechanics, Vol. 47, pp.335-341.
- 115.Singh, R., Carter, B.J., Wawrzynek, P.A., Ingraffea, A.R. (1998) Universal Crack Closure Integral for SIF Estimation, Engineering Fracture Mechanics, Vol. 60, No.2, pp.133-146.
- 116.Elber, W. (1971) The Significance of Fatigue Crack Closure: Damage Tolerance in

Aircraft Structures, ASTM International, ASTM STP 486, pp.230-242.

117. Gadallah, R., Osawa, N., Tanaka, S. (2017) Evaluation of Stress Intensity Factor for a Surface Cracked Butt Welded Joint Based on Real Welding Residual Stress, *Ocean Engineering*, Vol.138, pp.123-139.
118. Yamada, K., Ishikawa, T. (2017) Evaluation on Retrofitting Effect of ICR treatment by Fracture Mechanics, *Journal of Structural Engineering*, Vol.63A, pp.659-667. (In Japanese)
119. Barsoum, Z., Barsoum, I. (2009) Residual Stress Effects on Fatigue Life of Welded Structures using LEFM, *Engineering Failure Analysis*, Vol.16, pp. 449-467.
120. Infante, V., Branco, C.M., Baptista, R. (2001) Fatigue Analysis of Welded Joints Rehabilitated by Hammer Peening, Instituto Superior Tecnico, Paper for IIW meeting, Ljubljana, Slovenia, 2001, Ref. XIII-1892/01, pp.1-42.
121. Weich, I. (2008) Ermüdungsverhalten mechanisch nachbehandelter Schweißverbindungen in Abhängigkeit des Randschichtzustands, Fatigue behaviour of mechanical post weld treated welds depending on the edge layer condition, Dissertation, Technischen Universität Carolo-Wilhelmina, Braunschweig, 2009 (in German).